High Fidelity Modeling and Analysis of Nanoengineered Composites and Complex Sandwich Structures

by

Karthik Rajan Venkatesan

A Dissertation Presented in Partial Fulfillment
of the Requirements for the Degree
Doctor of Philosophy

Approved June 2021 by the
Graduate Supervisory Committee:

Aditi Chattopadhyay, Chair
Yongming Liu
Yang Jiao
Masoud Yekani Fard
Tom Stoumbos

ARIZONA STATE UNIVERSITY

August 2021

ABSTRACT

Damage and failure of advanced composite materials and structures are often manifestations of nonlinear deformation that involve multiple mechanisms and their interactions at the constituent length scale. The presence and interactions of inelastic microscale constituents strongly influence the macroscopic damage anisotropy and useful residual life. The mechano-chemical interactions between constituents at the atomistic length scale play a more critical role with nanoengineered composites. Therefore, it is desirable to link composite behavior to specific microscopic constituent properties explicitly and lower length scale features using high-fidelity multiscale modeling techniques.

In the research presented in this dissertation, an atomistically-informed multiscale modeling framework is developed to investigate damage evolution and failure in composites with radially-grown carbon nanotube (CNT) architecture. A continuum damage mechanics (CDM) model for the radially-grown CNT interphase region is developed with evolution equations derived using atomistic simulations. The developed model is integrated within a high-fidelity generalized method of cells (HFGMC) micromechanics theory and is used to parametrically investigate the influence of various input micro and nanoscale parameters on the mechanical properties, such as elastic stiffness, strength, and toughness. In addition, the inter-fiber stresses and the onset of damage in the presence of the interphase region are investigated to better understand the energy dissipation mechanisms that attribute to the enhancement in the macroscopic out-of-plane strength and toughness. Note that the HFGMC theory relies heavily on the description of microscale features and requires many internal variables, leading to high computational costs. Therefore, a novel reduced-order model (ROM) is also developed to

surrogate full-field nonlinear HFGMC simulations and decrease the computational time and memory requirements of concurrent multiscale simulations significantly.

The accurate prediction of composite sandwich materials' thermal stability and durability remains a challenge due to the variability of thermal-related material coefficients at different temperatures and the extensive use of bonded fittings. Consequently, the dissertation also investigates the thermomechanical performance of a complex composite sandwich space structure subject to thermal cycling. Computational finite element (FE) simulations are used to investigate the intrinsic failure mechanisms and damage precursors in honeycomb core composite sandwich structures with adhesively bonded fittings.

ACKNOWLEDGMENTS

The completion of the research work presented in this dissertation would not have been probable without the efforts of many people to whom I owe much appreciation. I am incredibly thankful and indebted to my advisor, Regents' Professor Aditi Chattopadhyay, for the guidance, encouragement, and challenge she provided me throughout the doctoral program. I am incredibly grateful for all her advice and supervision that has helped me mature into someone deserving of the doctoral title. I would also like to thank the members of my Supervisory Committee, Professor Yongming Liu, Professor Yang Jiao, Dr. Tom Stoumbos, and Professor Masoud Yekani Fard, for all their valuable support and feedback that helped me improve the quality of the research presented in this work.

Gratitude is also due to my colleagues in Professor Chattopadhyay's research group and the Adaptive Intelligent Materials & Systems (AIMS) center. Through discussions and collaborations with Dr. Siddhant Datta, Dr. Bonsung Koo, Dr. Nithya Subramanian, Dr. Ashwin Rai, I developed some of my best ideas and acquired specific research directions. I would also like to thank Mr. Vincent Luu and Ms. Cristianne Scherrer for aiding with the day-to-day tasks of the AIMS Center. Finally, I would like to thank my parents and brother and their unending support and love.

I would also like to acknowledge the funding sources, the program manager, and the technical liaison that supported this research. The Office of Naval Research supported the primary work presented in this dissertation through grant number N00014-17-1-2029. The program manager is Dr. Anisur Rahman. The Northrop Grumman Corporation supported the secondary work presented in this dissertation, and the program manager was Dr. Tom Stoumbos.

TABLE OF CONTENTS

Page

CHAPTER Page

LIST OF TABLES

LIST OF FIGURES

Figure Page

Figure Page

Figure Page

CHAPTER 1

INTRODUCTION

1.1 Background

With the substantial need for the use of advanced composite materials with superior performance capabilities, there is a growing need to efficiently engineer such material systems, tailoring them for specific applications. A primary example is the carbon fiber reinforced polymer (CFRP) composites. CFRP composites can be engineered to produce high strength, lightweight, fatigue resistance, fire-retardant materials, substantiating their use in a wide range of aerospace and naval applications (Gay 2014). Recent advances in nanotechnology have also led to the incorporation of carbon nanotubes (CNTs) in traditional CFRP composites that can potentially impact a wide range of aerospace and marine applications through improved mechanical strength, through-thickness characteristics, fracture toughness, and added multi functionalities (Thostenson et al. 2001; Datta et al. 2015; Datta et al. 2018). The long aspect ratio and small size of these particles are responsible for several transformative characteristics: the large surface area to volume ratio, flexibility in surface functionalities, and superior mechanical performance compared with any other known material form. These nanoengineered CFRP composites offer vital advantages such as greater tailorability of the composite structural and nonstructural properties.

On the other hand, sandwich composites consisting of thin CFRP laminate face sheets covering a thick lightweight core material are also used in aerospace and spacecraft structures for their lightweight, high in-plane mechanical properties and high bending stiffness. They are often designed to meet close thermal distortion and damage tolerance in space applications,

as they are exposed to harsh environments and extreme temperature ranges. However, due to the constituent and architectural complexity, scale-dependent load transfer characteristics, and damage anisotropy in such complex material systems, investigations of relevant failure mechanisms and useful life prediction in service conditions are critical to ensuring improved structural durability and safety.

1.2 Nanoengineered Composites

In traditional CFRP composites, the interface between the plies is well known to be a 'weak link' in laminated composites, which requires significant reinforcement along the out-of-plane direction. Several methods to locally enhance the interlaminar strength by introducing nanomaterials in the matrix region between the plies have been investigated. The enhancement of mechanical properties of composites have been reported by incorporating nanoscale fillers such as CNT (Jyoti et al. 2015, Aldajah and Haik 2012, Vaganov et al. 2016), fullerenes (Ogasawara et al. 2009, Tayfun et al. 2015), and nanoclay (Shokrieh et al. 2012, Xu and Hoa 2008). These nanofillers can modify the composite interface and improve load transfer through several reinforcing mechanisms at the nanoscale, such as chemical bonding (He et al. 2007), wetting, mechanical interlocking (Moaseri et al. 2014), and local anchoring/stiffening of the polymer matrix (Chou et al. 2010). A 60% enhancement in interlaminar fracture toughness was observed by incorporating fullerene (0.1-1 wt.%) in the matrix resin (Ogasawara et al., 2009). Over the last decade, CNT reinforcements have been used to explore the possibility of enhancing both the inter- and intralaminar regions (Rai et al., 2017; Green et al., 2009). A clear majority of the investigations use CFRP composites with randomly dispersed CNT architecture (Seyhan et al., 2008; Thakre et al. 2011; Godara et al. 2009; Chou et al. 2010). CNTs have strengthened both the interlaminar and intralaminar regions in CFRPs (Rai et al. 2017; Green

et al. 2009). The random dispersion of CNTs in the polymer matrix show improved strength, interlaminar toughness, and energy absorption capabilities (Inam et al., 2010; Cho et al., 2008). These studies show a marginal increase in mechanical, electrical, and fire-retardant properties with only a small weight fraction of CNTs in the host matrix material. Enhanced delamination resistance and fracture toughness have also been demonstrated (Kin-Tak et al., 2003; Kumar et al. 2005; Rangari et al. 2008; Seyhan et al. 2008; Thakre et al. 2011). Recent developments have also reported the growth of radially-aligned CNTs on the reinforcing fibers within composite materials (Pozegic et al. 2016, Krishnamurthy et al. 2017), embedded CNT-nanoforests (Lettiere et al. 2019), and CNT ropes. Such novel CNT architectures offer key advantages, such as a low percolation threshold (0.1~5 vol.%), many particles per unit volume, extensive interfacial area per unit volume, and short distances between particles. They can also significantly improve a wide range of multifunctional properties, including mechanical, electrical, thermal, electro-magnetic interference shielding, piezoelectric/resistive, and fire safety.

1.3 High Fidelity Modeling Motivation

Despite the enormous benefits offered by nanoengineered composites, a significant technology barrier limiting their use in practical application is attributed to the lack of a complete understanding of the physical factors and their impact on the composite constituents and structural response in service conditions. Although this may be achieved through extensive experimental characterization and testing, many physical variables and their complex interactions, especially for CNT-enhanced composites, make this approach infeasible. For instance, several factors affect the properties of CNT-enhanced composites; these include spatial and compositional nature of the CNTs, size, orientation, and spatial distribution within

the composite matrix material, fiber and matrix properties, interfacial bonding and adhesion between the CNTs and surrounding matrix, and constituent volume fractions. Environmental effects, such as temperature, humidity, and pressure, during manufacturing and operation also play a crucial role in the overall properties of nanoengineered composites. However, because of the complexities associated with these material systems, damage prediction and quantification studies are often limited to two-dimensional or idealized geometries, linearly elastic constitutive models, and prescribed damage initiation location and progression path (Murthy and Chamis, 1986; Swaminathan, Ghosh, and Pagano, 2006; Skoček, Zeman, and Šejnoha, 2008). These assumptions can lead to oversimplification of the problem and, therefore, often result in poorly predicted critical material behaviors.

In general, macroscopic damage and failure of composites are manifestations of inelastic deformation that involve multiple damage mechanisms at the micro constituent level. The presence and interactions of multiple inelastic phases or inclusions in composites at lower length scales strongly influence the macroscale damage anisotropy. With CNT-enhanced composites, the mechano-chemical interactions between the CNTs and surrounding polymer and fiber at the atomistic length scale needs to be considered. Homogenization techniques that utilize only macroscale constitutive models will fail to achieve the required accuracy necessary to predict damage and residual life. Therefore, it is desirable to link CNT-enhanced composite behavior to specific microscopic constituent properties explicitly, and atomistic scale features using multiscale modeling techniques. Besides, the development of a high-fidelity computational multiscale framework initiating at the atomistic scale to address nanoscale interactions and subsequent effects arising from these interactions is critical to obtaining a holistic understanding of the behavior of CNT-enhanced nanocomposites. Such a framework requires scale-specific constitutive models, critical model parameters, and physics-

based criteria to link discrete atomistic scale phenomena to continuum scale models. At the nanoscale, molecular dynamics (MD) simulations have shown strong potential in modeling CNT-enhanced composites due to the comparable sizes of CNTs and polymer chains of the host matrix. Significant research has been reported on modeling and predicting the thermo-mechanical properties of CNT-enhanced nanocomposites using MD simulations (Li et al. 2017, Jung et al. 2020, Jiang et al. 2020, Suk 2020).

Consequently, MD simulations can be used to investigate the atomistic phenomena and the effects of various nanoscale parameters on mechanical properties such as elastic moduli, interfacial strength, and bonding energy at higher length scales. The framework should also explicitly incorporate microstructural details into structural analysis and address the complex coupled effects of different micro constituent parameters on the overall response at the microscale. An illustration of an atomistically-informed concurrent multiscale analysis framework is shown in Figure 1.

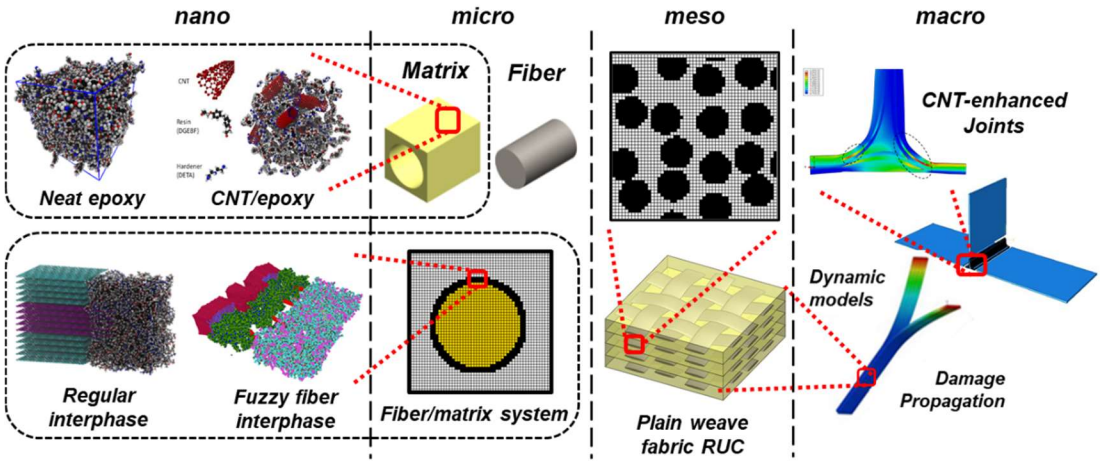

Figure 1. Atomistically Informed Multiscale Framework

1.4 Multiscale Simulations – Challenges

Developing a computational framework that incorporates the effects of various length scales is challenging due to the significant disparity in time and length scales and the complex interactions of the various scale-dependent phenomenon that needed to be physically modeled. Conventional multiscale analysis approaches have been developed to determine macroscopic composite behaviors, primarily through homogenization and localization rules associated with a microscale repeating unit cell (RUC) or representative volume element (RVE) with periodic boundary conditions (PBCs). Multiscale 'handshaking' methodologies include hierarchical, concurrent, or synergistic approaches. Hierarchical models have the highest computational efficiency and lowest fidelity of the three approaches. They are characterized by an uncoupled one-way flow of information across length scales via a top-down (localization) or bottom-up (homogenization) approach. The lack of two-way information transfer precludes the consideration of path-dependent material nonlinearity and limits hierarchical models to linear thermoelastic analyses. The concurrent approach represents all constituents in a single model and involves simultaneous computation at all length scales. These models may be semi-analytical (Pineda et al. 2017), which are computationally efficient but often lack fidelity, or fully numerical, which are highly accurate at the cost of computational efficiency. Multi-level finite element (FE) methods are fully numerical concurrent approaches, which involve equipping a macroscopic integration point in an FE analysis with a sub-grid containing the composite RUC or RVE (Feyel 2003, Tikarrouchine et al. 2018). Such approaches are highly accurate; however, the mesh size required to resolve all constituents in a single structural scale model results in prohibitive computational overhead, limiting the scope

of concurrent multiscale analyses. As a result, researchers have been forced to make do with idealized RUCs, limiting the capture of micromorphology effects across length scales.

However, another approach to determine composite behaviors centers on semi-numerical methods that provide a compromise between fidelity and efficiency via a two-way flow of information between length scales. Examples include the generalized method of cells (GMC) (Paley et al. 1992), high-fidelity GMC (HFGMC) (Zhong et al. 2004, Haj-Ali et al. 2009), and their respective efficient reformulations (Balasu et al. 2020). GMC is more often used within a multiscale framework due to its high computational efficiency; however, GMC uses a linear sub-element or subcell displacement field, leading to a lack of normal-shear coupling between individual phases. In contrast, the HFGMC theory employs a second-order subcell displacement field, accounting for normal-shear coupling and resulting in linearly varying stress, strain, and temperature fields at the subcell level. This approach has been verified for various composite material systems defined by a periodic RUC or RVE (Haj-Ali et al. 2014, Freed and Aboudi 2009, Dodla 2018). Unlike the FE methods, HFGMC imposes displacement continuity between adjacent subcells in an average sense. This approximation directly applies average traction continuity and enables the explicit definition of additional stress variables in the formulation. The subcell displacement components are directly tied to both the applied remote average strain and the fluctuating displacement micro variables.

Furthermore, this approximation allows the advantage of applying PBCs over both the global and local micro variables, wherein the PBCs in the FE formulation are imposed only through displacement total variables. Haj-Ali and Aboudi 2013 illustrated the specific differences by comparing the HFGMC to the FE to analyze a relatively wide range of cases. However, the higher fidelity of HFGMC simulations at the microscale comes at a high computational cost. It is 'mesh' size-dependent and requires fine spatial discretization to

ensure convergence to resolve all constituents in a single structural model. This results in prohibitive computational overhead that limits the scope of concurrent multiscale structural analyses to idealized geometries and small-scale coupons. Therefore, it is highly beneficial to develop an efficient multiscale modeling framework that can simulate the multi-physical behavior of advanced composites systems with significantly improved computational efficiency using surrogate modeling or reduced-order approximation techniques.

1.5 Composite Sandwich Space Structures

Composite sandwich structures have excellent in-plane and flexural stiffness and a high strength-to-weight ratio, substantiating their suitability for a wide range of space structure applications. However, while in orbit, these structures are often exposed to hostile environments involving high vacuum, ultraviolet radiations, and extreme temperature ranges. The fluctuating temperature conditions pose severe challenges to the composite sandwich material's thermal stability and durability and, therefore, significantly impact space structures' overall performance.

The structural behavior of composite sandwich materials under cyclic thermal loading is a complex phenomenon, gaining more importance in designing spacecraft structures, satellite components, and composite laminates in general. One of the most common types of failure due to the thermal cycling of sandwich structures is microcracking in the composite face sheet. The primary cause is the non-homogeneity that arises from the mismatch in the coefficient of thermal expansion (CTE) between the core and face sheet and the adhesively bonded fittings. Hodge et al. (2018) investigated crack formation in carbon fiber epoxy-based matrix composite cryogenic tanks and evaluated the microcracking characteristics at both room and cryogenic temperatures. Liquid hydrogen tanks made of composite sandwich material failed thermal

cyclic validation tests when the outer skin and core separated from the inner skin due to microcracks forming in the inner skin. Elevated humidity and thermal cycling also substantially affect the critical strain energy release rate associated with delamination due to the face sheet/core debonding (Tuttle and Mark 2018). In the long run, the microcrack formation in the composite face sheet increases with an increase in thermal cycles, which causes degradation in the mechanical properties, including strength (Lee et al. 2002; Shimokawa et al. 2002). Besides, the ultimate pull-out and shear strengths of adhesively bonded fittings decrease when tested at elevated temperatures and wet conditions (Snead et al. 1983; Park et al. 2011). Local stress concentrations in the adhesive layer and the free edge interface between the fitting and skin act as potential hot spots for microcrack initiation, likely due to improper bonding during the manufacturing process and the wide mismatch in material stiffness and CTE. Depending on the type of fitting geometry and loading conditions, the hot spots may trigger damage and interact with different modes to create complex failure behavior in sandwich structures (Feldusen et al. 2009; Heimbs et al. 2009). Adhesive failure, interlaminar failure, face sheet compressive fracture and wrinkling, and core buckling are some of the commonly anticipated failure modes (Dattaguru et al. 1984; Petras and Sutcliffe 1999; Ferrari 2015). Figure 2 illustrates a typical shear buckling pattern in the honeycomb core composite sandwich panel.

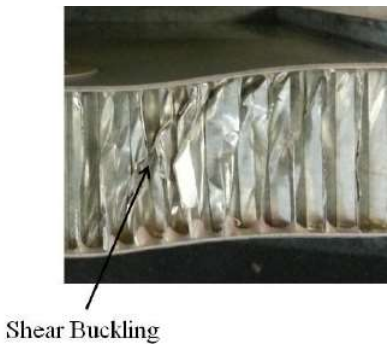

Figure 2. Honeycomb Panel Showing Shear Buckling Failure Mode.

Although material characterization, mechanical testing, and design verification studies such as thermal cycling and vacuum testing are critical for specific mission assurance, experimental prediction of the structural integrity of an exhaustive range of space structures under the various anticipated thermomechanical loading environments is not feasible. Therefore, it is beneficial to develop improved models and analysis tools to better understand the thermal stability and damage tolerance of complex sandwich structures and predict useful residual life accurately.

1.6 Objectives of the work

Following are the primary objectives of this research work:

- Develop a high-fidelity microscale model for CFRP composites with radially-grown CNT architecture that utilize nanoscale derived elastic and inelastic information and variation in the architectural parameters to estimate the nanocomposite properties at higher length scales efficiently.
- Develop a thermodynamically admissible bridging technique to efficiently transfer inelastic information from discrete atomistic MD simulations of the radially-grown CNT interphase to higher length scales using a continuum damage mechanics approach.
- Investigate the linear and nonlinear effects of the unidirectional CFRP composites with radially-grown CNT architecture under mechanical loading, using the developed atomistically informed damage model; investigate effects of damage initiation and propagation with and without the presence of radially-grown CNTs.
- Develop a reduced-order approximation of the high-fidelity microscale model to reduce the computational cost and memory requirements of repeated micromechanics

simulations and efficiently transfer the homogenized microstructural response to higher length scales to analyze built-up structural components.

Following are the secondary objectives of this research work:

- Investigate failure mechanisms and capture the intrinsic nonlinear material behavior of specific aerospace-grade aluminum honeycomb core and CFRP composite face sheets.
- Investigate the thermomechanical performance of complex honeycomb core composite sandwich space structures with adhesively bonded fittings exposed to extreme temperature ranges using high-fidelity computational modeling techniques.

1.7 Outline

The report is structured as follows:

Chapter 2 presents an atomistically-informed continuum damage mechanics (CDM) model for the radially-grown CNT-fiber-matrix interphase region, with a damage evolution equation developed from the results of elastoplastic MD simulations. The approach bridges the nonlinear deformation obtained from discrete MD simulations to the sub-micro scale efficiently.

Chapter 3 details a microscale model's development based on the HFGMC theory, which integrates nanoscale elastic and inelastic information of the radially-grown CNT interphase using the atomistically-informed CDM damage equations, and idealized composite microstructure. The predicted homogenized response is verified and benchmarked against available experimental data and literature models. The influence of various material and process parameters on the homogenized nanocomposite response at the microscale is investigated.

Chapter 4 presents the development of a surrogate model for advanced composite materials based on a novel adaptation of nonuniform transformation field theory in conjunction with the HFGMC micromechanics theory. The developed surrogate model is trained to predict the global and local nanocomposite microstructural response with significantly decreased computational time and memory requirements.

Chapter 5 presents an investigation into the thermomechanical performance of complex composite sandwich structures with adhesively bonded fittings subject to cyclic thermal loading using FE analyses. Additionally, sandwich panels with different configurations were chosen to investigate the nonlinear effects such as shear buckling in the honeycomb core and the damage progression in CFRP composite face sheets under different loading conditions.

Last, essential contributions and conclusions derived from this research work and possible future investigations that extend upon the present work are discussed in Chapter 6.

CHAPTER 2

DAMAGE FORMULATION FOR NANOENGINEERED FIBER-MATRIX INTERPHASE

2.1 Introduction

The recent effort on growing or grafting CNTs on the surface of fibers (radially-grown) has shown to offer some advantages over other CNT reinforcement techniques (Sharma and Lakkad 2011; Wicks et al. 2010). The introduction of CNTs in composites through CNT deposition/growth on the fiber surface provides a higher control over CNT orientation, length, and density (Carpenter et al. 2011). Radially-grown CNT architecture shows increased potential for mechanical reinforcement as they offer improved load transfer between the fiber/matrix interface and increased interfacial shear strength (IFSS) (Qian et al. 2008; Wang et al. 2014). Huang et al. (2013) studied the effect of multi-wall CNTs dispersed in the matrix and radially aligned in the fiber/matrix interface. The authors concluded that the reinforcing effect is more pronounced when CNTs are added to the fiber instead of the matrix. They reported a 24.42% increase in transverse strength and a 15.47% improvement in interlaminar shear strength (ILSS). Karapappas et al. (2009) reported that highly condensed deposition of CNTs on fiber surfaces increases the fracture energy by 45%-75%. Garcia et al. (2008) used different aspect ratios of CNTs vertically aligned in the fiber/matrix interface and reported a 150%-300% improvement in toughness. Most recently, it was shown that the surface treatment of carbon fiber fabric and incorporation of CNTs significantly improved the dynamic properties such as storage modulus and energy absorption capabilities compared to neat polycarbonate/carbon fiber composites (Cho et al. 2019). Consequently, using radially-grown CNTs on the fiber surface as a promising

means for nanoscale reinforcements has attracted their manufacturability and use. However, a significant challenge to optimizing them for a specific application is the lack of comprehensive modeling techniques that adequately capture the nanoscale effects of radially-grown CNTs on fiber to the bulk properties of the composites at higher length scales.

Recent studies have shown that the nanoscale information of CNT-enhanced composites is integral to understanding their material-structure property and can lead to successful strategies for scaling material behavior from the nano- and microscale to the macroscale (Subramanian, Rai, and Chattopadhyay 2015; J. Zhang et al. 2016). Computational models based on molecular dynamics (MD) simulations can describe the complex bonded and nonbonded interactions between atoms of the individual material constituents and provide essential insights into the composite's macroscopic behavior and material properties. They can also provide time-dependent information on material evolution.

In this chapter, modeling the interphase region of CFRP composite with radially-grown CNT architecture is discussed first. The creation of radially-grown CNTs in a simulation volume containing the epoxy resin, hardener molecules, and fiber surface is explained. The effect of varying CNT concentrations on the nanocomposite interphase's elastic-plastic and damage response is also evaluated through atomistic virtual deformation tests. The subsequent section briefly outlines the procedures to perform the virtual deformation tests using MD simulations. In the last section of the chapter, an atomistically-informed continuum damage model with internal variables representing polymer mechanics and damage evolution for different CNT concentrations in the interphase is developed to accurately simulate the response and complicated damage process in the radially-grown CNT-fiber-matrix interphase region.

2.2 Nanoscale Model

MD simulations are performed at the nanoscale to inform the continuum level HFGMC framework. The radially-grown nanocomposite model at the atomistic scale is comprised initially of five constituents: carbon fiber surface, polymeric functional coating (PSMA), radially-grown CNTs, the epoxy resin, and the crosslinker (see Figure 3). The carbon fiber surface is simulated with void-induced, irregularly-stacked graphene layers to simulate surface roughness; radially-grown CNTs are embedded in the PSMA chains; they are physically dispersed with no functionalization. The epoxy consists of DGEBF (Di-Glycidyl Ether of Bisphenol F) as the resin and DETA (Di-Ethylene Tri-Amine) as the crosslinker, before curing, dispersed randomly in the unit cell inside a predefined box. The unit cell dimensions are $40 \times 45 \times 35$ nm^3.

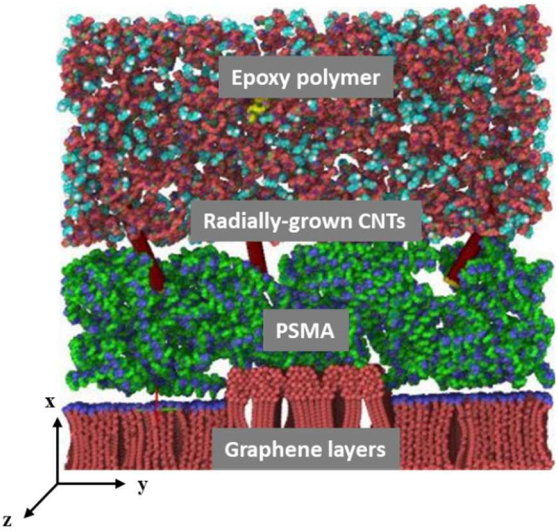

Figure 3. Atomistic Model of Radially-Grown CNT Architecture Interphase Region.

A detailed description of the model setup, choice of force fields, and epoxy crosslinking simulations can be found in Subramanian et al. (2018). The MD simulations for the radially-grown nanocomposite are performed with hybrid classical force fields initially. The

simulations implement PBCs along the y- and z-directions. However, the assumption of PBCs is not appropriate along the x-direction due to a phase discontinuity (at the interphase). In this work, the focus was to capture the effect of CNT areal density (the number of CNTs per nm^2 graphene layer) on the elastic, elastic-plastic, and damage initiation characteristics of the fiber/matrix interphase with radially-grown CNTs. This is achieved by developing a molecular model with a fixed number of graphene sheets, PSMA, and epoxy molecules. Radially-grown CNTs of chirality (10,10) are embedded in the PSMA chains that are physically dispersed with no functionalization. Due to the high computational costs incurred by large-scale molecular systems, the modeling of radially-grown CNTs with heights in the order of microns is not feasible via MD simulations. Hence, the length of the CNT is chosen to be only ~ 10 nm. However, it is assumed that the relative fraction of the interphase region is of critical relevance and is used as an input to model the interphase at the higher length scale. The relative fraction is estimated as the ratio between the height of the CNT and the thickness of the interphase (defined by the unit cell's height) along the CNT growth direction. In this present atomistic model, the relative fraction of the interphase region is calculated to be ~ 0.25. The number of radially-grown CNTs is varied to capture a short range of areal densities. It should be noted that the intermolecular forces of repulsion between the CNTs dictate the upper limit of CNT areal density.

Equilibration and crosslinking MD simulations are performed first using classical force fields. The Optimized Potential for Liquid Simulations – All Atom (OPLS-AA) (Jorgensen et al. 1996) and the Consistent Valence Force Field (CVFF) (Zang et al. 2009) defines the crystalline CNT and graphene molecules, respectively. The thermoplastic PSMA chains and the thermoset epoxy molecules utilize the Merck Molecular Force Field (MMFF) parameters (Halgren 1996). The deformation MD simulations are performed using a reactive force field

(ReaxFF) (Singh et al., 2013) to capture bond elongation and bond scission events. A tensile load is applied to the molecular model by uniformly deforming the simulation box along the y-direction. The applied strain translates to the elongation of bonds, causing the atoms to be remapped, and the equivalent stresses are obtained from the spatial and temporal averaging of virial stresses (Subramaniyan et al., 2008). Subramanian et al. (2013) developed an ultra-high strain rate approach to decouple the thermal relaxation of bonds and capture the effect of bond elongation and breakage purely based on mechanical deformation. Therefore, the obtained response is a quasi-continuum-equivalent deformation of the molecular system. The variation of bond energy between the molecular model's unbound state at the initial step and at each time step of the simulation is used to calculate the bond dissociation energy. As deformation occurs, the bond energy lost due to dissociation of each covalent bond in the system is calculated and defined as BDE. Further details of the boundary conditions and accompanying justifications are provided in Subramanian et al. (2018).

It was concluded from a previous atomistic scale investigation of the radially-grown CNT fiber interphase that failure of this region is dominated by the mechanisms arising from loads transverse to the CNT growth direction (*y*-direction in the atomistic model in Figure 3). These observations were justified by comparing the obtained maximum value of bond dissociation energy and the respective failure strains for different loading directions. A significant hypothesis that emerged subsequently was that, while the elastic behavior along *y*-direction was due to loads being transferred through polymer chain stretching, the CNTs reorient themselves to fill the voids caused by polymer chain extension. This reorientation of CNTs happens along the loading direction; thus, strain-hardening tendencies were observed beyond the elastic regime. Further information on the MD model and the nanoscale stress-strain response curves can be found in Subramanian et al. (2018). Figure 4 illustrates the smoothed

elastoplastic stress-strain response from virtual deformation simulations conducted for different CNT areal densities. In the elastic regime, the polymer chains in the interphase region are stretched along the direction of applied stress. In the yielding regime, the molecular configuration deforms and rearranges irreversibly. After yield, strain-softening occurs due to the breakage of polymer chains due to subsequent bond dissociation. When strain softening is complete, strain hardening behavior emerges due to the subsequent realignment of CNTs along the loading direction in the newly generated voids. In the failure regime, the spacing between the CNT and the matrix increases, contributing to a secondary softening regime that leads to the complete failure of the interphase material. This phenomenon cannot be determined and verified experimentally; however, the simulations provide insights into important nanoscale trends while considering the local interactions between the CNT, graphene layers, and polymer matrix and the influence of different CNT areal densities.

In a recent study, a molecular system with randomly distributed CNTs was generated to investigate the effect of nano-inclusions by weight fractions on the polymer cross-linking formation (Subramanian et al., 2015). It was observed and quantitatively shown that the increase in CNT weight fraction reduced the polymer's mean crosslinking degree. However, the gradient of reduction in crosslinking degree reduced at a much higher weight fraction due to the formation of CNT clusters causing localized highly crosslinked polymer regions. This formed the basis that the CNTs interferes with the crosslink formation between the resin and the hardener molecules. A similar reduction in the polymer crosslinking degree in the present radially-grown CNT architecture is observed with an increase in CNT areal density. Therefore, the increase in CNT areal density in the interphase region results in a considerable decrease in the transverse elastic modulus. However, the slope of the hardening phase in the stress-strain curve increases with an increase in the areal density. Figure 5 shows the associated bond

dissociation energy (BDE) variation during the deformation simulations transverse to the CNT growth direction for varying CNT areal densities. The slope of the BDE curve with respect to strain indicates how much energy is expended for bond breakage from the applied deformation. The initial increase in the BDE curve slope up to ~2 % strain indicates that the bond energy is lost due to the stretching and scission of low strength sp^3 bonds. After the polymer phase's failure, the BDE curve saturates beyond ~4% strain, and the slope drastically reduces due to load transfer to the radially-grown CNTs. It is important to note that the rate of damage saturation (bond dissociation) increases with an increase in the areal density and leads to a notable increase in the hardening phase. These nanoscale physical phenomena unique to radially-grown CNT architectures could be attributed to increased strength and toughness properties at higher length scales. The obtained stress-strain response and bond dissociation energy (BDE) variation, which provide vital insights into these damage mechanisms, are used to derive constitutive equations in the microscale continuum damage model described in the next section.

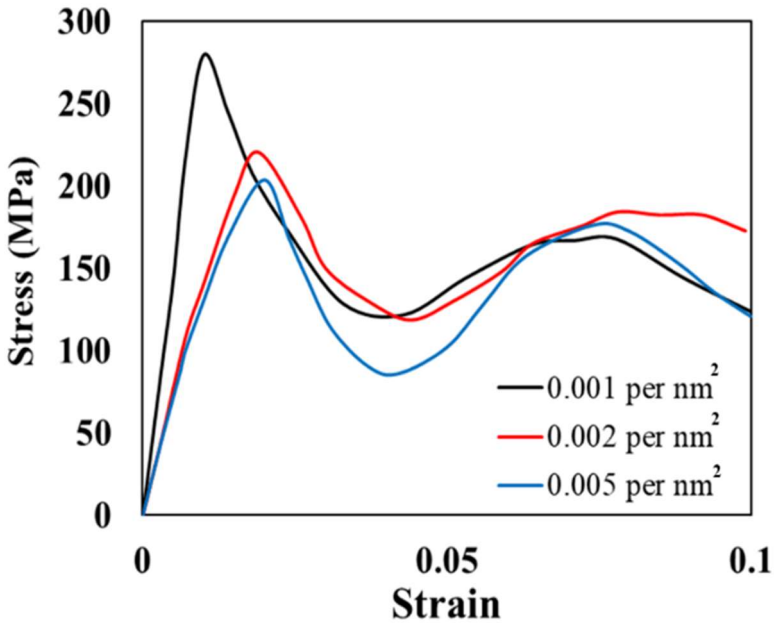

Figure 4. MD Model Response for Different CNT Areal Densities

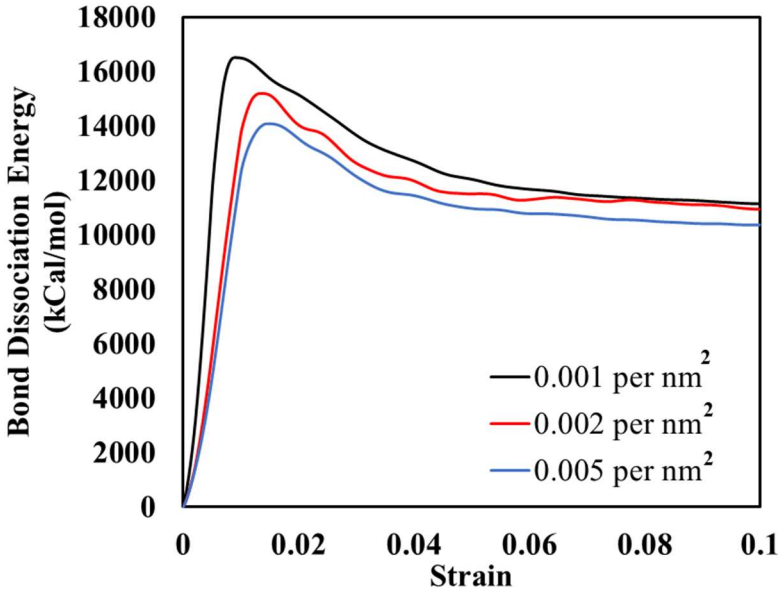

Figure 5. Instantaneous BDE Response for Different CNT Areal Densities

2.3 Sub-microscale Model

Motivated by the previous MD simulation results, it is necessary to accurately model the complex damage saturation and prominent strain hardening mechanism in the radially-grown CNT architecture. A constitutive material model for the interphase region is developed based on the CDM framework, with damage evolution equations developed from elastoplastic MD simulation results. Firstly, the interphase region is modeled as an orthotropic material at the sub-microscale. Figure 6 (a) shows the local coordinate system defined by the fiber inclusion in the x_1 direction and the radially oriented CNTs in the orthotropic material frame (x_2-x_3). The six independent elastic parameters in the orthotropic material are obtained from the tensile and shear deformation MD simulations of the atomistic interphase model described in the previous section. The three independent Poisson's ratios are carefully estimated to ensure a positive-definite symmetric elasticity tensor C_{ijkl}.

In the CDM framework, constitutive equations and evolution laws of state variables are derived from the damage-coupled energy potentials. In the present study, based on the hypothesis of decoupling between elastic damage and plastic hardening (Zhu and Cescotto 1995), the Helmholtz free energy density is expressed as

$$\psi = \psi_e\left(\epsilon_{ij}^e, D_{ij}\right) + \psi_p(\xi, T) \tag{2.1}$$

where $\psi_e(\epsilon^e, D)$ is a coupled damage-elastic strain energy and $\psi_p(\xi, T)$ is the free energy contribution due to plastic strain hardening, ϵ_{ij}^e is the elastic strain tensor, ξ is an internal variable representing the equivalent plastic strain $\bar{\epsilon}^p$, T is the temperature and the tensor D_{ij} is the internal variable associated with damage.

With the additive decomposition of the strain rate $\dot{\epsilon} = \dot{\epsilon^e} + \dot{\epsilon^p}$ and using the Clausius-Duhem inequality under isothermal conditions, the following relation can be obtained.

$$\gamma = \sigma : \dot{\epsilon}^p - \frac{\delta\psi_e}{\delta D}\dot{D} - \frac{\delta\psi_p}{\delta\bar{\epsilon}^p}\dot{\bar{\epsilon}^p} \geq 0 \tag{2.2}$$

where γ is the power of dissipation. The thermodynamic conjugate forces corresponding to the internal variables are derived from the free energy term and are expressed as

$$\sigma_{ij} = \frac{\delta\psi}{\delta\epsilon_{ij}^e} = C_{ijkl}\epsilon_{kl}^e\,, \tag{2.3}$$

$$Y_{ij} = -\frac{\delta\psi}{\delta D_{ij}} = \frac{1}{2}\epsilon_{kl}^e\frac{\delta C_{klpq}}{\delta D_{ij}}\epsilon_{pq}^e \tag{2.4}$$

$$\kappa = \frac{\delta\psi}{\delta\bar{\epsilon}^p} \tag{2.5}$$

where σ, Y and κ are the thermodynamic affinities associated with the elastic strain ϵ^e, damage D and the plastic strain due to molecular rearrangement in the polymer ϵ^p respectively.

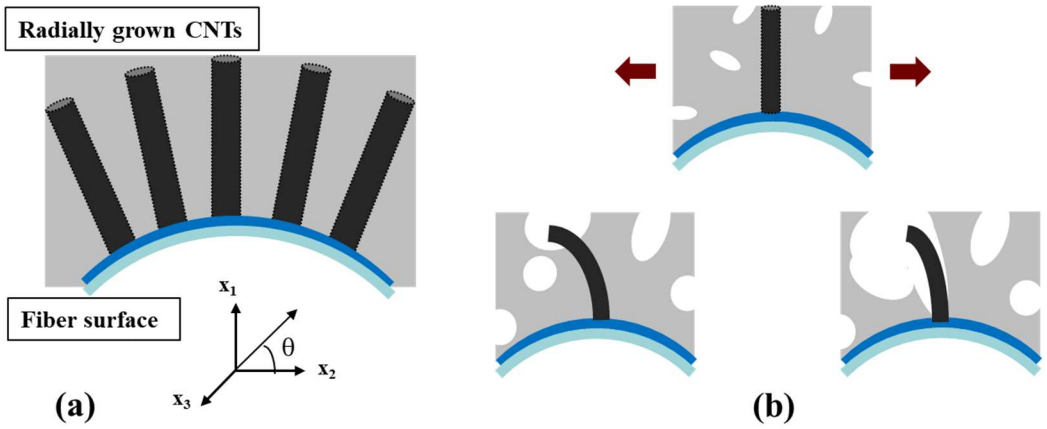

Figure 6. (a) Local Coordinate System; (b) Deformation Stages under Transverse Loading

2.3.1 Constitutive Equations

Using strain equivalence principle and assuming damage components in each direction evolve independently, the following relation for the coupled elastic-damage strain energy term can be obtained.

$$\psi_e = \frac{1}{2}\epsilon_{ij}^e(1 - D_{ij})C_{ijkl}\epsilon_{kl}^e \tag{2.6}$$

By substituting the strain energy expression from Eq. (2.6) in Eq. (2.3), the coupled elastic-damage law can be expressed as follows.

$$\sigma_{ij} = (1 - D_{ij})C_{ijkl}\epsilon_{kl}^e \tag{2.7}$$

It is important to note that in the present work, the primary goal is to capture specific nano and sub-microscale features that could be attributed to the enhancement in out-of-plane properties of radially-grown nanocomposites. As observed from atomistic simulations, interphase failure under transverse loading is more predominant than the deformation behavior along the direction longitudinal to the CNTs. The interphase region exhibits complex mechanisms such as plasticity, damage-softening, rehardening, and failure along the transverse

direction. Figure 6 (b) illustrates the various stages of deformation under transverse loading and the damage variable D_2, characterizes the corresponding damage evolution, as shown in Figure 7. Along the x_3-direction, the absence of a matrix-dominated softening mechanism is attributed to the load-carrying role dominated by the graphene layers. Therefore, the interphase deformation along this direction is assumed to be linearly elastic. Consequently, a thermodynamically consistent model is implemented by defining a yield function to initiate failure along the transverse (x_2) direction.

$$\phi_p = \frac{\sigma_{eq}^*}{1 - D_2} - \sigma_{y_0} - \kappa \leq 0 \tag{2.8}$$

where σ_{y_o} represents the yield stress in the referent direction, σ_{eq} is the equivalent stress, and κ is a scalar thermodynamic force associated with the plastic strain hardening, characterizing the expansion of the yield surface. A nonlinear plastic strain hardening free energy term is assumed and can be written as

$$\psi_p = C_h(\bar{\epsilon}^p)^\gamma \tag{2.9}$$

where C_h and γ are the hardening modulus and hardening index representing the internal stresses developed by the polymer chain rearrangement and the subsequent realignment of CNTs along the loading direction. Substituting the above free energy term in Eq. (2.5), the thermodynamic force associated with hardening is obtained as

$$\kappa = \gamma C_h(\bar{\epsilon}^p)^{\gamma-1} \tag{2.10}$$

Under the associative flow, Eq. (2.8) defines the stress function as a yield function and plastic potential. With negligible plastic deformation along the x_1- and x_3-direction, the plastic strain evolution equation in the x_2-direction is obtained using the classical plasticity conditions and can be expressed as

$$\dot{\epsilon}_{ij}^{p} = \dot{\lambda}\frac{\delta\phi_p}{\delta\sigma_{ij}} = \frac{\dot{\lambda}}{1-D_2}\frac{\delta\sigma_{eq}}{\delta\sigma_{ij}} \tag{2.11}$$

where $\dot{\lambda}$ represents the viscoplasticity multiplier and is described as

$$\dot{\lambda} = \frac{1}{K_v}\left[\left(\frac{\phi_p + \sigma_{y_0}}{\sigma_{y_0}}\right)^{\frac{1}{\mu}} - 1\right] \tag{2.12}$$

where K_v and μ are viscoplastic constants.

2.3.2 Damage State Variable

The nanoscale mechanics of the interphase region derived using MD simulations show that the CNT areal density governs the out-of-plane properties of radially-grown nanocomposites. At the continuum scale, the CNT areal density is defined as the number of CNTs grafted or grown per μm^2 of the fiber surface. Along the transverse direction, the post-yield softening and strain hardening behavior are mainly due to the polymer bond breakage, molecular rearrangement, and consequent reorientation of CNTs at the nanoscale. In the present formulation, a damage evolution equation based on BDE variation is developed to surrogate the nanoscale damage kinetics in the CNT reinforced interphase region.

To model the proposed multi-stage deformation behavior illustrated in Fig. 6 (b), a damage variable D_2 is introduced to characterize the corresponding damage evolution along the y-direction. Two distinct softening variables are introduced to account for the dual softening behavior observed in the MD simulations. The BDE variation shown in Fig. 5 is used to model the evolution of the primary damage variable D_s. It is important to note that the calculated BDE variation from the MD simulations shown in Fig. 5 plots the instantaneous difference in bond energy due to the breakage of covalent bonds in the system. The calculated variation

accounts only for the bond breakage and does not consider the cumulative variation of bond breakage energy converted to non-bonded pair energy interactions. A damage saturation law is assumed to characterize D_s and the point of damage saturation is calibrated from the BDE curve for the corresponding value of strain. The evolution of the secondary damage variable D_f is developed to simply surrogate the final drop in the stress-strain curve obtained from the MD simulations. The atomistic interphase model shows a considerable decrease in transverse modulus with an increase in areal density. This behavior is ascribed to the increase in local stress concentrations in the polymer due to the increase in the CNT volume concentration. However, the rate of damage saturation and hardening mechanism is more prominent with increased areal density. Hence, the damage evolution equation is developed to reflect this change of nature of the damage with a change in CNT areal density and is expressed as

$$\dot{D}_s = \frac{\dot{\lambda}}{2}\left(\frac{(1+\alpha) - D_s\rho^{\eta}}{\rho^{\eta}}\right)Y^{\xi} \tag{2.13}$$

$$\xi = \alpha\rho^{\eta} \tag{2.14}$$

where ρ is the CNT areal density, α is a phenomenological constant associated with the damage saturation when the realignment of CNTs is complete, and η is the rate of damage growth. To capture the dual softening behavior, a secondary damage variable, also called the failure variable, is obtained as

$$\dot{D}_f = \frac{\dot{\lambda}}{2}\left(\frac{Y}{Y_0\sqrt{1-D_f}}\right) \tag{2.15}$$

where Y_0 is a material parameter associated with the slope of the secondary softening curve. The variation of damage evolution versus applied strain shown in Figure 5(a) gives the combined response of the two-distinct damage variable, contributing to the dual softening

stress-strain response. As a validation process, the combined damage response is compared with the cumulative BDE variation obtained from the MD simulations of the radially-grown CNT interphase region (Subramanian et al., 2018). Figure 8 (a) shows the obtained BDE variation as a function of the applied strain for a CNT areal density of ~ 0.003 per nm^2. It should be noted that this BDE variation is calculated by considering energy due to bond breakage and the non-bonded pair energy variations, which gives the cumulative variation of the deformation response. Figure 8 (b) shows the normalized BDE variation and the damage evolution for a CNT areal density of ~ 0.003 per nm^2. The predicted cumulative damage evolution shows a good correlation with the normalized cumulative BDE variation. It is important to note that the assumed damage evolution equation is based on an exponential saturation law, while the obtained BDE curve shows a highly non-linear response. It is also worth mentioning that the developed damage evolution model sufficiently captures critical characteristics such as a change in gradient and damage saturation. The variation of stress-strain response with CNT areal density is shown in Figure 7 (b). At high CNT density, the model predicts improved damage saturation and a more prominent hardening behavior than lower CNT density, where the stiffness improves. The change in gradient and slope of the damage curve are the critical features of interests sufficiently captured by the developed damage evolution model.

The developed constitutive model considers the variation of material behavior with CNT density in the direction transverse to the radially-grown CNTs. Hence, a relationship between transverse yield strength and CNT density, ρ, is derived through molecular dynamics simulations. The yield point is computed using MD simulations with appropriate force fields as described in the previous section. From the simulation results, the yield strength for a range

of CNT areal density was calculated using virtual deformation tests along the x_2-direction. The linear fit model was found to have the following form.

$$\sigma_{y_o} = 135.5 - 0.0076\rho \tag{2.16}$$

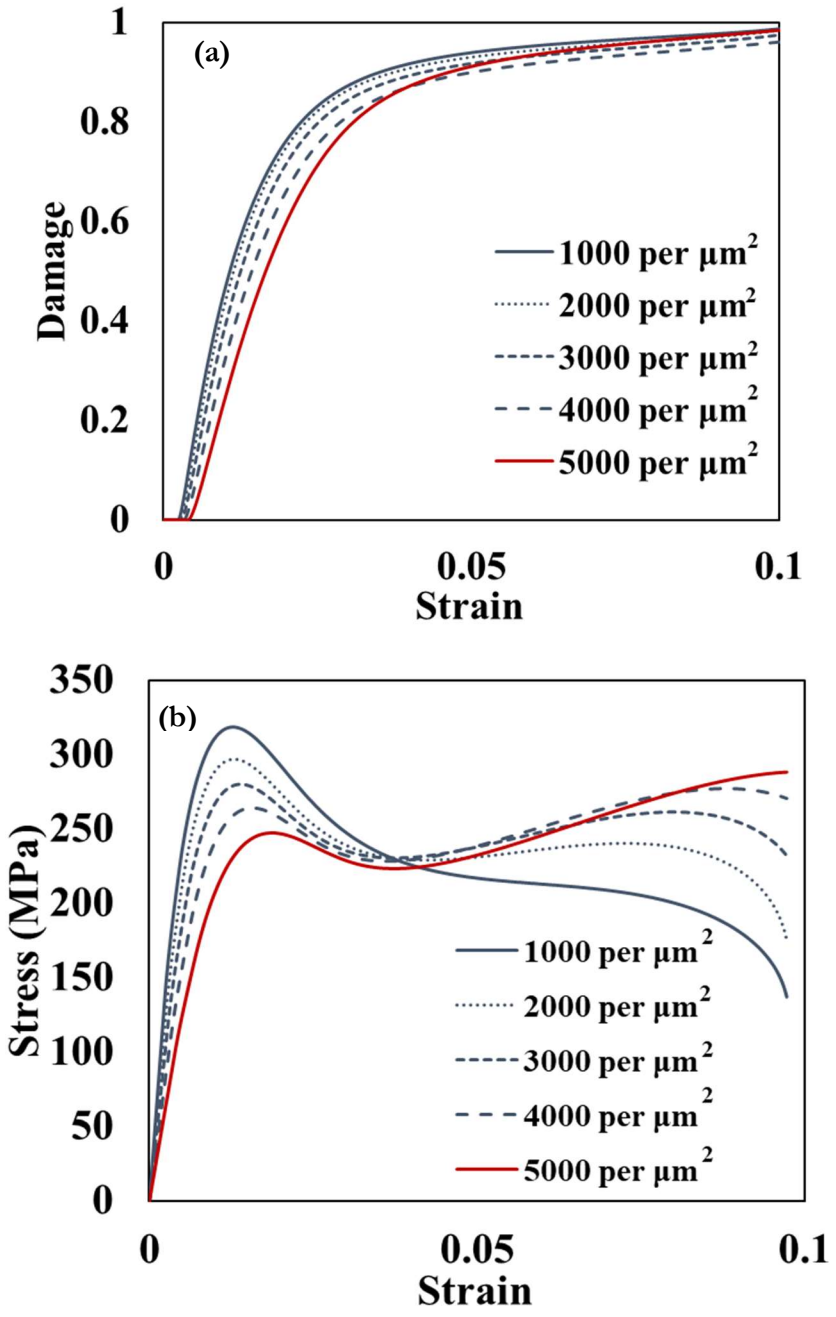

Figure 7. Interphase Model Prediction of: (a) Cumulative Damage; (b) Stress Vs Strain

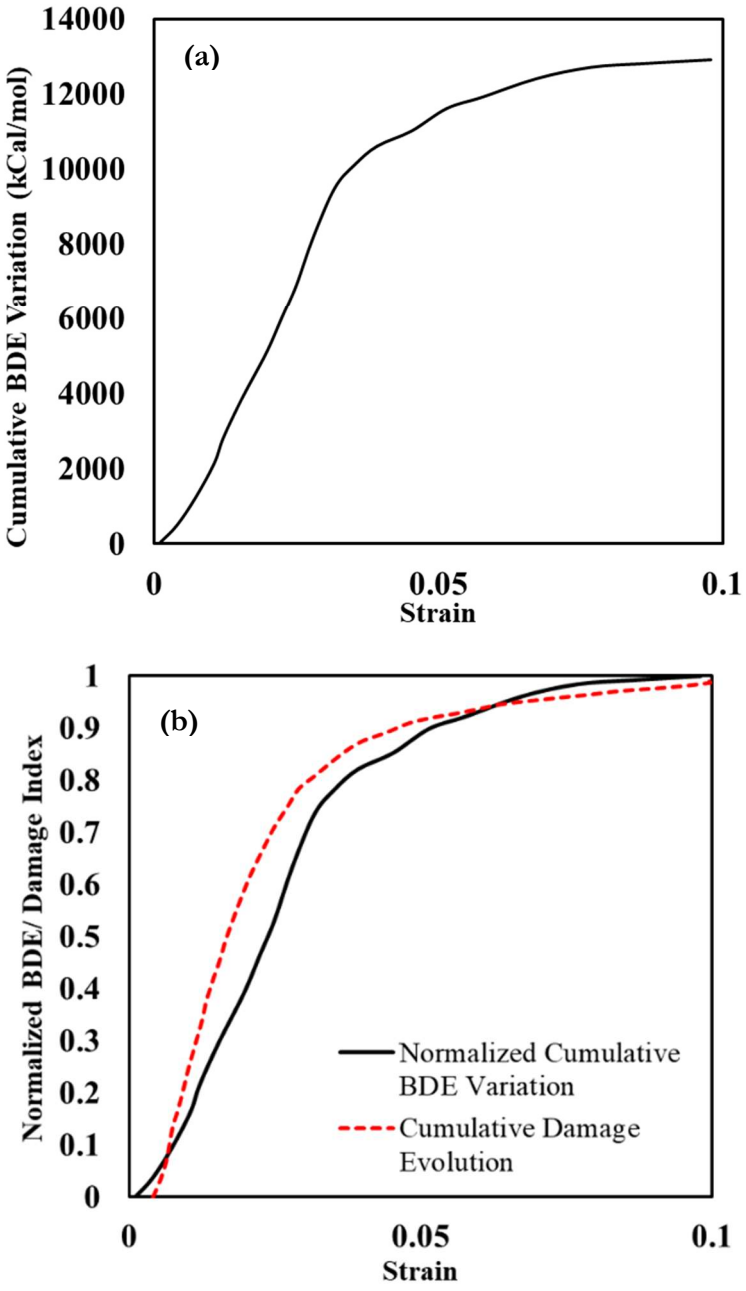

Figure 8. (a) Cumulative BDE Response; (b) Comparison with Damage Model

2.4 Summary

This chapter introduced the development of a constitutive law for radially-grown CNT architecture based on the CDM framework and in conjunction with a damage evolution

equation developed from nonlinear MD simulation results using reactive force fields. This thermodynamically admissible framework uses various ISVs to define material damage and hardening, based on MD simulations of covalent bond breakage under mechanical loading. The developed damage formulations were benchmarked by comparing the damage evolution trend with the bond dissociation energy variation curve obtained from MD simulations.

Since these formulations utilize the energy form of the inelastic information obtained from MD simulations, successful nonlinear information transfer between the nanoscale and continuum scale is possible in a computationally efficient manner. Additionally, the atomistically informed damage model was also used to provide insight into the manner of damage accumulation in the heterogenous radially-grown CNT-fiber-matrix interphase region. The CDM-based atomistically informed damage model is applied to study the inelastic behavior in radially-grown CNT nanocomposites in the subsequent chapter.

CHAPTER 3

MICROMECHANICS OF RADIALLY-GROWN CNT ARCHITECTURE

3.1 Introduction

The presence of radially-grown CNTs in the fiber-matrix interphase region leads creates an additional layer of stiffness around the interface at the microscale (Wood et al. 2012). The stress concentrations in the fiber/matrix interface are likely to shift from the fiber surface to the ends of the CNTs, thereby changing the damage initiation and progression (Matveeva et al., 2019; Romanov et al., 2015). As a result, a significant impediment to capturing the influence of radially-grown CNTs on the composite response is the intrinsic heterogeneity in the fiber-matrix interphase region. Moreover, the prediction of strength and toughness is further exacerbated due to the multiscale nature of the damage and failure mechanisms/interactions such as fiber-matrix interfacial debonding, matrix cracking, and CNT/matrix interfacial debonding (Gorbatikh et al. 2016).

Several studies have reported predicting the mechanical properties of carbon fiber-reinforced polymer (CFRP) composites with radially-grown CNTs, also known as fuzzy fiber reinforced polymer composites (FFRP), using a multiscale modeling approach. Chatzigeorgiou et al. (2011) used a two-step homogenization procedure of a three-phase unit cell to estimate composites' effective properties with the nano-reinforced interphase region. Chatzigeorgiou et al. (2012) also used the asymptotic expansion homogenization method to numerically estimate the effective mechanical properties. Lurie et al. (2018) used a generalized self-consistent (GSC) method to obtain analytical estimates for the effective mechanical characteristics of radially-grown CNT composites. Other hierarchical modeling approaches

include both deterministic (Kundalwal and Ray 2011, 2012) and stochastic techniques (Raifee and Ghorbanhosseini 2017) to estimate the effective properties using material properties of the individual constituents. A three-dimensional (3D) hierarchical multiscale model of the radially-grown CNT architecture was developed (Malekimoghadam et al., 2019). The CNTs were initially modeled using a 3D shell lattice structure and then reconstructed as nanofibers using an equivalent continuum modeling technique. The fiber-matrix interphase region of the microscale RUC was then modeled using an effective properties approach. However, these hierarchical methods are generally limited to predicting elastic properties and do not account for the fundamental level damage mechanisms and interactions across multiple length scales.

FE-based concurrent multiscale models were proposed for a synergistic analysis of the nano- and microscale reinforcements using solid continuum elements. Dai et al. (2015) used microscale RUCs to predict the fatigue performance of unidirectional CFRP composite with radially-grown CNTs using extended FE methods. Microscale RUCs with explicitly modeled microfibers, matrix, and individual 3D CNTs were built with accurate dimensions and meshed using the embedded element technique (Romanov et al., 2014; Rai et al., 2018). The FE-based microscale RUCs were used to investigate the stress heterogeneity in the fiber-matrix interphase region due to the presence of CNTs (Romanov et al., 2015). Additionally, the interactions between the various nano- and microscale damage mechanisms were incorporated using a combination of embedded and cohesive elements (Lu et al. 2019; Liu et al. 2019). Liu et al. (2020) used such techniques to demonstrate the influence of radially-grown CNTs on composite properties such as strength and toughness. While these techniques can be used to scrutinize improvements in the composite behavior, an accurate prediction requires physics-based constitutive laws and scale bridging mechanisms that account for the complex bonded and nonbonded interactions between the individual constituents at the fundamental (nano)

length scale. Recently, molecular dynamics (MD) simulations were conducted to investigate interactions in the fiber-matrix interphase region with radially-grown CNTs (Subramanian et al. 2018). The MD approach adequately captured the complex deformation and various competing energy dissipating mechanisms at the nanoscale, such as polymer bond breakage, chain entanglement, and CNT/polymer debonding due to van der Waals separation.

In the previous chapter, the MD methodology was used to investigate the effects of varying CNT concentrations on the out-of-plane mechanical response of the radially-grown CNT-fiber-matrix interphase region. An atomistically-informed hierarchical constitutive law was then developed to capture the transition of nanoscale damage phenomena to the continuum length scale. In this chapter, the developed damage model in conjunction with the atomistically-informed damage model for thermoset polymers developed by Rai et al. (2016) is further applied to a radially-grown CNT nanocomposite RUC within the HFGMC micromechanics framework, while fiber failure is disregarded. The framework is then extended to study the influence of various material and process parameters on the microscale's homogenized composite response. First, the predicted elastic property is compared to existing model predictions and experimental data in the literature for verification and benchmarking. The multiscale model is then used to quantify the effects of input parameters such as CNT areal density and fiber-matrix interphase thickness (CNT height), polymer crosslinking degree, and fiber volume fraction on the predicted composite elastic properties, strength, and toughness. The validation of these predictions at the microscale can be done once the experimental data becomes available. However, the parametric study's results provide essential insights into the sensitivity of the design parameters for improving macroscopic response. The information is key to understanding and optimizing the architecture of CNT-embedded composites for specific applications. Last, the multiscale model is used to predict fiber stresses

and the onset of microscale damage in the out-of-plane loading direction to capture the energy dissipation mechanisms attributed to the enhancement in composite strength and toughness at higher length scales.

3.2 Micromechanical Model

The previous chapter observed that the CNT areal density in the interphase region affects the out-of-plane properties significantly. Therefore, the local fiber/matrix interphase region is modeled at the micro length scale to quantify the influence of the CNT areal density and the other constituent properties on the global response of radially-grown nanocomposite. The HFGMC micromechanics theory is employed to capture these effects. The HFGMC theory is based on the homogenization procedure for heterogeneous composites with periodic microstructure. The theory centers on a semi-numerical approach that provides a compromise between fidelity and efficiency via a two-way flow of information between length scales. The nanocomposite RUC is defined by a continuous long fiber inclusion in a polymer matrix along the y_1-direction. The microscale unit cell is periodically distributed in the $y_2 - y_3$ plane and is discretized into several sub-volumes, known as subcells (see Figure 9). The microscale RUC is discretized using 40x40 subcells in the $y_2 - y_3$ plane and set to one subcell along the fiber direction (y_1). A higher-order multiaxial displacement field is employed, resulting in local shear stresses and strains, particularly in the fiber-matrix interface due to applied global strain. As a result, the model can adequately capture the interfacial stress transfer characteristics between adjacent subcells of different material properties. The volume-averaged and higher-order micro variables, which make up the second-order displacement field, must be determined from a system of governing equations, the interfacial displacement and traction continuity

conditions between all subcells, and the periodic boundary conditions the fluctuating displacement field must satisfy. It is important to note that all the necessary conditions are imposed in an average sense. The obtained micro variables are utilized to compute local subcell strains and stresses. The average stress and strain are estimated by employing the definition of volume average in composites. The effective elastic moduli are readily obtained by establishing the relations between the average stresses and strains in the nanocomposite. The local subcell strains are used to evaluate the constitutive level inelasticity and damage models. The detailed solution procedure for the displacement field can be found in (Aboudi and Pindera 2004).

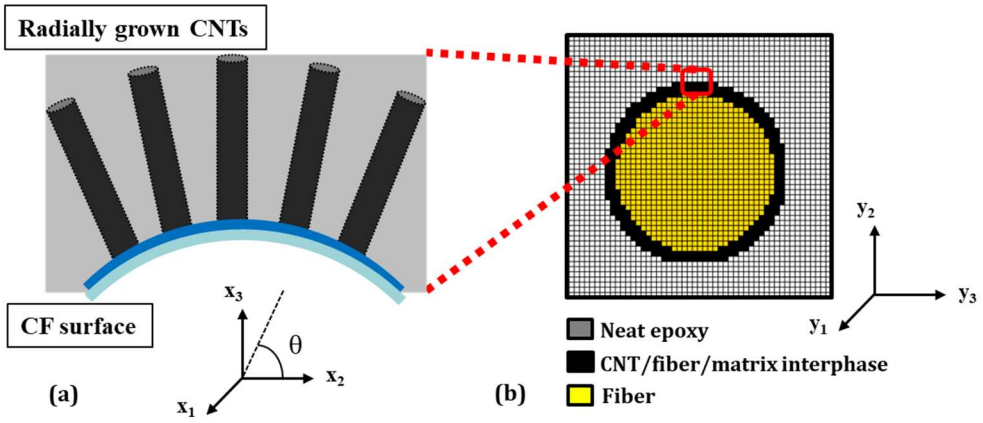

Figure 9. (a) Sub-Micro Scale Interphase Representation; (b) Microscale Unit Cell

In radially-grown CNT architecture, the height of the CNTs is primarily controlled by varying the duration of the growth or deposition process. Experimental investigation suggests that microfibers with relatively short CNTs correspond to an annular (ring-like) growth pattern (Wicks et al., 2014). While increasing the duration of the process yields relatively long CNTs, the annular CNT growth pattern splits into 'mohawks' along the microfiber length. The scope of the developed multiscale framework is limited to capturing the effect of short CNTs that attribute to an annular growth pattern. Hence, the nanoengineered interphase

region is modeled with interphase subcells of uniform thickness adjacent to the fiber subcells, as illustrated in Figure 9 (b). Additionally, the interphase subcells are modeled as cylindrically orthotropic, and the stiffness matrix of the subcells (Fig. 9 (a)) is transformed with respect to the angle formed by the in-plane axis of the unit cell (x_3- direction) to the out-of-plane axis along the fiber (y_1- direction). The strain transformation matrix describes the relationship between the material properties in the interphase coordinate system and the microscale coordinate system. The elastic properties determined from the atomistic simulations of the interphase region are incorporated into the micromechanical model of interphase subcells using the transformation matrix and is expressed as

$$\bar{C}_{int} = T_\epsilon C_{int} T_\epsilon^T \tag{3.1}$$

where the subscript 'int' denotes interphase.

Based on the unit cell presented in Figure 9, a geometrical relationship is derived to estimate the CNT volume fraction V_{cnt} at the microstructure level as a function of the areal density and reinforced interphase thickness at the sub-microscale. If the radially-grown CNTs are evenly spaced and are of uniform heights, the CNT volume fraction can be estimated as

$$V_{cnt}(\%) = \frac{\rho \pi d_{cnt}^2 t_{int}}{D} V_f \times 100 \tag{3.2}$$

where D and V_f are the diameter and volume fraction of the fiber in the RUC, d_{cnt} is the diameter of radially-grown CNTs, and ρ is the CNT areal density at the sub-microscale. The parameter t_{int} characterizes the thickness of the CNT-enhanced fiber/matrix interphase region. The maximum value of CNT volume fraction in the present modeling framework is dictated by the maximum value of CNT areal density and CNT height. In the nanoscale model of the radially-grown CNT/fiber/matrix interphase, the number of CNTs was varied to

capture a short range of areal densities. The intermolecular forces of repulsion dictated the upper limit of this range among the CNTs in the molecular system. Based on the developed molecular system of the interphase, the upper limit was determined to be ~6000 CNTs/ μm^2. Additionally, the CNT-enhanced interphase region in the microscale RUC is assumed to be of uniform thickness around the fiber. As stated before, this attributes to the annular growth-like pattern that corresponds to relatively short radially-grown CNTs of height between 3-5 μm. Based on these grounds, the predictive capabilities of the developed multiscale model may be limited to ~6000 CNTs/ μm^2 and 5 μm CNT height. Figure 10 shows the variation of CNT volume fraction with respect to the number of CNTs grown per μm^2 on a single fiber at 40% volume fraction of fiber and for varying thickness of the interphase region.

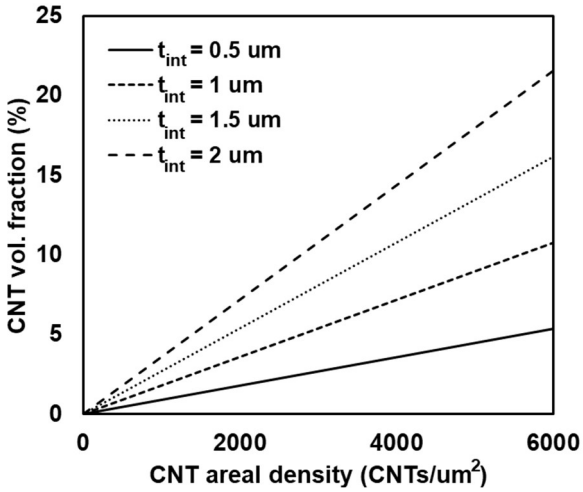

Figure 10. CNT Volume % vs CNT Areal Density for Varying Interphase Thickness

It is important to note that modeling nanoscale interphase with CNT heights in microns is computationally expensive and is not feasible via molecular dynamics simulations. The height of the CNTs in our nanoscale model was chosen to be only ~10 nm. As previously stated, the interphase material consists of quasi-unidirectional nanofibers (CNTs) reinforced in epoxy and radially aligned around the fiber surface. Experiments suggest that the presence

of CNTs leads to the local stiffening of the epoxy, creating a layer of stiffness around the fiber/matrix interface region (Boroujeni et al., 2014; Zhang et al., 2009). Numerical simulation shows that relatively short and dense CNT forests shift stress concentrations away from the fiber surface towards the ends of CNTs (Romanov et al., 2015). This formed the basis of our hypothesis that the presence of CNTs has an extended reinforcing effect in the epoxy matrix. In MD simulations, the unit cell was constructed with a sufficiently large amount of epoxy molecules beyond the ends of the radially-grown CNTs (Subramanian et al., 2018). The ratio of the CNT height to the total height of the epoxy region (relative height fraction) is assumed to be attributed to the extended reinforcing effect around the fiber-matrix interphase region. The relative height fraction is used as a measure to scale the nanoscale interphase model. It is assumed to implicitly account for the CNT's varying heights around the fiber surface at the microscale. In the future, a comprehensive MD investigation of the interphase region for varying relative height fractions is expected to verify this model hypothesis. In the present study, the microscale interphase t_{cnt} is computed using the relative height fraction of ~1.5 estimated from the MD model (Subramanian et al. 2018). For instance, an interphase thickness of 500 nm corresponds to radially-grown CNTs of ~333 nm long in the annular growth pattern.

Each subcell in the unit cell is assigned a material constitutive law to describe the local mechanical behavior. The fiber subcells are defined as transversely isotropic with linear elastic constitutive law. The polymer subcells are defined as isotropic material, while the interphase is modeled as orthotropic. The implementation of the damage model has been performed on a local scale. Therefore, damage evolves in each subcell based on the local stress state. The damage model for polymer matrix and radially-grown CNT/fiber/matrix interphase,

described in the previous subsection, is applied to the RUC within the HFGMC framework. As stated before, the stiffness matrix of the interphase subcell is transformed with respect to the angle formed by the in-plane axis of the local coordinate system (x_1,x_2,x_3) representing the material plane to the axis along the fiber direction (y_1-direction), as illustrated in Figure 9. Therefore, the subcell strain components obtained from displacement field variables are transformed back to the local coordinate system, which is then used to evaluate the local stress state in the material plane. The interphase subcell's local stresses are degraded for the given damage level and are transformed back to the global coordinate system. This process is repeated for each interphase subcell and at each loading increment.

Due to damage, the implementation of this model for post-peak softening analysis will cause strain localization with a resulting mesh-dependency of the numerical results. Although the homogenized elastic properties converge with subcell mesh, some regularization technique is required for post-peak softening behavior based on several methods proposed in the literature. A suitable regularization method for the HFGMC framework will be integrated in the future to mitigate the spurious mesh sensitivity of the softening behavior. Hence, the developed modeling framework's precision is currently limited and not wholly relied on to quantify the post-peak softening response.

3.3 Analysis and Discussion

3.3.1 Model Verification and Benchmark

This section presents results and predictions from the atomistic interphase damage model applied to the high-fidelity micromechanical model. The present modeling framework is validated by comparing the elastic mechanical properties of unidirectional radially-grown CNT

nanocomposite (2% CNT volume fraction) with experimental data from the literature. In Ref. (Kulkarni et al. 2010), radially-grown CNT composite lamina was manufactured with single-wall CNTs of 100 nm height and 30 nm diameter, radially aligned on microfiber surface of diameter 5.2 μm. The microfiber volume fraction of the composite lamina was 40%, with the resulting CNT volume fraction at 2 %, respectively. The relative height fraction (~1.5) of the interphase material is used to scale the thickness corresponding to the 100 nm CNT height. An areal density of ~615 CNTs per μm^2 is estimated using the fiber diameter, volume fraction, CNT diameter, and interphase thickness in Eq. (18). The microscale unit cell is generated with these properties and is subject to boundary conditions corresponding to deformation along the direction transverse to the fiber. The predicted value of the transverse elastic modulus agrees well with the experimental data when the interphase thickness is estimated to be ~ 150 nm (substantially equivalent to 100 nm long CNTs). The specific material properties and input parameters used in the microscale and sub-micro scale constitutive models are summarized in Table 1 and Table 2. It is worth mentioning that the reported experimental data for ultimate strength and failure strain in Kulkarni et al. 2010 was ambiguous. A strength of 29 MPa and a failure strain of 0.28 % was reported, which is too low for a 40 % fiber volume fraction, considering that traditional CFRP composite exhibits much higher strength and strain to failure. As a result, these values could not be used to verify the damage modeling aspects.

Table 1. Elastic Material Properties of Microscale Constituents

Material	E_1 (GPa)	E_2 (GPa)	E_3 (GPa)	G_{12} (GPa)	G_{13} (GPa)	G_{23} (GPa)
Fiber	294	18.5	18.5	7.1	7.1	25

Epoxy (Rai et al. 2017)	2.2	2.2	2.2	0.76	0.76	0.76
Interphase	17.32	15.39	27.61	2.35	4.58	3.16

Table 2. Input Properties for Matrix and Interphase Damage Model

Material	Parameters
Epoxy (Rai et al. 2017)	$Y_0 = 0.12$ MPa, $\eta = 0.40$
Interphase	$\alpha = 0.20$, $\eta = 0.042$

Table 3. Comparison Between Experiments and Microscale Model

	Atomistically-informed HFGMC		Experimental data	
	E_{11} (GPa)	E_{22} (GPa)	E_{11} (GPa)	E_{22} (GPa)
CFRP w/ radially-grown CNT	187¶	10.49ǂ	203 ± 7.6¶ [43]	10.02 ± 1.13ǂ [42]
CFRP	189.33¶	8.25ǂ	198.3 ± 5.0¶ [43]	7.8 ± 1.09ǂ [44]

¶70% Fiber Volume Fraction ǂ40% Fiber Volume Fraction

As shown in Table 3, the predicted longitudinal and transverse modulus obtained from the HFGMC model agrees well with the experimental observations. The predicted elastic response of radially-grown nanocomposite yields up to a 21.3% improvement in the transverse modulus with respect to traditional CFRP composites, as shown in Table 3. However, the longitudinal modulus of the composite deteriorates in the presence of a heterogeneous interphase region. This degradation could be attributed to the interphase region acting as surface defects on the fiber, thereby degrading the load transfer characteristics along the fiber direction.

Table 4. Present Model Benchmarked with Literature and Experiment Data

Method	E_T (GPa)	Error (%)
Experiment (Kulkarni et al. 2010)	10.02	-
Present HFGMC model	10.49	4.7
Generalized self-consistent (GSC) model (Lurie et al. 2018)	10.09	0.69
Finite element model (Kundalwal and Ray 2012)	13.93	39
Mori-Tanaka model (Kundalwal and Ray 2011)	11.91	18.86
Simple unit cell (SUC) model (Hassanzadeh et al. 2018)	10.38	3.5
Effective fiber model (Rafiee and Gorbanhosseini 2018)	11.20	11.7

As shown in Table 4, the transverse Young's modulus predicted using the multiscale model benchmarks well with finite element and analytical methods in the published literature. Although literature models do compare well with experiments, the suitability of those approaches is generally limited to investigating only the effective elastic properties. The present multiscale model can capture fundamental level damage mechanisms and interactions through the atomistically informed damage model and HFGMC theory. It is worth mentioning that existing literature models compared with experiments consider a highly crosslinked polymer with a modulus ranging between 3 to 5 GPa. Moreover, MD simulations of epoxy polymer curing showed the most likely crosslinking degree to be 56 %, with a standard deviation of 15 % (Subramanian et al., 2015). However, in the present multiscale model, a crosslinking degree of 40 % is estimated to show good agreement with the experimental data (Kulkarni et al. 2010) within a 5 % error. This discrepancy is hypothesized to be due to the presumed idealized RUC with deterministic material properties.

The multiscale model could be extended to account for distribution in the crosslinking degree, fiber volume fraction, CNT height, and CNT areal density to quantify the uncertainty in the predicted transverse modulus. However, the present investigation's scope is limited to a parametric model assessment of the influence of such parameters on the output mechanical properties of interest. Additionally, the HFGMC theory predicts local strain profiles and damage contours, which could be beneficial to an improved understanding of the mechanisms that contribute to improving the composite transverse Young's modulus, strength, and toughness.

3.3.2 Sensitivity Analysis

This section presents the merits of the radially-grown architecture to the behavior of traditional CFRP composites. As a case study for microstructural analysis, the microscale unit cells with radially-grown CNT architecture with ~150 nm interphase thickness and traditional CFRP composite with no reinforced interphase are generated. The model is generated with a 2 % volume fraction of CNT (same as the one used for model validation). The two microscale constituent properties that govern the global behavior of a traditional CFRP composite, namely, polymer curing degree and microfiber volume fraction, are considered to investigate the variation in effective elastic properties. The effect of polymer crosslinking degree on the effective properties of radially-grown FFRP and CFRP composites is shown in Figure 11 (a)-(c). The nanoengineered interphase does not enhance the modulus in the longitudinal direction but shows a noticeable increase in properties transverse to the fiber. For a polymer crosslinking degree of 60%, 30% increase in transverse Young's modulus and up to 50% increase in transverse shear modulus is observed (see Fig 11 (b) - (c)). However, the effect of crosslinking degree on the

percentage enhancement in properties with and without the presence of a CNT-reinforced fiber-matrix interphase region is observed to be trivial.

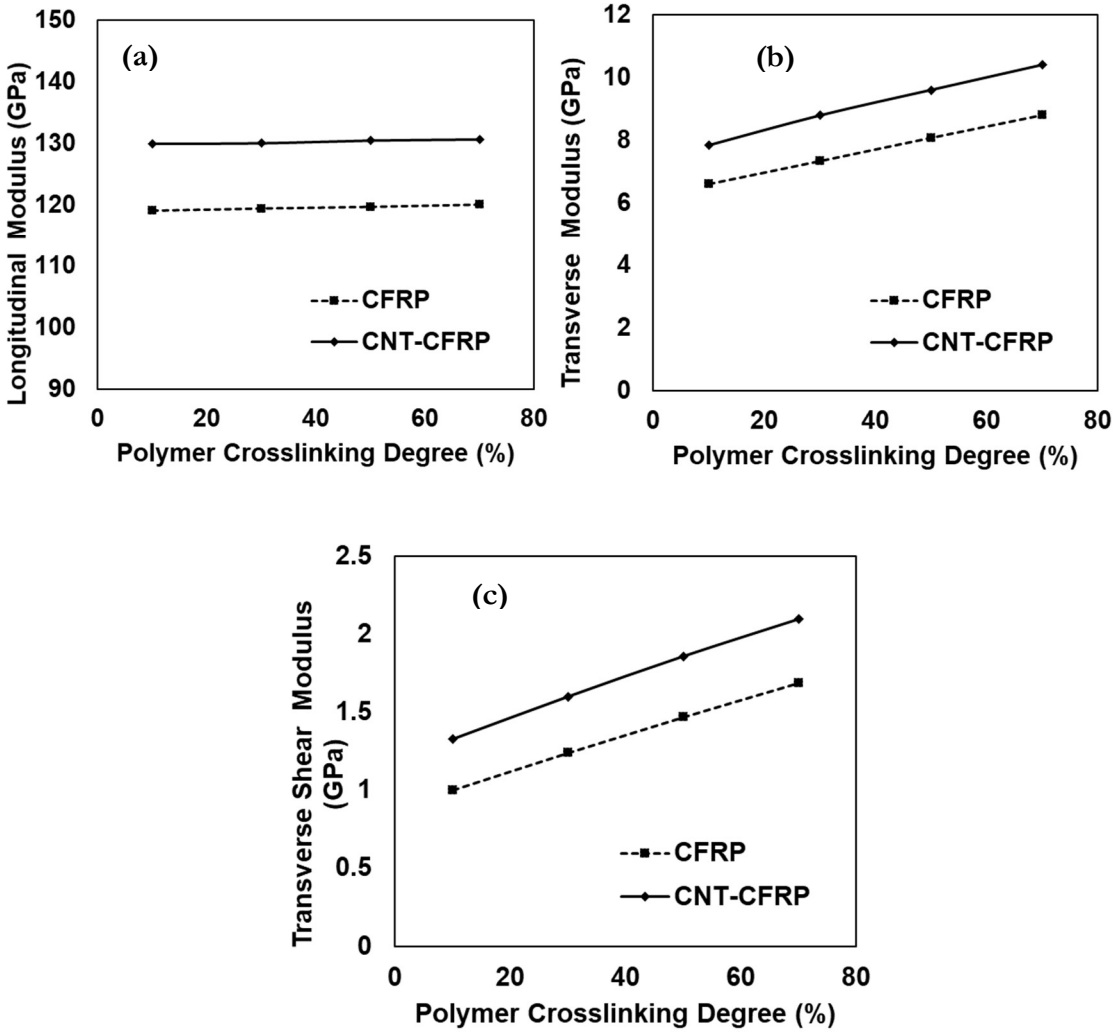

Figure 11. Comparison Between (a) Longitudinal; (b) Transverse; (c) Transverse Shear Modulus for Varying Crosslinking Degree.

Similarly, comparing effective properties between radially-grown CNT-CFRP and traditional CFRP with the varying carbon fiber volume fraction is shown in Figure 12 (a)-(c). The CNT-reinforced interphase did not change the longitudinal modulus. However, the

radially-grown CNTs on the fiber surface significantly improve the transverse elastic and shear modulus. For instance, at a 60 % fiber volume, the traditional CFRP and CNT-CFRP value correspond to a 27 % increment. Similarly, at a 60 % fiber volume fraction, the presence of radially-grown CNTs on the fiber surface increases the transverse shear modulus by 57 %. The transverse properties of the radially-grown CNT architecture relative to traditional CFRP are attributed to CNT-reinforced interphase subcells with enhanced stiffness in the CNT growth direction, aligned along the direction transverse to the fiber.

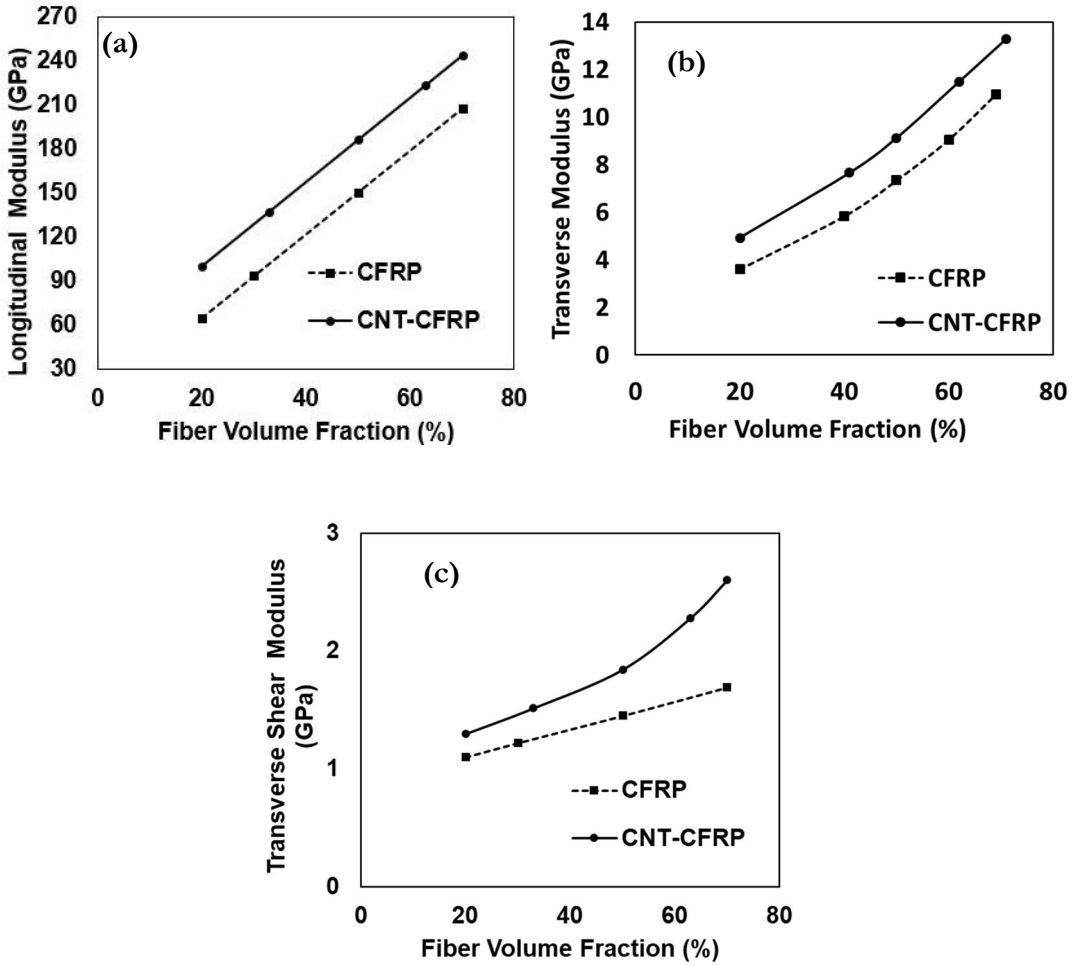

Figure 12. Comparison Between (a) Longitudinal; (b) Transverse; (c) Transverse Shear Modulus for Varying Fiber Volume %.

Two parametric analysis cases are considered to investigate the effect of the CNT-reinforced interphase region on the mechanical behavior of radially-grown CNT nanocomposite. In the first case, the effect of the length of the CNTs (eventually the thickness of the interphase region) on the nanocomposite's homogenized properties is investigated. The microscale unit cell is generated with a fiber diameter of 5 μm, 30% fiber volume fraction, and 20% polymer crosslinking degree. By varying the CNT height (virtually the interphase thickness) and assuming a constant CNT areal density of 100 CNTs/ μm^2, the parametric analysis is carried out for up to ~5 % volume fractions of CNT. The effect of interphase thickness on the transverse properties of radially-grown FFRP is shown in Figure 13 (a)-(b). Regarding the longitudinal properties, the increase in interphase thickness did not significantly change the properties. However, for 3 μm interphase thickness, the transverse Young's modulus and the shear modulus show improvement by 23% and 47%, respectively, compared to traditional FRP composite with no reinforced interphase region.

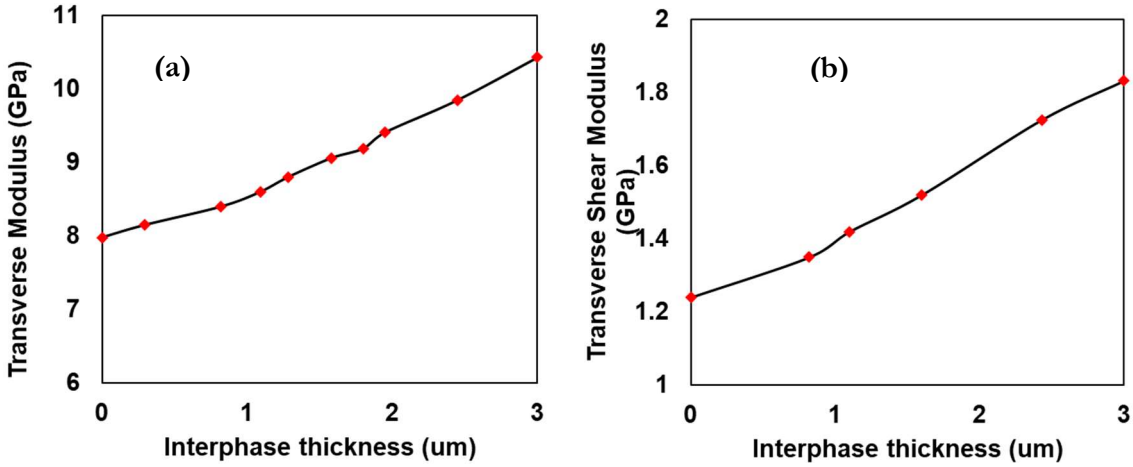

Figure 13. Effect of Interphase Thickness on (a) Transverse; (b) Transverse Shear Modulus

In the second case, the effect of CNT areal density on the effective properties of the nanocomposite is explored. The microscale unit cell is generated for the same fiber and matrix

properties. By varying the CNT areal density and assuming a constant interphase thickness of 150 nm is assumed, the parametric analysis is carried out for up to ~ 12 % volume fractions of CNT. Figure 14 (a)-(b) shows the effect of areal density on the transverse properties. The increase in areal density does not significantly enhance the transverse Young's modulus, showing a minor decrease in the transverse shear modulus. In general, the increase in CNT areal density or the CNT volume fraction in the interphase region is expected to enhance the elastic modulus primarily in the direction transverse to the fiber. The author hypothesizes that this disagreement is due to the variations in material properties in the interphase unit cell along the direction of CNT growth, which is not considered by the present modeling effort. Further investigation on the effect of areal density in the nanoscale unit cell along the growth direction is crucial to model the reinforcing effects at the micro length scale adequately.

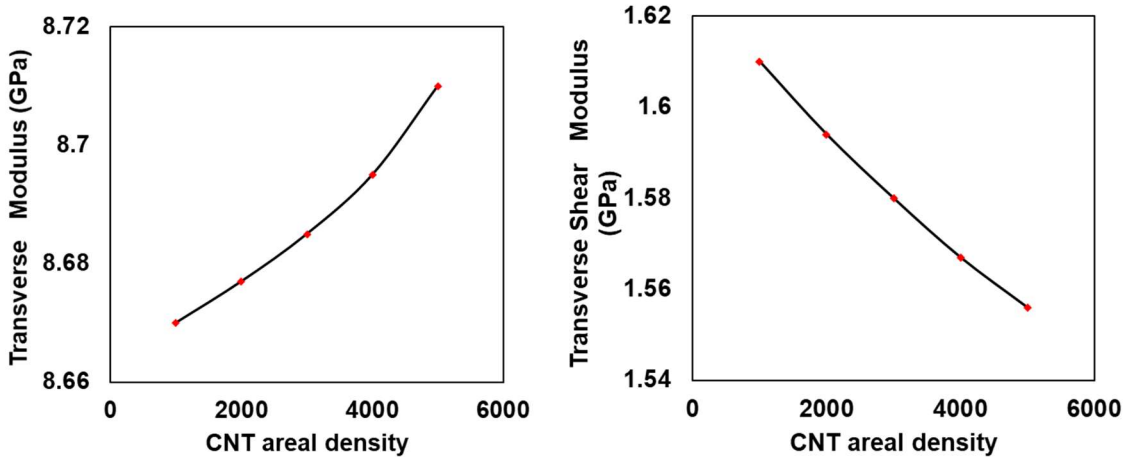

Figure 14. Effect of CNT Areal Density on (a) Transverse; (b) Transverse Shear Modulus

3.3.3 Damage Simulation under Out-of-plane Loading

The influence of matrix and CNT-reinforced interphase properties on the transverse nonlinear behavior is simulated to further assess strength and toughness enhancement capability. The microscale unit cell generated with a 30% volume fraction of fiber, 40% polymer crosslinking

degree, and 150 nm interphase thickness is used for this study. It is worth mentioning that the interphase rupture criterion for the atomistically-informed CDM model is set to 100 % to simulate a gradual softening response. This constituent level damage threshold value can be accurately estimated once the experimental data for strength and toughness becomes available.

The variation of transverse stress-strain response of radially-grown CNT-CFRP with two areal density cases is shown in Figure 15. The model does not show any significant variation in transverse Young's modulus. However, the increase in CNT areal density improves transverse tensile strength and strain to failure. At 3000 CNTs per μm^2, which corresponds to ~5 % volume fraction of CNT, the model predicts up to 25 % improvement in transverse tensile strength. This is attributed to the nanoscale phenomena, where the increase in areal density leads to improved damage saturation in the interphase region. The toughness or energy absorption capabilities determined by the area under the stress-strain curve improve with the increase in areal density. This enhancement is attributed to the pronounced nanoscale strain hardening tendencies due to the reorientation of CNTs along the loading direction. Furthermore, this enhancement could improve damage resistance in the out-of-plane direction and interlaminar strength in radially-grown CNT architecture. These observations are consistent with existing experimental investigations where the highly condensed deposition of radially-grown CNTs on fiber surface using a vapor deposition technique improved fracture energy by 45 % (Karapappas et al., 2009).

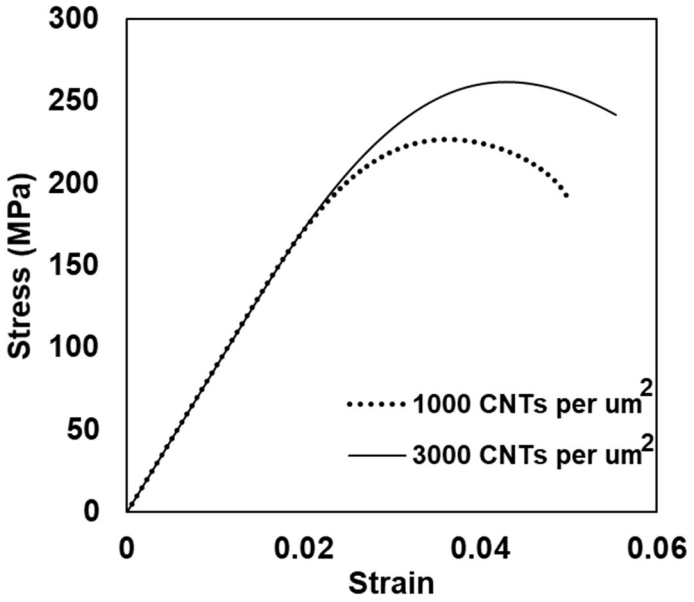

Figure 15. Predicted Transverse Failure Response for Different CNT Areal Density.

The variation of transverse stress-strain response of radially-grown CNT-CFRP with CNT-reinforced interphase thickness is shown in Figure 16. As shown before, the increase in interphase thickness enhances the transverse Young's modulus. In the inelastic regime, the increase in interphase thickness improves the transverse strength of the composite. At 2 μm interphase thickness and 100 CNTs per μm^2, which corresponds to ~ 3.2 % volume fraction of CNT, the model predicts a 20.4% improvement in transverse tensile strength compared to traditional FRP. The increase in interphase thickness (virtually CNT height) leads to an increased region of stiffness around the fiber, which improves the composite stiffness and strength. The interphase region also acts as a shielding transition layer, which reduces the stress concentrations in the surrounding matrix and delays the onset of damage. This phenomenon is further demonstrated in Sections 3.3.4 and 3.3.5.

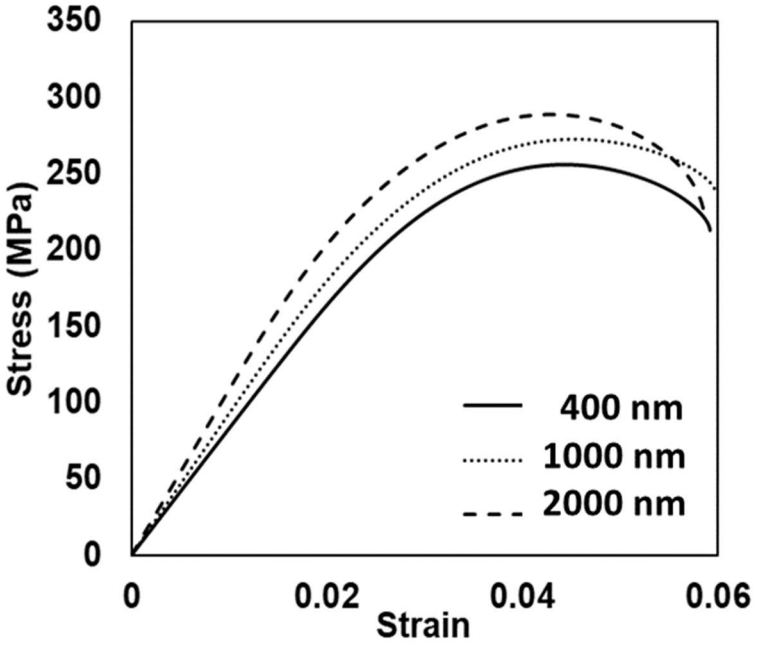

Figure 16. Predicted Transverse Failure Response for Varying Interphase Thickness.

Last, the microscale unit cell is generated for the same fiber properties and 150 nm CNT-reinforced interphase thickness. The variation of transverse stress-strain response of radially-grown CNT-CFRP for two cases of polymer crosslinking degree is shown in Figure 17. The nanocomposite exhibits more energy absorption capabilities at the lower crosslinking degree with a higher strain to failure. The increase in crosslinking degree causes increased load transfer characteristics but increased brittle response with a lower strain to failure. This variation is attributed to the nanoscale phenomena where bond breakage in neat epoxy becomes more brittle with an increase in crosslinking degree (Rai et al., 2017).

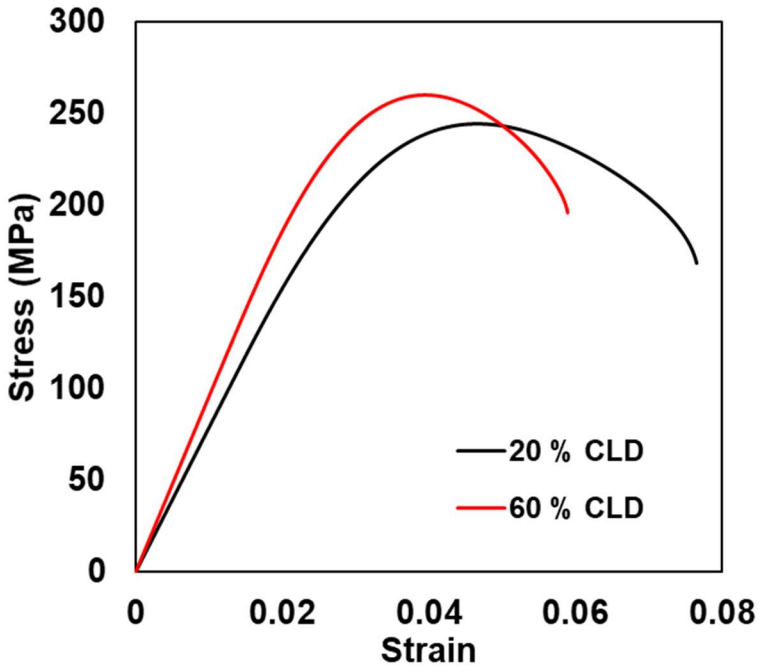

Figure 17. Predicted Transverse Failure Response for Varying Crosslinking Degree

3.3.4 Effect of Interphase on Inter-fiber Stresses

The HFGMC unit cell model is then analyzed in the elastic regime to investigate the effect of nanoengineered interphase on stresses expected to play a role in the onset of damage. While the debonding of CNT/epoxy is a nanoscale damage mechanism, the failure of epoxy close to stress concentration regions and the debonding of the fiber/matrix interface are primary failure modes expected to be seen at the microscale. The inter-fiber stress distribution, relevant to the fiber/matrix debond and matrix cracking, is studied to investigate this phenomenon. The microscale unit cell of 30 % fiber volume fraction with and without nanoengineered interphase subcells is subjected to boundary conditions mimicking deformation in the transverse direction. The model is generated with a 2 % volume fraction of CNT. A displacement in the y_2- direction corresponding to an average transverse strain of 0.3 %, which is well below the threshold strain for the constituent phases, is applied to the unit cell. Two stress components characterize the

stresses in the matrix region adjacent to the fiber interface; normal $\sigma_r(\theta)$ and tangential $\sigma_\tau(\theta)$, interfacial stresses. These stress components are calculated with respect to the cylindrical coordinates (r, θ, z) located at the fiber center. The fiber/matrix interfacial stresses are averaged over a thin region of matrix subcells around the fiber in the traditional FRP unit cell. In CNT-FRP, these stresses are in the matrix subcells around the interphase. The stress profile around the fiber/matrix interface in a quarter fiber unit cell of CFRP and radially-grown CNT-CFRP are presented in Figures 18 and 19. The stress distribution profile plotted between 90° and 180° for just one-quarter of the fiber.

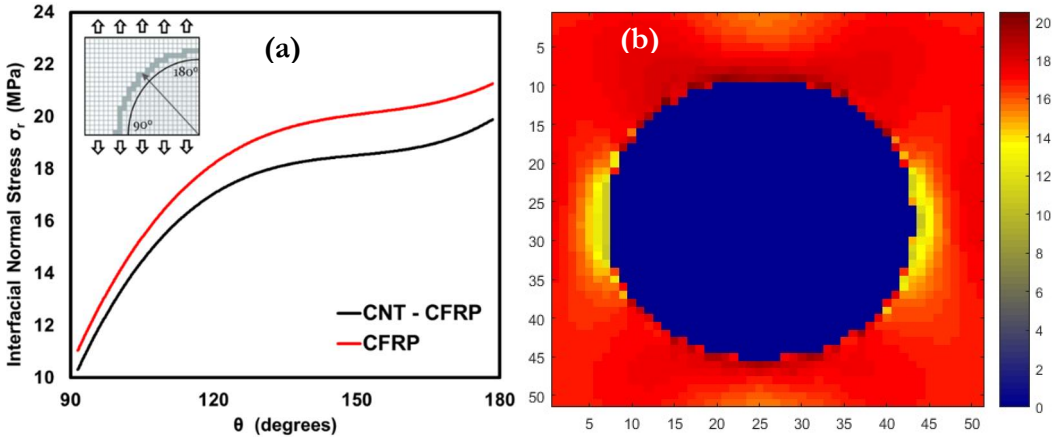

Figure 18. (a) Effect Of Interphase on Normal Interfacial Stresses $\sigma_r(\theta)$; (b) RUC Normal Interfacial Stress Contour

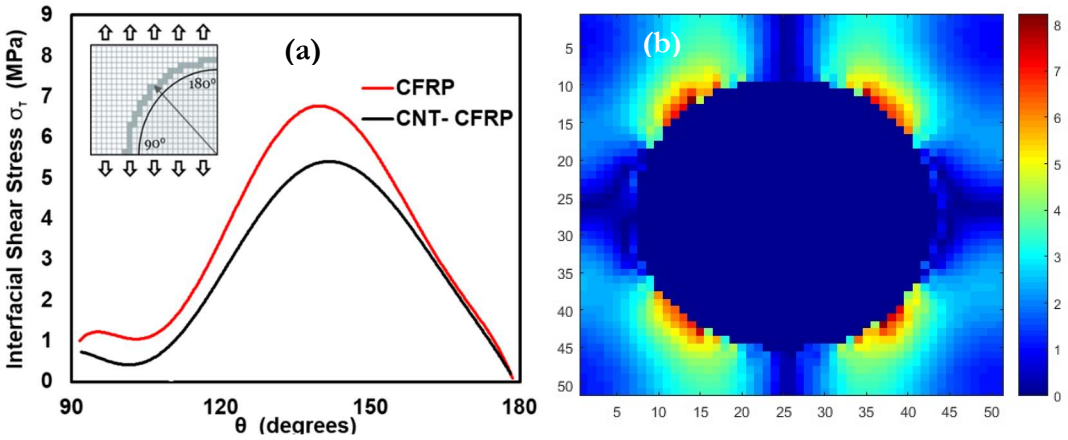

Figure 19. (a) Effect of Interphase on Tangential Interfacial Stresses $\sigma_\tau(\theta)$; (b) RUC Tangential Interfacial Stress Contour

In CFRP composites with no CNTs, the normal interfacial stresses $\sigma_r(\theta)$ gradually increases and reaches a maximum value at 180°Which is aligned with the transverse loading direction. The onset of debonding is expected to occur if the value of interface stress at 180° exceeds the interfacial strength. The normal interfacial stress in radially-grown CNT-CFRP shows a consistent trend of being lower with respect to CFRP (see Figure 18 (a)). Figure 18 (b) shows the contour plot of normal interfacial stresses in the matrix-rich subcells. The model shows a 20% reduction in the magnitude of normal stress at $\theta = 180^\circ$, compared to the model without CNTs. Figure 19 (b) shows the contour plot of tangential interfacial stresses in the matrix-rich subcells around the interphase region. The maximum peak is at around $\theta = 140^\circ$ and is around 60% lower than the normal stress peaks. As seen in Figure 19 (a), the magnitude of interfacial shear stress is also significantly reduced compared to the traditional FRP composite. The presence of nanoengineered interphase with orthotropic material properties suppresses the stress concentration in the matrix because of the mismatch in properties of the fiber and the matrix. Similar results and trends were reported by Romanov et al. (2015) and

Matveeva et al. (2019). Moreover, these predictions and observations are consistent with existing experimental investigations where radially-grown CNT on the fiber surface has better transverse and interfacial properties than traditional CFRPs (Carpenter et al., 2011; Wood et al. 2012).

3.3.5 Effect of Interphase on Damage Propagation

With a 2 % volume fraction of CNTs generated in Section 3.3.4, the microscale model is further used to investigate the effect of CNT-enhanced interphase on damage propagation. The unit cell is subject to deformation transverse to the fiber direction beyond the ultimate point. The developed multiscale model can predict the strength and toughness by accounting for the combined effect of the nanoscale and microscale damage mechanisms, namely, CNT/epoxy debonding, damage in the matrix, and fiber/matrix debonding. The multiscale model predictions of the transverse tensile stress-strain response of traditional CFRP and radially-grown CNT architecture are shown in Figure 20 (a). It is worth mentioning that CFRP's predicted transverse tensile strength is much larger than the experimental values. A rupture criterion can define the damage threshold for the polymer matrix at which global failure occurs. At the 2.5 % threshold value, the estimated transverse tensile strength of the CFRP was about 82 MPa, which correlates well with the experimental data (Gilat et al., 2002). However, as mentioned before, the microscale test data available for the radially-grown CNT architecture did not provide a comparable basis for refining the damage model for the CNT-reinforced fiber-matrix interphase region. Moreover, the scope of this investigation is to explore the progressive nature of damage that could be attributed to the enhancement in the composite fracture toughness and energy absorption capabilities. Therefore, the polymer and interphase damage model's rupture criteria are set to 100 % to simulate the complete softening response.

As shown in Figure 20 (a), the CNT-reinforced interphase increases the transverse tensile strength and energy absorption capabilities. Figure 20 (b) shows the damage states of radially-grown FFRP composite. It is observed that the damage regions are contained in a concentrated area around the circumference of the fiber corresponding to the initiation sites. Damage initiation occurs in the interphase and epoxy, while a significant of it is in the matrix around the interphase leading to potential debonding sites. The model initially shows substantial damage in polymer, which is accompanied by the degradation of interphase subcells. The interphase degradation implicitly accounts for the nanoscale bond breakage phenomena leading to CNT/epoxy debonding and following a dual softening behavior, which consumes more energy and further toughens the material. Finally, the failure of the interphase, along with matrix subcells, leads to complete fiber/matrix debonding. These observations indicate that epoxy damage is the primary toughening mechanism, while CNT/epoxy or fiber/epoxy debonding plays secondary roles. Nevertheless, all these mechanisms collectively contribute to the improvement in transverse strength and toughness properties.

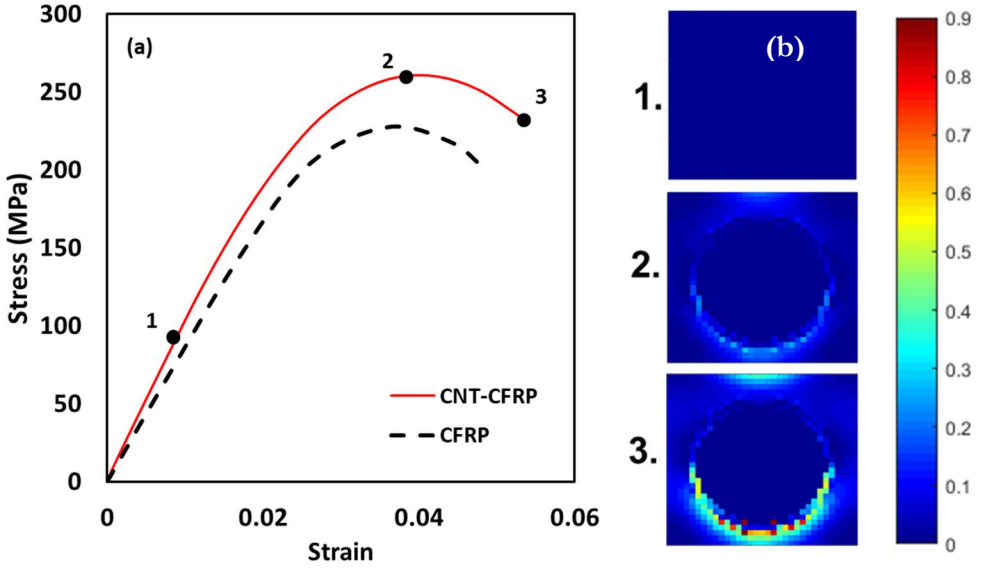

Figure 20. (a) Comparison of Transverse Failure Response with Traditional CFRP; (b) Local Subcell Damage Contour with Radially-Grown CNT

3.4 Summary

An atomistically-informed multiscale modeling framework was extended to evaluate the macroscopic properties of traditional fiber-reinforced polymer composites with radially-grown CNT architecture. The multiscale model accounts for physics-based constitutive laws and scale bridging mechanisms derived from molecular dynamics simulations. The constitutive models were integrated within a high-fidelity micromechanics framework. The transverse elastic modulus of radially-grown CNT-CFRP estimated by the high-fidelity micromechanical model was in good agreement with those predicted by the numerical and effective properties approach and the experimental data. Parametric studies were conducted to assess the capability to enhance stiffness, strength, and toughness of radially-grown CNT architecture by varying the matrix, reinforced fiber, and radially-grown CNT properties. The increase in CNT areal/growth density enhanced radially-grown CNT architecture's toughness and energy absorption capabilities. The increase in interphase thickness around the fiber (virtually the CNT height) showed notable improvements in transverse Young's modulus and transverse shear modulus.

The presence of radially-grown CNTs reduced the normal and shear interfacial stresses at the fiber/matrix interface. This reduction significantly affected the matrix-rich region's stresses that governed the onset of damage near the interphase region. The overall effect of radially-grown CNT on the damage resistance in the out-of-plane direction was investigated by comparing the stress-strain response with traditional FRP composites and investigating the microscale damage evolution. The damage originated in matrix-rich subcells around the CNT-

reinforced interphase region, accompanied by the degradation of interphase subcells to form debonding sites around the microfiber. The model also indicated the ability to predict the concurrent effects of the matrix and interphase damage mechanisms attributed to improved composite strength and toughness.

Based on the investigation presented in Sections 3.2 and 3.3, the CNT areal density has substantial effects on the improvement in strength; however, only marginal improvements were observed in stiffness at relatively high-volume fractions of CNT. The nanoscale-informed interphase continuum model and high-fidelity micromechanics theory can adequately capture the impact of radially-grown CNTs in the fiber/matrix interface. The methodology can be further integrated with finite element models of structural scale geometry to investigate the impact of radially-grown CNTs on critical properties such as interlaminar fracture toughness, interlaminar shear strength, and bearing strength. However, the HFGMC theory relies heavily on the description of microscale features and requires many internal variables, leading to high computational costs. Therefore, in the next chapter, a novel surrogate model is also developed to significantly replace full-field nonlinear HFGMC simulations and decrease the computational time and memory requirements of concurrent multiscale simulations.

CHAPTER 4

REDUCED ORDER MODEL FOR EFFICIENT MICROMECHANICS

4.1 Introduction

A significant limitation of the HFGMC micromechanics theory implemented in Chapter 3 is that incorporating a higher-order displacement field increases the number of unknowns per subcell, leading to a more extensive system of algebraic equations for the boundary value problem. Moreover, the accurate prediction of the effective composite behavior with inelastic subdomains relies heavily on the mesh discretization level necessary to resolve the subscale features and achieve numerical convergence. As a result, many internal variables are required, leading to high computational costs while limiting its use to multiscale analyses of small-scale coupons. Recently, computational reduced-order models (ROMs) built on full-field physics-based simulations have been developed to approximate global constitutive behavior with only a finite set of internal variables. These models are used at macroscopic integration points and can be evaluated many orders of magnitude faster than their full-field-based counterparts. A widely used model reduction technique is based on the proper orthogonal decomposition (POD), which is also known as principal component analysis (PCA) and singular value decomposition (SVD). Such methods mainly aim to reduce the high number of equations of full-field high-fidelity models such as FE methods through the projection of the entire equations on a sub-feature space. The POD-based ROM is often implemented in mechanics problems by creating a reduced basis from several snapshots of the full-field mechanical

response over the solution time. The optimally ordered set of basis functions are then used to solve the necessary boundary value problem in a reduced dimensionality space.

A ROM or surrogate model is then be formulated by truncating the optimal basis within a specific cut-off or threshold value. For multiscale analysis of composites, POD and its variants have been widely used for nonlinear heat conduction (Monteiro et al. 2008), multiscale fracture mechanics (Oliver et al. 2017), and damage analysis (Bhattacharyya et al. 2019, 2020). Another class of ROM technique is based on the hyper-reduction methods (Amsallem et al. 2015, Oliver et al. 2017), which approximate the integral by introducing a global basis to represent the integrand (nodal vector approximation) or by using a reduced set of integration points with empirically determined weights (integral quadrature approximation) (Farhat et al. 2015). Some examples of this class of ROM are the Discrete Empirical Interpolation Method (DEIM) (Chaturantabu and Sorensen 2010, Peherstorfer et al. 2014), Missing Point Estimation (MPE) method (Astrid et al. 2008), and Empirical Cubature Method (ECM) (Hernandez et al. 2017). Van Tuijl et al. (2018) present a comparison of the EIM and ECM for solving the microscale boundary value problem. Although the POD and hyper-reduction-based methods are widely used, they are better suited for linear or weakly nonlinear processes. This is because it heavily relies on a linear combination of only a few basis vectors. Besides, these models are known to drift from the highly nonlinear full-field simulations since the reduced basis is formulated based on the macroscopic response instead of microscopic quantities such as local displacement or inelastic strain fields. As a result, a significant challenge in these models is also to capture the nonlinear, path/history-dependent global material response while retaining relevant microscopic field quantitates.

A significant development in this direction is implementing transformation field analysis (TFA) theory (Dvorak and Benveniste 1992) to solve the microscale boundary value problem. In general, the internal deformation of each constituent phase in a composite results from internal stress fields arising from mechanical loads and thermal or other inelastic strains. If the deforming constituent phase is separated from the entire domain, it will deform freely without any contribution from any mechanical loads. However, the surrounding material restricts the deformation and generates internal strains, usually referred to as residual or transformation strain fields. The transformation fields are usually attributed to physically activated fields such as uncoupled thermal and phase transformations or inelastic strains that depend on the path or loading history. Coupled electromechanical deformation are also examples of transformation fields that depend on the evolution of other local electrical fields within the material domain. In the context of TFA theory, it is assumed that these transformation strain fields are represented by distributions that are piecewise uniform either in each phase or in the local volume V_r within these phases. Moreover, for small strain approximations, these fields are additively superimposed with the deformation induced by the uniform global strain fields. Therefore, the total local strain or stress field caused by the uniform global strain $\bar{\boldsymbol{\varepsilon}}$ or stress $\bar{\boldsymbol{\sigma}}$ and a piecewise uniform eigenstrain μ_s or eigenstress λ_s distribution is given as

$$\boldsymbol{\varepsilon}_r = \mathbb{A}_r : \bar{\boldsymbol{\varepsilon}} + \sum_{s=1}^{N} D_{rs}\mu_s \tag{4.1}$$

$$\boldsymbol{\sigma}_r = \mathbb{N}_r : \bar{\boldsymbol{\sigma}} + \textstyle\sum_{s=1}^{N} F_{rs}\lambda_s, (r, s = 1, \ldots . N) \tag{4.2}$$

The D_{rr} and D_{rs} are the self-induced and transmitted eigenstrain influence functions, F_{rr} and F_{rs} are the corresponding eigenstress influence functions. $\mathbb{A}_r$ and $\mathbb{N}_r$ are the mechanical strain and stress concentration tensors. The TFA formulation allows precomputing these

influence functions and concentration tensors in the preprocessing phase, allowing for the nonlinear analysis to be carried out with only a smaller number of unknowns. However, the assumption of piecewise uniform inelastic strain fields often requires a subdivision of each constituent phase into several sub-domains to predict the effective composite behavior with reasonable accuracy (Dvorak et al. 1994, Oskay and Fish 2007). Subsequently, the nonuniform transformation field analysis (NTFA) theory was developed by Michel and Suquet (2003), where the microscopic plastic or inelastic strain fields are no longer assumed to be piecewise uniform. The NTFA overcomes the drawbacks of TFA by defining the inelastic or plastic strain fields within each phase using a set of tensorial modes and subsequently capturing large deviations from uniformity. The choice of inelastic modes can be confined to each constituent phase or over the entire microscale domain. Notably, the NTFA method also incorporates microstructural information into the ROM, which is a crucial difference from other techniques such as the (a priori) hyper-reduction method (Ryckelynck 2005), the proper generalized decomposition method (Relun et al. 2013), or the general (Galerkin) projection-based ROMs (Robens-Radermacher et al. 2018). It provides localization rules to reconstruct local field quantities using precomputed operators and influence functions.

Most work on NTFA based ROMs focuses on simplifying the theory with various microscopic constituent models. Roussette et al. (2009) first extended the theory to composites with viscoplasticity and used POD to identify plastic modes. Michel and Suquet (2010) showed an improved efficiency-to-accuracy ratio by implementing the two-dimensional implementation method into the fast Fourier transform (FFT) theory. Additionally, they extended this formulation to account for cyclic loading conditions. Fritzen (2010) and (2013) later provided a 3D implementation of the theory using FE methods while extending it to viscoelastic composites composed of a matrix containing elastic inclusions. Largenton et al.

2014 further expanded the method to account for more viscoelastic phases in the presence of aging and swelling. To date, very few literature contributions have been made to the study of micro constituent level damage using the NTFA theory. Recently, Ju and Mahnken 2016, provided an FE implementation of the NTFA to consider softening effects due to combined plasticity and damage through an alternate formulation of the yield function where the damage state variable degraded the yield stress. However, in their case, the conventional NTFA approximation did not provide enough accuracy and failed to capture a highly nonlinear effective response. Instead, an adaptive NTFA model was proposed, which allowed for switching back to full-field FE simulations in regions within the RUC beyond a critical state of damage to improve the overall prediction accuracy. The computational costs increased using this approach, and it could not be applied to constitutive equations with damage state variables acting on the elastic modulus or the effective stress field.

In this chapter, a novel adaptation of the NTFA in conjunction with the HFGMC theory is presented to consider softening effects caused by damage. The distinctive feature of this work is that continuum damage state effects are considered as damage-induced inelastic strains acting on the individual material phase. For this purpose, the strain equivalence principle replaces the nominal stress with the effective stress in the damaged configuration. These assumptions allow for applying the superposition principle in the NTFA theory and solving the eigenstress or strain field in one phase based on the damage-induced inelastic strain field in another phase. A three-phase nanocomposite with an isotropic polymer matrix, transversely isotropic fibers, and orthotropic fiber-matrix interphase is used to demonstrate the predictive capability of the developed ROM. The reduced constitutive model of the inelastic phase has evolution equations and yield functions based on their microscopic counterparts.

The present chapter is organized as follows. Section 4.2 presents the HFGMC governing equations and constitutive model required to simulate the homogenized behavior of the composite subject to damage-induced inelastic strains. In Section 4.3, the NTFA procedure is extended to account for the damage softening effects by approximating the inelastic strain field. Section 4.4 presents the numerical implementation of the NTFA using HFGMC to compute inelastic modes and to localize operators for the ROM. Two types of inelastic mode identification procedures are discussed, with the algorithms presented in detail. In Section 4.5, the accuracy and efficiency of the developed ROM are assessed by comparing the global and local field quantities for different loading paths with full-field HFGMC simulations.

Notation: All quantities on the macroscale are symbolized using overlined letters such as $\bar{A}$ while quantities on the microscale are not overlined. Boldface lower-case Greek letters are reserved for second-order tensors (e.g., $\boldsymbol{\epsilon}, \boldsymbol{\sigma}, \boldsymbol{\eta}$). Regular lower-case Greek with a capped letter such as $\hat{\xi}$ denotes spatial or temporal vectors. Fourth-order tensors are denoted using letter-like symbols $\mathbb{C}, \mathbb{R}, \mathbb{N}$ and alike. Other matrices are defined using letter-like scripts $\mathcal{A}, \mathcal{D}, \mathcal{K}$ and alike. The individual components of the vectors, tensors, and matrices are denoted using regular letters with subscript indices (e.g., $\xi_i, \mathcal{A}_{ij}$). The L^2 norm of a tensor or a vector is symbolized by $\|A\|_2$. Additionally, the volume averaging operator of a quantity ■ in the domain r is defined as

$$\langle \blacksquare \rangle_r = \frac{1}{|\Theta_r|} \sum_{\beta=1}^{N(r)} \left|\Theta^{(\beta)}\right| \ \blacksquare \tag{4.3}$$

where $|\Theta_r|$ denotes the total volume of the phase r, $\left|\Theta^{(\beta)}\right|$ denotes the subcell or sub element (β) volume, and $N(r)$ denotes the total number of subcells belonging to phase r. If r is neglected, the operator averages the quantity over the entire RUC/RVE domain Ω.

4.2 Problem Statement and Governing Equations

The fiber-reinforced polymer composites with radially grown CNTs on fiber presented in the previous chapter will illustrate the ROM developed in this chapter. It contains three distinct phases: radially grown CNTs, microfiber inclusions, and polymer matrix. No experimental data are available for the nonlinear mechanical response of a unidirectional (UD) FFRP composite under complex multiaxial loading. Therefore, reference results for the mechanical response of these three-phase nanocomposites must be generated using full-field simulations.

In the previous chapter, the nonlinear behavior of the FFRP composite was simulated using an idealized microscale RUC containing three distinct phases. CNTs in the fiber-matrix transition region result in a complex stress state, creating an additional layer of stiffness around the fiber at the microscale. Consequently, the CNT-enhanced interphase region was represented using a homogenous continuum medium with thickness representing the height of radially grown CNTs. The FFRP composite RUC is shown in Figure 21. The microfiber phase is modeled as linear elastic transversely isotropic, while the polymer matrix phase is isotropic. The explicit interphase region is modeled with linear elastic orthotropic properties. The damage initiation of the matrix is modeled using CDM with an evolution equation developed to capture the polymer mechanics arising from covalent bond breakage at the nano length scale. The damage state variable is atomistically informed and initially developed using a nonlinear response from MD simulations of epoxy resin and hardener molecules. More details on the MD simulations and constitutive model development can be found in Rai et al. 2017. The composite RUC is simulated using the HFGMC micromechanics approach. As mentioned in the previous chapter, the HFGMC approach can capture the normal-shear

coupling effects in the composite and the load transfer characteristics between individual phases. A brief account of the necessary governing equations and the nonlinear constitutive equations for the polymer matrix is given in the following subsections.

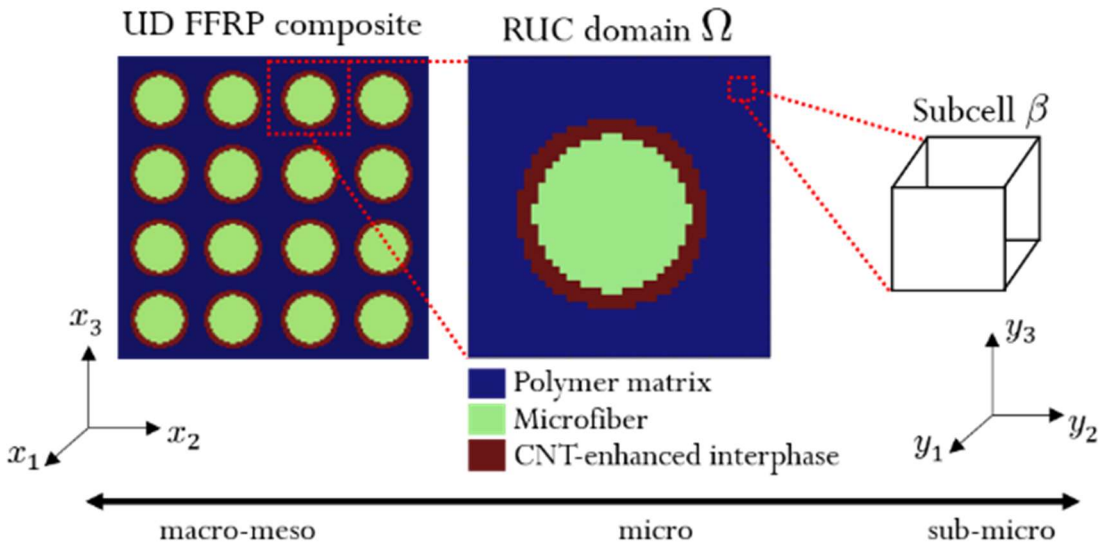

Figure 21. Multiscale Homogenization Scheme Using HFGMC Approach

4.2.1 Damage-induced Inelastic Strain Formulation

The UD FFRP composite is defined using a triply periodic RUC discretized into N number of subcells. The RUC is defined in the $x_1 - x_2 - x_3$ plane with microfiber inclusion and extended infinitely in the $x_1 -$ direction. Each subcell (β) is defined in the local $y_1 - y_2 - y_3$ coordinate system, with d, h, l as the subcell dimensions. The local subcell displacement field is given as

$$u_i{}^{(\beta)} = \bar{\epsilon}_{ij}x_j + W_{i(000)}{}^{(\beta)} + y_1 W_{i(100)}{}^{(\beta)} + \frac{1}{2}\left(3y_1^2 - \frac{d^2}{4}\right) W_{i(200)}{}^{(\beta)} \tag{4.4}$$

$$+\ y_2 W_{i(010)}{}^{(\beta)} + \frac{1}{2}\left(3y_2^2 - \frac{h^2}{4}\right) W_{i(020)}{}^{(\beta)} +\ y_3 W_{i(001)}{}^{(\beta)}$$

$$+ \frac{1}{2}\left(3y_3^2 - \frac{l^2}{4}\right) W_{i(002)}{}^{(\beta)}$$

where $W_{i(lmn)}{}^{(\beta)}$ are the unknown displacement micro variables and $\bar{\epsilon}$ is the average remote strain field. For small deformation problems, the subcell strain field $\boldsymbol{\varepsilon}^{(\beta)}$ is obtained as

$$\boldsymbol{\varepsilon}^{(\beta)}(t) = \bar{\epsilon}(t) + u^{(\beta)}_{(i,y_j)}(t) \tag{4.5}$$

where $\boldsymbol{u}^{(\beta)}_{(i,y_j)}$ comprises the fluctuating displacement micro variables. Each subcell in the RUC is assigned material properties and constitutive equations to describe the sub-micro scale material behavior. Using the strain equivalence principle and assuming that the damage state in each direction evolves independently, the generalized 3D Hook's law for linear elastic materials can be defined as

$$\boldsymbol{\sigma}^{(\beta)}(t) = \left(\mathbb{I} - \mathbb{D}^{(\beta)}(t)\right) : \mathbb{C}^{(\beta)} : \boldsymbol{\varepsilon}^{(\beta)}(t) \tag{4.6}$$

where $\boldsymbol{\sigma}^{(\beta)}$, $\mathbb{C}^{(\beta)}$, $\mathbb{I}$ are the microscopic subcell stress field, fourth-order elastic stiffness tensor, and fourth-order identity tensor, respectively. $\mathbb{D}^{(\beta)}$ is a fourth-order damage tensor with diagonal components comprising six independent damage variables $(\omega_1^{(\beta)}, \omega_2^{(\beta)}, \ldots \omega_6^{(\beta)})$ and non-diagonal components as zero. The above expression can be rewritten as

$$\boldsymbol{\sigma}^{(\beta)}(t) = \mathbb{C}^{(\beta)} : \left(\boldsymbol{\varepsilon}^{(\beta)}(t) - \boldsymbol{\varepsilon}_D^{(\beta)}(t)\right) \tag{4.7}$$

$$\boldsymbol{\varepsilon}_D^{(\beta)}(t) = \mathbb{D}^{(\beta)}(t) : \boldsymbol{\varepsilon}^{(\beta)}(t) \tag{4.8}$$

where $\boldsymbol{\varepsilon}_D^{(\beta)}$ is the subcell damage-induced inelastic strain field. The damage state formulated in terms of this inelastic strain field allows applying the superposition principle and approximation in the NTFA theory, as discussed in Section 4.3. The global RUC stress field is defined by volume averaging Eq. (4.7) over the entire domain Ω:

$$\bar{\boldsymbol{\sigma}}(t) = \langle \boldsymbol{\sigma}^{(\beta)}(t) \rangle \tag{4.9}$$

The microscopic stress field in Eq. (4.7) can be directly used to determine subcell surface-averaged traction force vector $t^{(\beta)}$. In the reformulated HFGMC (Balasu et al. 2020), the overall computational efficiency is significantly improved by deriving $t^{(\beta)}$ as a function of surface-averaged fluctuating displacement components. The surface-averaged traction is given as

$$t^{(\beta)} = [\mathcal{K}]^{(\beta)} \cdot \hat{u}^{(\beta)} + [\mathcal{C}]^{(\beta)} \cdot \left(\bar{\epsilon} - \boldsymbol{\varepsilon}_D^{(\beta)}\right) \tag{4.10}$$

where $[\mathcal{K}]^{(\beta)}$ is the subcell stiffness matrix, $[\mathcal{C}]^{(\beta)}$ is a subcell system matrix containing the elastic properties and $\hat{u}^{(\beta)}$ is the surface-averaged subcell displacement vector. The components of these system matrices can be found in Balasu et al. 2020. By imposing traction continuity conditions between adjacent subcells and periodic boundary conditions on the exterior boundaries, the global system of linear algebraic equations can be formulated as

$$\overline{\mathcal{K}} \cdot \hat{\bar{u}} = \hat{f}\,(\bar{\epsilon}) + \hat{g}(\boldsymbol{\varepsilon}_D) \tag{4.11}$$

where $\overline{\mathcal{K}}$ is the global RUC stiffness matrix, the vector $\hat{\bar{u}}$ represents the unknown surface-averaged displacements, vector $\hat{f}$ represents the external force due to the average remote strain field, and $\hat{g}$ contains the traction forces due to the microscopic damage-induced inelastic strain field $\boldsymbol{\varepsilon}_D^{(\beta)}$ that is implicitly dependent on the solution vector $\hat{\bar{u}}$. Equation (4.11) is analogous to the FE method, realized by defining the global stiffness matrix, applied external forces, and

internal resisting forces. However, unlike conventional nonlinear FE methods, $\overline{\mathcal{K}}$ does not change iteratively since the nonlinear contributions due to subcell constituent damage are accounted for in the vector $\hat{g}$. The global system of equations is solved twice per iteration per increment: first, solve the RUC boundary value problem without inelastic fields; next, update the inelastic field quantities using an iterative integration scheme. The solution vector $\hat{\bar{u}}$ is then used to determine the microscopic subcell strain and stress field defined in Eq. (4.5) and (4.7). It must be noted that most of the computational cost incurred is due to the factorization of the $9N * 9N$ global stiffness matrix and the number of iterations it takes to achieve a converged solution at every inelastic load increment. Therefore, order reduction is a beneficial option for improving the computational efficiency associated with the repeated solution of the HFGMC global system of algebraic equations.

4.2.2 Constituent Equations

The atomistically informed CDM model for polymer matrix will illustrate the NTFA-based ROM adaptation for nonlinearity due to damage. Using the strain equivalence principle, the microscopic, elastic-free energy term with isotropic damage can be written as

$$\psi_e = \frac{1}{2\rho}\big(1-\omega(t)\big)\cdot\boldsymbol{\sigma}(t):\boldsymbol{\varepsilon}^{\boldsymbol{e}}(t) \tag{4.12}$$

where $\boldsymbol{\rho}$ is the material density, $\boldsymbol{\sigma}$ is the effective stress field, $\boldsymbol{\varepsilon}$ is the elastic strain field, and $\boldsymbol{\omega}$ is the isotropic continuum damage variable. As in Eq. (4.7), the above expression can be rewritten in terms of the damage-induced inelastic strain $\boldsymbol{\varepsilon}_{\boldsymbol{D}}$ as follows.

$$\psi_e = \frac{1}{2\rho}\boldsymbol{\sigma}:\big(\boldsymbol{\varepsilon}(t)-\boldsymbol{\varepsilon}_{\boldsymbol{D}}(t)\big) \tag{4.13}$$

$$\boldsymbol{\varepsilon}_{\boldsymbol{D}}(t) = \omega(t)\cdot\boldsymbol{\varepsilon}^{\boldsymbol{e}}(t) \tag{4.14}$$

In the absence of plastic strains, the elastic strain $\boldsymbol{\varepsilon^e}$ is equal to the total strain determined using Eq. (4.5). Consequently, Cauchy's nominal stress field can be defined as

$$\boldsymbol{\sigma} = \rho \frac{\delta \psi}{\delta \boldsymbol{\varepsilon}} = \big(1 - \omega(t)\big) \cdot \boldsymbol{\sigma}(t) \tag{4.15}$$

The thermodynamic conjugate force associated with damage ω can be defined from the free energy term as

$$Y = -\rho \frac{\delta \psi}{\delta \omega} = \frac{1}{2}\, \boldsymbol{\sigma}(t) : \boldsymbol{\varepsilon}(t) \tag{4.16}$$

The classical Lemaitre yield function is given by

$$\phi = \frac{\sqrt{\frac{3}{2}} \|\boldsymbol{\sigma}\|_2}{1 - \omega(t)} - \sigma_y \tag{4.17}$$

where σ_y is the material yield strength. The damage evolution in the polymer matrix simulates the nanoscale covalent bond breakage process and is expressed as

$$\begin{gathered} \dot{\omega} = \frac{\dot{\lambda}}{2}\left[\operatorname{sgn}(x) \frac{-(1-\theta)|x| - |x|}{2(1-\theta)|x| + (1-\theta) - 1} + 1\right] \\ x = 2\left(\frac{Y}{Y_0}\right)^{\frac{1}{2(1-\theta)}} - 1 \end{gathered} \tag{4.18}$$

where θ is the polymer crosslinking degree and Y_0 is the minimum elastic energy required to initiate damage. The elastic modulus of the polymer matrix is a function of the crosslinking degree (Rai et al. 2017) The model predicts more ductile post-yield behavior at lower crosslinking degrees than at higher crosslinking degrees. The above expression follows a sigmoidal evolution curve with initial exponential growth followed by a linear phase and damage saturation. The evolution of the damage state variable is coupled to the viscoplastic multiplier $\dot{\lambda}$ obtained using the Peric formulations and is given as

$$\dot{\lambda} = \frac{1}{G}\left[\left(\frac{\phi + \sigma_y}{\sigma_y}\right) - 1\right]^{1/n} \tag{4.19}$$

where G and n are the viscoplastic constants. It is worth mentioning that the above constitutive equations are a simplified version of the model proposed by Rai et al. (2017). The original model accounts for both damage and plasticity effects.

Note that the damage evolution law presented in Eq. (4.18) does not account for a characteristic element size or fracture energy parameter. As a result, theoretically, incorporating this model within the HFGMC framework can result in strain localization and spurious mesh sensitivity of the softening behavior. While mesh objectivity is crucial, the proposed CDM model merely demonstrates the application of the NTFA theory to derive a reduced-order macroscopic CDM formulation that requires fewer internal variables and is evaluated only once at each time step. In addition, the developed ROM is expected to inherently preserve mesh dependency since the localization operators and inelastic modes are computed based on the data generated using full-field HFGMC simulations for a given discretization of the microstructure. In the future, a suitable regularization method can be introduced into the constituent damage model to circumvent the mesh-dependency of full-field simulations and the corresponding NTFA-based ROM predictions

4.3 NTFA-based ROM

The NTFA formulations available in the literature include a constitutive plasticity model with isotropic/kinematic hardening effects. Ju and Mahnken 2016 provide the formulation to account for softening effects due to combined plasticity and damage. In a typical CDM model, the damage state variable is a function of the damage conjugate force, defined in Eq. (4.16), and it is used to degrade the elastic modulus or the effective stress field. Ju and Mahnken 2016

coupled the evolution of the damage evolution to an equivalent plastic strain field and degraded only the yield stress in the yield function. This formulation allowed applying the NTFA superposition principle on a unified inelastic strain field that implicitly accounts for both plasticity and damage. However, the conventional NTFA approximation did not provide adequate accuracy and failed to capture the RUC's nonlinear response and highly heterogeneous local stress fields.

This section proposes a new NTFA formulation where the continuum damage state variable is formulated as a damage-induced inelastic strain field. This assumption allows for applying the superposition principle in the NTFA theory and solving the transformation strain or eigenstress fields in each constituent phase. This assumption also allows for approximating inelastic strain fields into a set of modes that will serve as shape functions explicitly pertinent to the plastic and damage-induced inelastic strains. The NTFA-based ROM adaptation to account for the combined damage-induced inelastic strain, together with plasticity and hardening effects, will remain an aspect of our future work. The present study focuses on introducing the formulation accounting for the damage-induced inelastic strain field only. The NTFA localization rules and the reduced constitutive equations for an arbitrary inelastic phase r are derived as follows. The space-time dependency of the damage-induced inelastic strain field $\boldsymbol{\varepsilon}_D^{(\beta)}$ is approximated into a finite set of deformation modes given by

$$\boldsymbol{\varepsilon}_D^{(\beta)}(t) = \sum_{k=1}^{M(r)} \boldsymbol{\mu}_k^{(\beta)} \xi_k(t) \tag{4.20}$$

where $M(r)$ denotes the total number of modes in phase r, $\xi_k(t)$ is the time-dependent damage mode activity coefficient, $\boldsymbol{\mu}_k^{(\beta)}$ is the heterogenous tensorial inelastic mode. Unlike TFA, the introduction of spatial heterogeneity in the inelastic strains allows for a more accurate

representation of the nonlinear deformation processes. The critical elements of the NTFA model are: (i) identification of the damage-induced inelastic modes and (ii) determination of the evolution of damage mode activity coefficients $\xi_k(t)$. A small number of inelastic modes are constructed to form a suitable basis for Eq. (4.20). The mode identification procedure and the algorithm are presented in Section 4.4.2.

Once the modes are identified, using the approximation of inelastic strains in Eq. (4.20), the superposition principle of the NTFA theory leads to the following localization rule for the microscopic subcell strain field:

$$\boldsymbol{\varepsilon}^{(\beta)}(t) = \mathbb{A}^{(\beta)}\colon\bar{\boldsymbol{\varepsilon}}(t) + \sum_{k=1}^{M(r)} \boldsymbol{\eta}_k^{(\beta)}\xi_k(t) \tag{4.21}$$

where $\boldsymbol{\eta}_k^{(\beta)}$ denotes the eigenstrain tensor. The fourth-order tensor $\mathbb{A}^{(\beta)}$ denotes the subcell mechanical strain concentration operator, determined by performing six independent elastic strain path computations for the HFGMC boundary volume problem outlined in Section 4.4.1. The eigenstrain tensor is computed by solving $M(r)$ linear elastic eigenstress problems (see Section 4.4.1 for more details). Combining Eq. (4.20) and (4.21) with Eq. (4.7), the localization rule for the subcell stress field is given by

$$\boldsymbol{\sigma}^{(\beta)}(t) = \mathbb{C}^{(\beta)}\colon\mathbb{A}^{(\beta)}\colon\bar{\boldsymbol{\varepsilon}}(t) + \sum_{k=1}^{M(r)} \boldsymbol{\rho}_k^{(\beta)}\xi_k(t) \tag{4.22}$$

where $\boldsymbol{\rho}_k^{(\beta)} = \mathbb{C}^{(\beta)}\colon\left\{\boldsymbol{\eta}_k^{(\beta)} - \boldsymbol{\mu}_k^{(\beta)}\right\}$ is the eigenstress tensor.

To prescribe the evolution of the damage mode activity coefficient ξ_k, further assumptions are required to derive reduced macroscopic constitutive equations and yield functions associated with the inelastic modes. First, the macroscopic free energy density per unit volume

of the heterogeneous material is formulated by volume averaging the microscopic free energy term in Eq. (4.13) as

$$\bar{w}(\bar{\boldsymbol{\varepsilon}}, \hat{\xi}) = \langle \rho \psi_e(\boldsymbol{\varepsilon}^{(\beta)}, \boldsymbol{\varepsilon}_D^{(\beta)}) \rangle \tag{4.23}$$

The average macroscopic strain $\bar{\boldsymbol{\varepsilon}}$ and the mode activity coefficient vector $\hat{\xi}$ are the new variables at the macroscopic material point. Then, the thermodynamic conjugate driving force with respect to the k-th mode activity coefficient of phase r is defined as

$$\begin{aligned} \tau_k{}^{(r)} &= -\frac{\delta \bar{w}}{\delta \xi_k} = -\langle \rho \frac{\delta \psi_e}{\delta \xi_k} \rangle = -\langle \rho \left(\frac{\delta \psi_e}{\delta \boldsymbol{\varepsilon}^{(\beta)}} : \boldsymbol{\eta}_k^{(\beta)} + \frac{\delta \psi_e}{\delta \boldsymbol{\varepsilon}_D^{(\beta)}} : \boldsymbol{\mu}_k^{(\beta)} \right) \rangle \\ &= \frac{1}{2} \langle \boldsymbol{\sigma}^{(\beta)} : \boldsymbol{\mu}_k^{(\beta)} \rangle - \langle \boldsymbol{\sigma}^{(\beta)} : \boldsymbol{\eta}_k^{(\beta)} \rangle \end{aligned} \tag{4.24}$$

Following the work of Fritzen and Bohlke (2013), in Eq, (4.24), the term $\langle \boldsymbol{\sigma}^{(\beta)} : \boldsymbol{\eta}_k^{(\beta)} \rangle = 0$ since $\langle \boldsymbol{\eta}_k^{(\beta)} \rangle = 0$ and due to static admissibility of the local stress field $\boldsymbol{\sigma}^{(\beta)}$ and eigenstress tensor $\boldsymbol{\rho}_k^{(\beta)}$. Therefore, by combining Eq (4.24) with Eq. (4.22), the simplified expression for the thermodynamic conjugate force is given as

$$\tau_k{}^{(r)} = \frac{1}{2} \left\langle \mathbb{A}^{(\beta)^T} : \mathbb{C}^{(\beta)} : \boldsymbol{\mu}_k^{(\beta)} \right\rangle : \bar{\boldsymbol{\varepsilon}}(t) + \frac{1}{2} \sum_{l=1}^{M(r)} \xi_k(t) \left\langle \boldsymbol{\mu}_k^{(\beta)} : \boldsymbol{\rho}_l^{(\beta)} \right\rangle \tag{4.25}$$

The orthonormal basis is given by

$$\begin{aligned} \boldsymbol{B}^{(1)} = \boldsymbol{e}_1 \otimes \boldsymbol{e}_1, \boldsymbol{B}^{(2)} = \boldsymbol{e}_2 \otimes \boldsymbol{e}_2 \\ \boldsymbol{B}^{(3)} = \boldsymbol{e}_3 \otimes \boldsymbol{e}_3, \boldsymbol{B}^{(4)} = sym(\boldsymbol{e}_2 \otimes \boldsymbol{e}_3) \\ \boldsymbol{B}^{(5)} = sym(\boldsymbol{e}_1 \otimes \boldsymbol{e}_3), \boldsymbol{B}^{(6)} = sym(\boldsymbol{e}_1 \otimes \boldsymbol{e}_2) \end{aligned} \tag{4.26}$$

Consequently, Eq. (4.25) can be expressed in a convenient matrix-vector form as follows.

$$\hat{\tau}^{(r)} = \mathcal{A} \cdot \bar{\varepsilon}(t) + \mathcal{L} \cdot \hat{\xi}(t) \tag{4.27}$$

$$\bar{\varepsilon}_i = \bar{\varepsilon} : \boldsymbol{B}^{(i)} \, , (i = 1, \dots ,6)$$

$$\mathcal{A}_{ki} = \frac{1}{2}\left\langle \mathbb{A}^{(\beta)^T} : \mathbb{C}^{(\beta)} : \boldsymbol{\mu}_k^{(\beta)} \right\rangle : \boldsymbol{B}^{(i)} \, , (i = 1, \dots ,6; \; k = 1, \dots , M)$$

$$\mathcal{L}_{kl} = \frac{1}{2}\left\langle \boldsymbol{\mu}_k^{(\beta)} : \boldsymbol{\rho}_l^{(\beta)} \right\rangle \, , (k, l = 1, \dots , M)$$

In the above expression, the thermodynamic conjugate forces and the corresponding damage mode activity coefficients are denoted in vector form $\hat{\tau} = \left[\hat{\tau}_1 \dots \hat{\tau}_k \dots \hat{\tau}_{M(r)}\right]^T$ and $\hat{\xi} = \left[\xi_1 \dots \xi_k \dots \xi_{M(r)}\right]^T$, respectively. The elastic influence matrix $\mathcal{A}$ and the mode interaction matrix $\mathcal{L}$ is computed once and for all.

In the coupled NTFA model proposed by Michel and Suquet (2003), the thermodynamic conjugate forces acting on the entire inelastic phase is a quadratic average of all the forces acting on all modes contained within that phase. Following this assumption, the macroscopic damage variable $\overline{\omega}_r$ representing the state of the entire inelastic phase r is introduced. The damage variable depends on the norm of the macroscopic equivalent damage conjugate force vector $\hat{y}$, analogous to the microscopic subcell damage conjugate force $\boldsymbol{Y}^{(\beta)}$. The equivalent force is derived by multiplying Eq. (4.16) by $\boldsymbol{\mu}_k^{(\beta)}$ and averaging over the entire volume:

$$\begin{aligned} y_k{}^{(r)} &= \left\langle \boldsymbol{\mu}_k^{(\beta)} : \boldsymbol{Y}^{(\beta)} \right\rangle \\ &= \left\langle \hat{\mu}_k{}^{(\beta)} \cdot \hat{Y}^{(\beta)} \right\rangle \end{aligned} \tag{4.28}$$

where $\hat{\mu}_k$ and $\hat{Y}$ are the k-th microscopic inelastic mode and the damage conjugate force written in its vector form. In this work, the microscopic inelastic phase is subject to isotropic damage. Hence, the components of the vector $\hat{Y}$ are equal ($Y_1^{(\beta)} = Y_2^{(\beta)} = \cdots Y_6^{(\beta)} = Y^{(\beta)}$), leading to the following expressions:

$$y_k{}^{(r)} = \left\langle m_k^{(\beta)} \cdot Y^{(\beta)} \right\rangle = \frac{1}{2}\left\langle m_k^{(\beta)} \cdot \boldsymbol{\sigma}^{(\beta)} : \boldsymbol{\varepsilon}^{(\beta)} \right\rangle \tag{4.29}$$

$$m_k^{(\beta)} = \sum_{i=1}^{6} \mu_{k,i}^{(\beta)} \tag{4.30}$$

Accounting for the Hill's Mandel condition and static admissibility of the eigenstrain and stress fields along with Eq. (4.21) and (4.22), the above expression is further simplified as

$$y_k{}^{(r)} = \frac{1}{2}\,\bar{\boldsymbol{\varepsilon}}(t) : \mathbb{F}_k : \bar{\boldsymbol{\varepsilon}}(t) - \frac{1}{2}\,\bar{\boldsymbol{\varepsilon}}(t) : \sum_{l=1}^{M(r)} \xi_l(t)\,\boldsymbol{\delta}^{(kl)} \tag{4.31}$$

$$\mathbb{F}^{(k)} = \left\langle m_k^{(\beta)} \cdot \mathbb{A}^{(\beta)^T} : \mathbb{C}^{(\beta)} : \mathbb{A}^{(\beta)} \right\rangle, (k = 1, \dots, M)$$

$$\boldsymbol{\delta}^{(kl)} = \left\langle m_k^{(\beta)} \cdot \mathbb{A}^{(\beta)^T} : \mathbb{C}^{(\beta)} : \boldsymbol{\mu}_l^{(\beta)} \right\rangle, (k, l = 1, \dots, M)$$

The first term in Eq. (4.31) is highly analogous to the damage conjugate force or elastic strain energy defined by Eq. (4.16). The additional term accounts for the mode interaction effects linked by the inelastic mode field and mode activity coefficients. Moreover, the coupled macroscopic equivalent damage variable analogous to the microscopic damage variable in Eq. (4.18) is defined as

$$\dot{\bar{\omega}}^{(r)} = \frac{\dot{\lambda}^{(r)}}{2} f\left(\left\|\hat{y}^{(r)}\right\|_2\right) \tag{4.32}$$

where $\left\|\hat{y}^{(r)}\right\|_2$ is the L^2 norm of the reduced damage conjugate force vector $\hat{\boldsymbol{y}}$. Based on the modified coupled model suggested by Fritzen and Bohlke (2013), the reduced yield function for the phase r analogous to Eq. (4.17) is proposed as

$$\bar{\phi}^{(r)} = \frac{\left\|\hat{\tau}^{(r)}\right\|_2}{1 - \bar{\omega}^{(r)}} - \sqrt{\frac{2}{3}} c_r \sigma_y \tag{4.33}$$

where c_r is the volume fraction of the inelastic constituent in the RUC, i.e., $c_r = \Omega_r/\Omega$. The reduced viscoplastic multiplier analogous to Eq. (4.17) is defined by

$$\dot{\lambda}^{(r)} = \frac{1}{K}\left[\left(\frac{\bar{\phi}^{(r)} + \sigma_y}{\sigma_y}\right) - 1\right]^{1/n} \tag{4.34}$$

Likewise, the cumulative mode activity coefficient vector $\hat{\xi}$ is formulated by pre-multiplying Eq. (4.20) on both sides by $\boldsymbol{\mu}_k^{(\beta)}$, combining with Eq. (4.14) and average over the entire volume:

$$\left\langle \boldsymbol{\mu}_k^{(\beta)} : \boldsymbol{\varepsilon}_D^{(\beta)} \right\rangle = \left\langle \boldsymbol{\mu}_k^{(\beta)} : \boldsymbol{\mu}_k^{(\beta)} \right\rangle \xi_k \tag{4.35}$$

$$\xi_k = \frac{\left\langle \boldsymbol{\mu}_k^{(\beta)} : \omega^{(\beta)} \cdot \boldsymbol{\varepsilon}^{(\beta)} \right\rangle}{\left\langle \boldsymbol{\mu}_k^{(\beta)} : \boldsymbol{\mu}_k^{(\beta)} \right\rangle}$$

Combining with Eq. (4.21), the above expression is simplified and written in a more convenient form:

$$\hat{\xi}^{(r)} = \bar{\omega}^{(r)} \cdot \left(\mathcal{P} \cdot \bar{\varepsilon}(t) + \chi \cdot \hat{\xi}(t)\right) \tag{4.36}$$

$$\mathcal{P}_{ki} = \frac{\left\langle \boldsymbol{\mu}_k^{(\beta)} : \mathbb{A}^{(\beta)} \right\rangle}{\left\langle \boldsymbol{\mu}_k^{(\beta)} : \boldsymbol{\mu}_k^{(\beta)} \right\rangle} : \boldsymbol{B}^{(i)}, (i = 1, \dots, 6;\ k = 1, \dots, M)$$

$$\chi_{kl} = \frac{\left\langle \boldsymbol{\mu}_k^{(\beta)} : \boldsymbol{\eta}_l^{(\beta)} \right\rangle}{\left\langle \boldsymbol{\mu}_k^{(\beta)} : \boldsymbol{\mu}_k^{(\beta)} \right\rangle}$$

It should be noted that the initial heterogenous damage variable field $\omega^{(\beta)}$ is treated as homogenous here, i.e., $\bar{\omega}^{(r)} = \omega^{(\beta)} =$ constant. This assumption is numerically verified in Section 4.5.1. Once the reduced damage state variable $\bar{\omega}_r$ and the associated mode activity

coefficient vector $\hat{\xi}$ are obtained, the macroscopic average stress tensor for the composite is obtained by volume averaging of Eq. (4.22):

$$\bar{\boldsymbol{\sigma}}(t) = \langle \boldsymbol{\sigma}^{(\beta)}(t) \rangle = \bar{\mathbb{C}} : \bar{\boldsymbol{\varepsilon}}(t) + \sum_{k=1}^{M(r)} \xi_k(t) \langle \boldsymbol{\rho}_k^{(\beta)} \rangle \tag{4.37}$$

where $\bar{\mathbb{C}}$ is the macroscopic fourth-order stiffness tensor evaluated numerically using the HFGMC approach. Note that all the system matrices defined in Eq. (4.27), (4.31), and (4.36) are computed once for all. Unlike the HFGMC approach, the reduced constitutive equations are evaluated only once for the entire inelastic phase r at each time step. The total number of internal variables necessary to solve the reduced constitutive equations is equal to the total number of modes $M(r)$.

While the NTFA formulation presented in this section is based on small-strain assumptions, it may be possible to extend the approach to the finite-strain regime, which will be crucial for considering composite microstructures undergoing large deformation, such as hyper elasticity and crystal plasticity. Note that there are no known contributions in the literature demonstrating the extension of the NTFA formulation to the finite-strain regime. For this purpose, the HFGMC boundary value problem can first be formulated in the reference configuration to account for the finite-strain mechanical response. The stress and strain measures of each sub-element become Piola-Kirchhoff stress and deformation gradient tensor. A suitable decomposition procedure can then approximate the deformation gradient field into a set of orthogonal modes. Once the modes are identified, the NTFA theory could lead to a localization rule for the microscale deformation gradient field like Eq. (4.21). Moreover, a reduced free energy term accounting for large deformation and a conjugate force analogous to the Piola-Kirchhoff stress may be derived using the assumptions made in Eq.

(4.23) and (4.24). Nonetheless, extending to large deformation will gain applicability of the approach to geometrically nonlinear problems, which will provide a more rigorous validation standard for the accuracy of the NTFA ROM in the future

4.4 Numerical Implementation

This section presents the numerical implementation of the NTFA ROM using the HFGMC approach to compute the necessary reduced constitutive system matrices and inelastic modes. The individual steps involved in this preprocessing stage of the ROM are illustrated in Figure 22. The first step involves spatial discretization of the composite RUC and prescribing necessary material constants and damage models for the constituent phases. A brief account of the RUC discretization and constituent equations is provided in Section 4.2. Next, several strain path computations are performed on the RUC using the HFGMC micromechanics approach. The computations are used to investigate the following aspects: (i) mechanical strain concentration and effective stiffness tensor of the RUC; (ii) linear eigenstrain analyses necessary for the local NTFA eigenstress field data; (iii) nonlinear simulations generating the inelastic strain snapshots necessary for the mode identification process. Last, the system matrices derived in Section 4.3 are computed based on the generated local field data obtained from strain path computations. Further details are given in the following subsections.

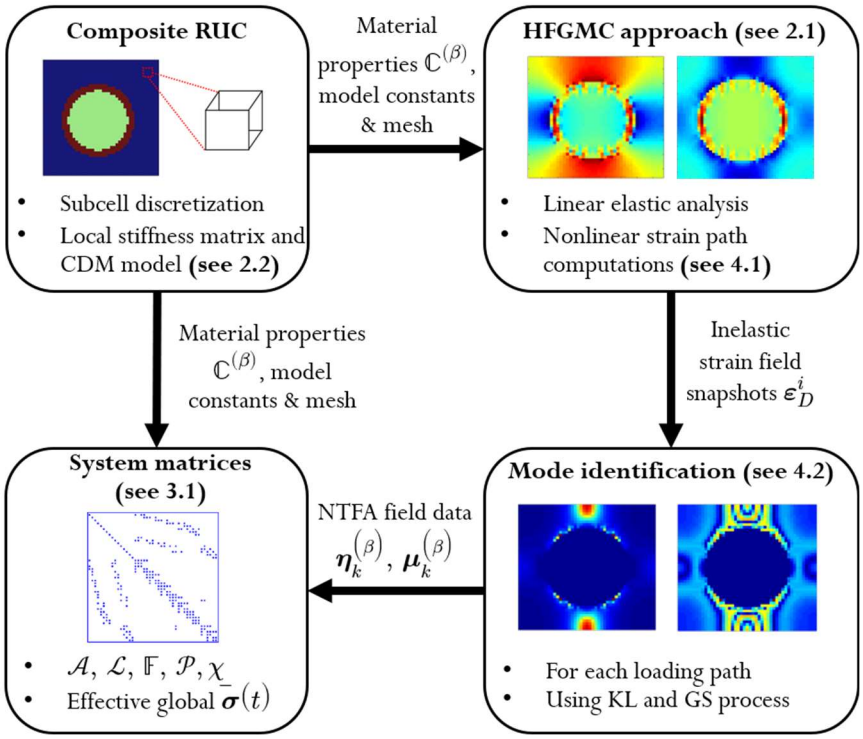

Figure 22. Preprocessing Steps in NTFA-Based ROM

4.4.1 Strain Path Computations

Several numerical computations are performed to investigate the linear elastic properties and each subcell's eigenstrain fields in the generated RUC. For a 3D case, the linear elastic properties are identified from six independent linear elastic simulations of the RUC obtained by solving Eq. (4.10) in Section 4.2.1 as

$$\bar{\mathcal{K}} \cdot \hat{\bar{u}} = \hat{f}\,(\bar{\epsilon}^{(i)}) \tag{4.38}$$

$$\bar{\epsilon}^{(i)} = \epsilon_0 \cdot \boldsymbol{B}^{(i)}\ (i = 1, \dots, 6) \tag{4.39}$$

where $\bar{\epsilon}^{(i)}$ is applied as the average remote strain and ϵ_0 is a positive constant. The solution of Eq. (4.38) enables establishing the following localization relation, which expresses the local strain in subcell (β) in terms of the strain concentration tensor $\mathbb{A}^{(\beta)}$ and remote average strain as

$$\boldsymbol{\varepsilon}^{(\beta)} = \mathbb{A}^{(\beta)} : \bar{\epsilon}^{(i)} \tag{4.40}$$

For each of the six independent elastic strain paths, Eq. (4.40) provides six components of the subcell strain field, which are equal to the elements in the first column of the tensor $\mathbb{A}^{(\beta)}$. Subsequently, the macroscopic fourth-order elastic stiffness tensor is obtained as

$$\bar{\mathbb{C}} = \langle \mathbb{C}^{(\beta)} : \mathbb{A}^{(\beta)} \rangle \tag{4.41}$$

Assuming that the modes are known, the eigenstrain field $\boldsymbol{\eta}_k^{(\beta)}$ created by an inelastic strain field under a vanishing remote average strain field is determined by solving the boundary value problem in Eq. (4.10) while interpreting $\boldsymbol{\mu}_k^{(\beta)}$ as the applied inelastic strain field. The eigenstrain field due to the k-th mode inelastic strain field in phase r is obtained by solving $M(r)$ eigenstress problems given by

$$\bar{\mathcal{K}} \cdot \hat{\bar{u}} = \hat{g}\,(\boldsymbol{\mu}_k) \tag{4.42}$$

where vector $\hat{g}$ contains the traction forces due to the subcell inelastic mode $\boldsymbol{\mu}_k^{(\beta)}$. The local subcell strain obtained from the solution vector $\hat{\bar{u}}$ of Eq. (4.42) is the k-th eigenstrain field. The corresponding eigenstress fields are then computed using Eq (4.22).

Additionally, multiple nonlinear simulations are performed to generate snapshots of inelastic strain fields $\boldsymbol{\varepsilon}_D^{(\beta)}$, necessary for the mode identification procedure discussed in Section 4.4.2. The modes' nature is determined by the strain loading paths used in generating the snapshots of $\boldsymbol{\varepsilon}_D^{(\beta)}$. In general, one can choose any arbitrary multiaxial strain path that the homogenized composite is likely to experience at the macroscopic integration point. For simplicity, the following two strain path computations are considered in the present study:

$$\Sigma_*^{(1)} = \boldsymbol{B}^{(2)}, \qquad \Sigma_*^{(2)} = \boldsymbol{B}^{(2)} + \boldsymbol{B}^{(3)} \tag{4.43}$$

The first loading case is out-of-plane uniaxial normal strain applied along the x_2 −direction. The second case is out-of-plane biaxial normal strains applied along the x_2 and x_3 direction. The corresponding individual computations with the associated strain paths are given by

$$\bar{\epsilon}^{(i)} = \epsilon_0{}^{(i)} \cdot \Sigma_*^{(i)} \; (i = 1, 2) \tag{4.44}$$

The inelastic strain fields generated by each nonlinear computation is temporally discretized into N_f frames or snapshots in the chronological sequence. Therefore, the total number of snapshots are $N_p * N_f$, where N_p represents the number of inelastic strain path computations.

4.4.2 Inelastic Mode Identification

The NTFA formulation proposed by Michel and Suquet (2010) and Fritzen (2013) provided the following requirements for the choice of plastic or inelastic modes: (i) normalization condition with respect to the inelastic phase domain Ω_r, i.e., $\left\langle \left\| \boldsymbol{\mu}_k^{(\beta)} \right\| \right\rangle_r = 1$; (ii) the support of each mode is confined within the corresponding inelastic phase r; (iii) the modes are incompressible, i.e., $tr\left(\boldsymbol{\mu}_k^{(\beta)}\right) = 0$; (iv) the modes are orthogonal to each other, i.e., $\left\langle \boldsymbol{\mu}_k^{(\beta)} : \boldsymbol{\mu}_l^{(\beta)} \right\rangle = 0$, when $i \neq j$. Later, Fritzen (2013) suggested that the normalization condition does not replicate a highly heterogeneous material response. Hence, a modified requirement was proposed, where the modes are normalized with respect to their active plastic or inelastic volume fraction $c_r{}^{(k)}$of the k-th mode:

$$c_r{}^{(k)} = \left\langle 1_{\|\boldsymbol{\mu}_k^0\|_2 > \delta} \right\rangle \leq c_r \tag{4.45}$$

where δ is a cut-off parameter and $\boldsymbol{\mu}_k^0$ denotes the mode before normalization. Note that the k-th active inelastic volume fraction of phase r is always less than or equal to the total volume

fraction c_r A flexible option for the cut-off criteria is to set the parameter $\delta = 10^{-3.....-4} max\left\{\left\|\boldsymbol{\mu}_k^0\right\|_2\right\}$.

Two different mode identification procedures are used and studied here: the Karhunen-Loeve (KL) decomposition and the modified Gram-Schmidt (GS) method. In both methods, the inelastic strain field snapshots $\boldsymbol{\varepsilon}_D^{(\beta)}$ are used to construct modes $\boldsymbol{\mu}_k^{(\beta)}$, essential for the NTFA formulation. The KL decomposition is based on the proper orthogonal decomposition of the correlation matrix K computed using these snapshots. The eigenvalues and eigenvectors of the covariance matrix are used to construct inelastic modes. The dominant modes are retained based on an eigenvalue cut-off parameter α. The modes are then normalized with respect to the active inelastic volume fraction. The decomposition algorithm is presented in Table 5.

Table 5. Algorithm for Karhunen-Loeve Decomposition Procedure

1. Normalize N_f snapshots of damage-induced inelastic strains in phase r

$$\boldsymbol{\varepsilon}_D^i = \boldsymbol{\varepsilon}_D^i \Big/ \left\langle \left\| \boldsymbol{\varepsilon}_D^i \right\| \right\rangle_r \quad (i = 1, \dots N_f)$$

2. Compute correlation matrix K

$$K_{ij} = \left\langle \boldsymbol{\varepsilon}_D^i : \boldsymbol{\varepsilon}_D^j \right\rangle_r \quad (i = 1, \dots N_f, j = i, \dots N_f)$$

3. Compute eigenvalues λ_i and eigenvectors v_i^p. Let $\lambda_i \geq \lambda_j$ for $j > i$

4. Find M dominant eigenvalues based on the cut-off criteria

$$\frac{\sum_{i=1}^{M} \lambda_i}{\sum_{i=1}^{N_f} \lambda_i} \geq \alpha$$

5. Construct $\boldsymbol{\mu}_k^0$ modes using a linear combination of inelastic strains and eigenvectors

$$\sum_{p=1}^{N_f} v_k^p \cdot \boldsymbol{\varepsilon}_D^p = \boldsymbol{\mu}_k^0, \ (k = 1, \dots M)$$

6. Renormalize modes with respect to the active plastic volume of phase r

$$\boldsymbol{\mu}_k = \frac{{c_r}^{(k)} \boldsymbol{\mu}_k^0}{\left\langle \left\| \boldsymbol{\mu}_k^0 \right\|_2 \right\rangle_r}$$

While the KL decomposition method is a straightforward process, it requires the computation of a vast number of L^2 norm products of damage-induced inelastic strain field snapshots. Moreover, due to the sigmoidal nature of the evolution equation in Eq. (4.18), the evolution of inelastic strains is initially nonlinear, followed by linear growth and damage saturation to some extent in the macroscopic loading. Due to the non-gaussian nature of the nonlinear response, the KL method results in dominating coefficients in the correlation matrix K, leading to dominant eigenvalues λ_i mainly affected by the last frames of the snapshots. Consequently, Fritzen and Böhlke (2010) developed an alternative mode identification process known as the modified Gram-Schmidt (GS) method. The GS procedure is based on the L^2 product of inelastic strain fields with a residual threshold based on the snapshots' co-linearity with respect to an existing basis. Unlike the KL method, the GS method cycles through the snapshots in reverse order. The current mode basis is enriched with a new inelastic strain field if the L^2 product exceeds the maximum residual threshold γ. The detailed procedure is presented in Table 6 for the reader's convenience.

Table 6. Algorithm for Modified Gram-Schmidt Process

1. Arrange N_f snapshots in phase r in the reverse order (Last frame to the first frame).

Set i = 0, M = 0

2. Increment i and compute $r_0 = \left\langle \boldsymbol{\varepsilon}_D^i : \boldsymbol{\varepsilon}_D^i \right\rangle_r$

Cycle through $k = 1, \ldots M$ and compute $p_k = \left\langle \boldsymbol{\mu}_k^0 : \boldsymbol{\varepsilon}_D^i \right\rangle_r$
while $r_k = r_{k-1} - (p_k)^2 > \gamma$
if $r_k < \gamma$ go to step 2.

3. if $r_M > \gamma$, compute new mode

$$\boldsymbol{\mu}_{M+1}^0 = \frac{\left\{ \boldsymbol{\varepsilon}_D^i - \sum_{k=1}^{M} p_k \boldsymbol{\mu}_k^0 \right\}}{\sqrt{r_M}}$$

M = M+1. Go to step 2

4. Normalize modes with respect to the volume containing inelastic phase r

$$\boldsymbol{\mu}_k = \frac{{c_r}^{(k)} \boldsymbol{\mu}_k^0}{\left\langle \left\| \boldsymbol{\mu}_k^0 \right\|_2 \right\rangle_r}$$

A total of 200 snapshots are generated for the two inelastic strain path computations defined by Eq. (4.44). Based on these snapshots, both the KL and GS mode identification process returns a set of inelastic modes for each case. For the KL method, the eigenvalue cut-off parameter is set to 0.9999. For the GS method, the residual threshold is set to $\gamma = 10^{-9}$ to generate enough modes for each loading case. The modes extracted for the first strain path computation using the two approaches are illustrated in Figure 23. The first and last equivalent modes extracted in the matrix phase by applying the KL method are shown in subfigures (a) and (c) of Figure 23. Subfigures (b) and (d) show the equivalent modes extracted using the G-S method. It is worth mentioning that the first mode identified by both these methods is, to some extent, similar. Unlike the KL method, the GS method constructs additional modes

based on the subsequent inelastic strain field's co-linearity concerning the first mode. Consequently, the last mode identified by the two methods is very distinguishable. Note that the GS approach returns more inelastic modes than the KL approach for the two strain path computations. A summary of the number of modes obtained for each strain path computation for the two approaches is shown in Table 7. Before concluding in favor of the two approaches, it is worth comparing both methods' accuracy in predicting the local and global field quantities of the RUC.

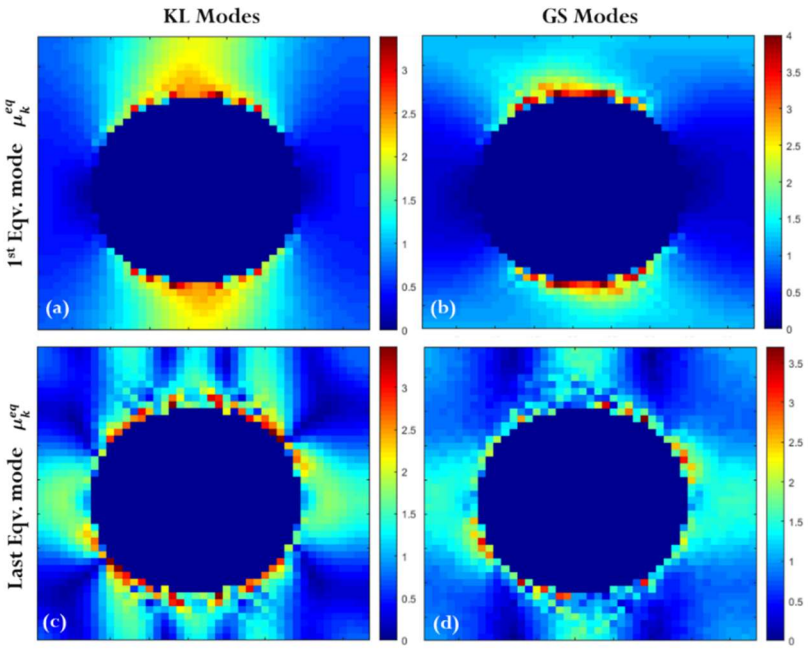

Figure 23. Illustration of Inelastic Modes for the Two Approaches For (Test Case 1).

Table 7. Number of Modes for Two Strain Paths

	$\boldsymbol{\Sigma}_*^{(1)}$	$\boldsymbol{\Sigma}_*^{(2)}$
KL modes	7	5
GS modes	9	8

4.5 ROM Verification

The FFRP composite RUC shown in Figure 21 is generated using a 30 % fiber volume fraction and a 40 % polymer crosslinking degree. The crosslinking degree affects the polymer Young's modulus based on the findings presented in Rai et al. (2017). The CNT-enhanced interphase thickness is ~1 um, corresponding to a 5 um fiber diameter. The RUC is discretized into 10x43x43 subcells with ten subcells in the fiber direction. The constituent elastic properties and necessary damage model parameters are given in Tables 8 and 9. The RUC is subject to the two strain path computations defined in Eq. (4.44). The first test case is for out-of-plane uniaxial normal loading and the second case is for out-of-plane biaxial normal loading. It is worth mentioning that the current study primarily focuses on introducing the detailed procedure for the NTFA formulation with the HFGMC theory and the localization functions necessary to account for the damage-induced inelastic strain fields in the individual micro constituents. Hence, the choice of the two idealized inelastic strain paths is merely to verify and validate the assumptions made to derive the coupled damage conjugate force and the macroscopic damage variable analogous to its microscopic counterpart, as given in Eq (4.28) and (4.32). Verification of the ROM's predictive capability for more realistic loading conditions and implementing a different mode identification procedure, if necessary, will remain an aspect of our future work.

In the present work, the NTFA ROM predictions based on the inelastic modes identified using KL and GS methods are compared with full-field HFGMC simulations for the two test cases. The comparison is carried out for three types of model response: (i) effective response of the composite RUC; (ii) local stress field contour; and (iii) probability distribution of local

stress field norm in all phases. Additionally, the computational cost of the ROM and HFGMC simulations is discussed.

Table 8. Elastic Material Properties for Micro Constituents

Material	E_1 (GPa)	E_2 (GPa)	E_3 (GPa)	G_{12} (GPa)	G_{13} (GPa)	G_{23} (GPa)
Fiber	294	18.5	18.5	7.1	7.1	25
Epoxy	2.2	2.2	2.2	0.76	0.76	0.76
Interphase	17.32	15.39	27.61	2.35	4.58	3.16

Table 9. CDM Model Parameters for Matrix Phase

$\boldsymbol{\theta}$	$\boldsymbol{Y_0}$ (MPa)	$\boldsymbol{\sigma_0}$ (MPa)	$\boldsymbol{G}$ (s)	$\boldsymbol{n}$
0.40	0.12	60	15	2.5

4.5.1 Effective response

The effective RUC response of the two NTFA ROM test cases are obtained using Eq. (4.37) and are illustrated in Figures 24 and 25. The L^2 norm of the effective RUC stress field $\|\bar{\boldsymbol{\sigma}}\|_2$ predicted based on KL and GS modes are compared with HFGMC simulations, as shown in Figures 24 (a) and 5(a). The evolution of the macroscopic damage variable in the matrix phase r is also compared for the two cases, as shown in Figures 24(b) and 5(b). The damage state variable for the NTFA ROM $\bar{\omega}^{(r)}$ is computed using Eq. (4.32). The damage variable for HFGMC simulations is computed by volume averaging over the subcell damage operator as $\bar{\omega}^{(HFGMC)} = \langle \omega^{(\beta)} \rangle_r$.

For both the test cases, the predicted RUC stress field norm $\|\bar{\boldsymbol{\sigma}}\|_2$ and macroscopic damage $\bar{\omega}$ are in good agreement with HFGMC simulations. In the case of $\|\bar{\boldsymbol{\sigma}}\|_2$, the NTFA ROM based on GS modes shows overall better prediction accuracy than using KL modes. The same

conclusion applies to the predicted macroscopic damage evolution. The homogenized damage $\bar{\omega}$ predicted using GS modes shows an overall minimal discrepancy between the ROM and HFGMC macroscopic damage state. Nevertheless, both KL and GS modes can capture the initial acceleration, a steady-state growth, followed by saturation due to the sigmoidal nature of damage evolution defined by Eq. (4.18). Moreover, these close agreements are also a numerical verification for the assumptions used to derive Eqs. (4.28), (4.32), and (4.36), where the heterogeneity due to local subcell damage variables $\omega^{(\beta)}$ is treated as homogenous in the entire phase, i.e., $\bar{\omega}^{(r)} = \langle \omega^{(\beta)} \rangle_r$. Further studies are carried out to investigate the local stress field in individual constituent phases.

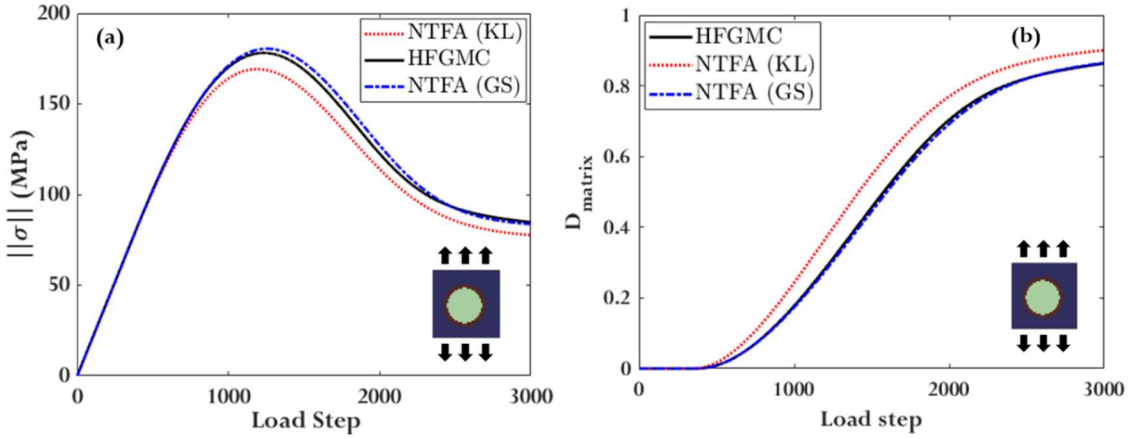

Figure 24. Comparison Between HFGMC and ROM for Test Case 1: (a) Effective RUC Stress Norm; (b) RUC Damage Evolution

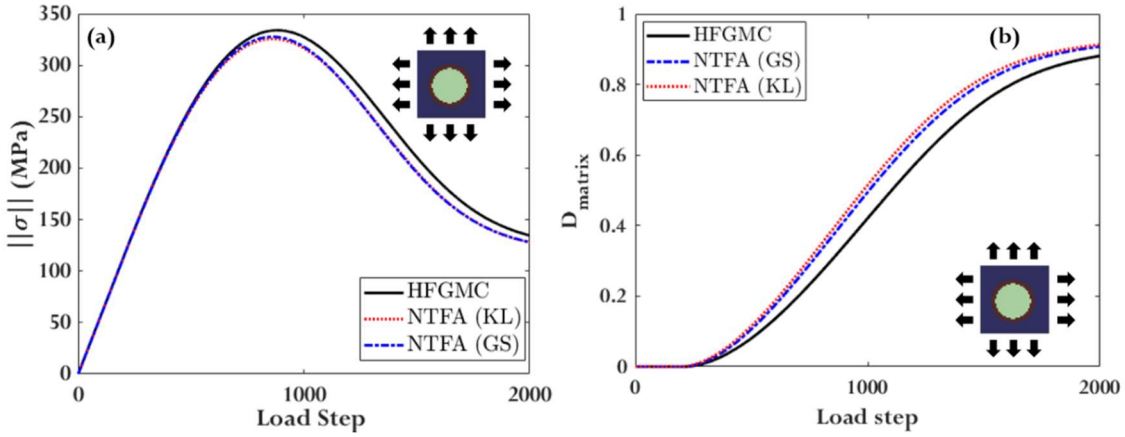

Figure 25. Comparison Between HFGMC and ROM for Test Case 2: (a) Effective RUC Stress Norm; (b) RUC Damage Evolution

4.5.2 Local stress fields

In each constituent phase, the local stress field predicted using the NTFA ROM is compared with HFGMC simulations at peak RUC stress and the end of the load step. The ROM subcell stress fields are reconstructed using Eq. (4.22). The L^2 norm of the subcell stress field $\left\|\boldsymbol{\sigma}^{(\beta)}\right\|_2$ is used, and the comparison is made for predictions based on KL and GS modes. Figure 26 shows the comparison of the local stress field obtained for test case 1. Both KL and GS show good agreement with the HFGMC simulation at peak stress (t = 1250). However, the predictions based on KL modes do not capture the local stress field contour at the end of the load step (t = 3000). The local stress field mismatch is more significant in the matrix region, attributed to the KL method's inability to capture non-gaussian (sigmoidal) damage evolution (Eq 4.18). In contrast, the stress contour predicted using GS modes shows good agreement with the HFGMC simulation with only a slight discrepancy in some matrix regions around the fiber. Nevertheless, the GS modes are sufficient to capture the general heterogeneity in the

local stress field due to the mismatch in material properties between the fiber, matrix, and explicit interphase region.

A similar conclusion applies to the predicted RUC stress field contour for test case 2 (see Figure 27). The ROM using GS modes shows better prediction accuracy at peak RUC stress (t = 900) and the end of the load step (t = 2000). The discrepancy in the stress field contour predicted based on GS modes at t = 2000 remains small compared to the local stress field predicted using KL modes. The probability distribution of the local stress field in each phase obtained for the two test cases is investigated in the following subsection.

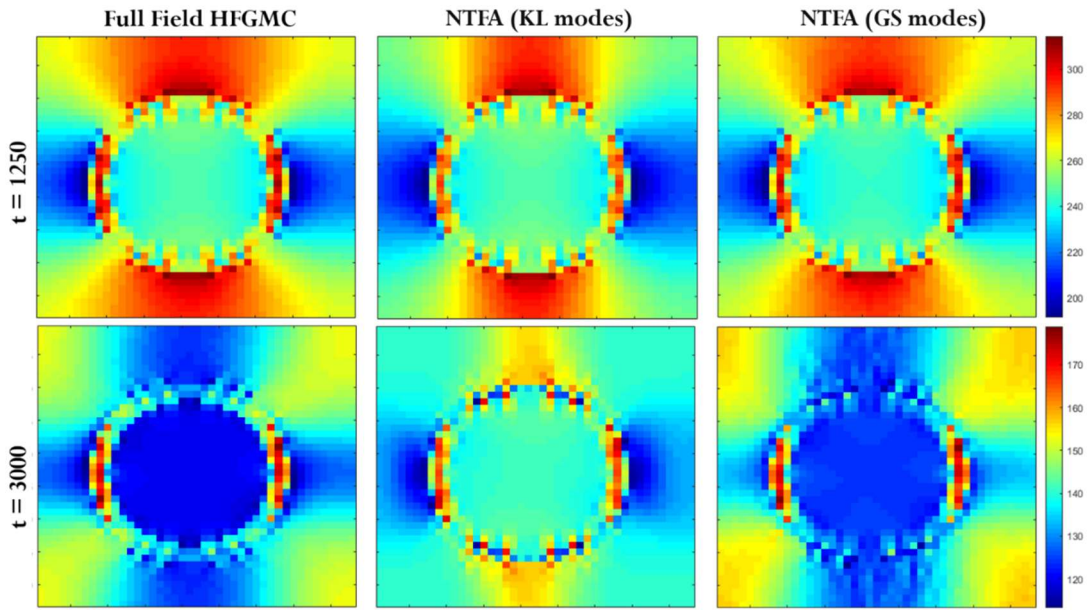

Figure 26. Comparison of Norm of RUC Stress Field Contour for Test Case 1.

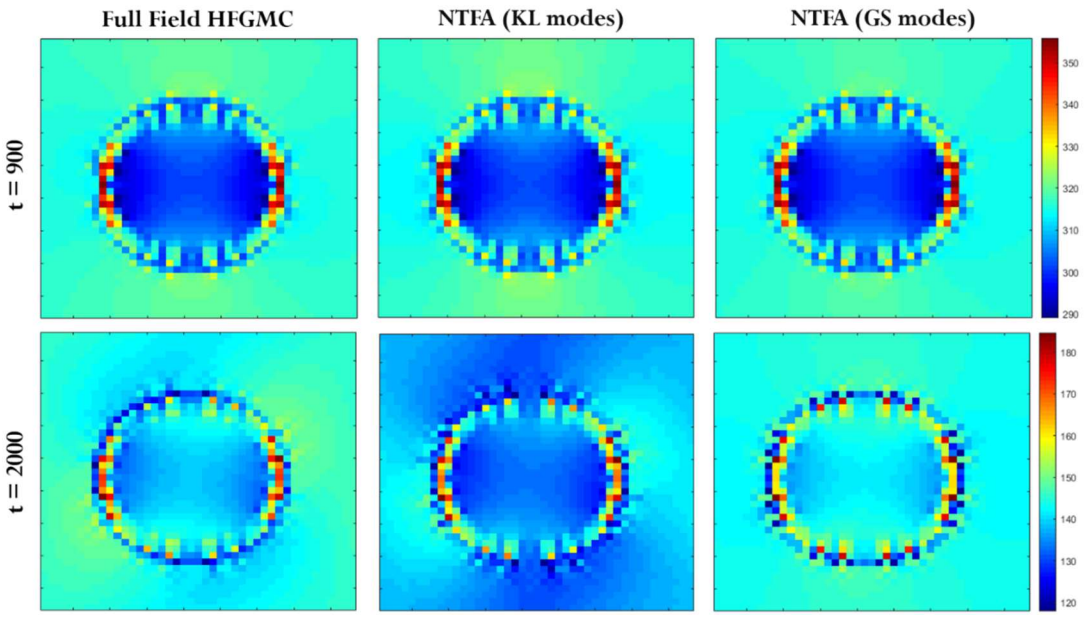

Figure 27. Comparison of Norm of RUC Stress Field Contour for Test Case 2.

4.5.3 Local stress distribution of the phases

The ROM predictions for the local stress distribution in each phase are compared with full-field reference simulations. The L^2 norm of the local subcell stress field $\left\|\boldsymbol{\sigma}^{(\beta)}\right\|_2$ is used, and its probability distribution in each phase is compared with HFGMC simulations. For this purpose, a quantile-quantile (q-q) plot is used to determine whether the local stress fields obtained from the ROM and HFGMC computations come from the same distribution family. A 45^0 reference line is plotted using the quantiles of both the data sets. If the two data sets come from the same distribution, the data points should fall close to this reference line. The comparison is made for both KL and GS modes.

Figure 28 shows the q-q distribution plot of each constituent phase predicted using KL modes for test case 1. The comparison is made at peak RUC stress. Figure 28 (b) shows that the local stress distribution in the fiber and interphase is in good agreement with HFGMC

simulation. However, the inelastic matrix phase's distribution shows some deviations from the reference data set (see Figure 28 (a)). On the other hand, the probability distribution of local stress fields predicted based on GS modes is in excellent agreement with HFGMC simulations, particularly in the matrix phase, as shown in Figure 29.

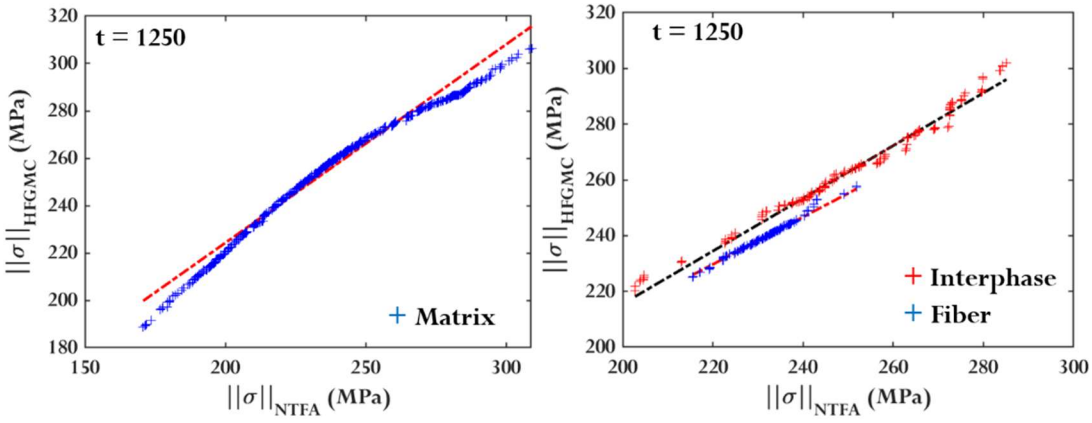

Figure 28. Distribution of Norm of Local Stress Field Using KL Modes (Test Case 1)

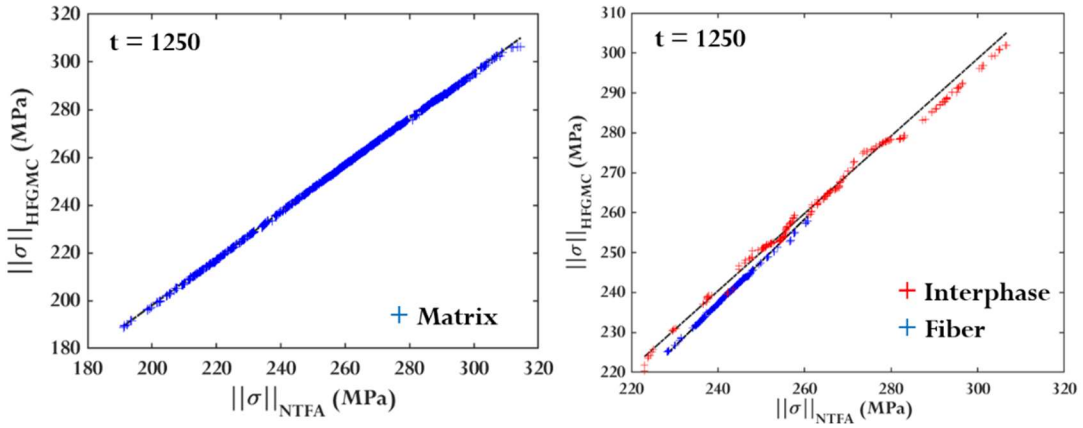

Figure 29. Distribution of Norm of Local Stress Field Using GS Modes (Test Case 1)

For test case 2, the comparison is made at peak RUC stress and the load step's end. Figure 30 shows the q-q distribution plot of each constituent phase predicted using KL modes. The local stress distribution in all three phases is in good agreement with HFGMC simulations at peak RUC stress (t = 900 in Fig. 25 (a)). However, the probability distribution of the phases

based on KL modes at the end of the load step (t = 2000) does not agree well with the reference data set from HFGMC simulations. Figure 31 shows the q-q distribution plot predicted using GS modes. In contrast to KL modes, the distribution of stress fields predicted using GS modes is in good agreement with HFGMC simulations at peak RUC stress and the end of the load step. These comparisons further show that the GS modes can adequately capture the heterogeneity in the local stress field.

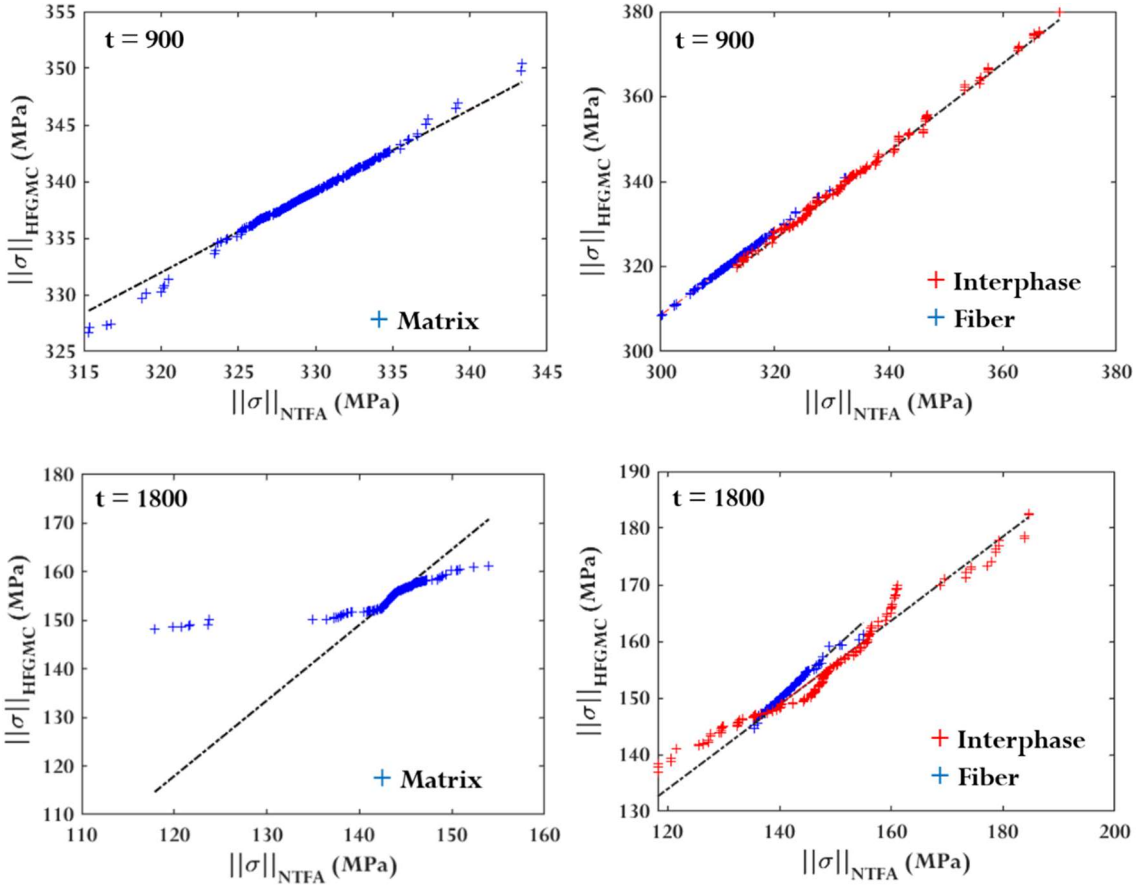

Figure 30. Distribution of Norm of Local Stress Field Using KL Modes (Test Case 2)

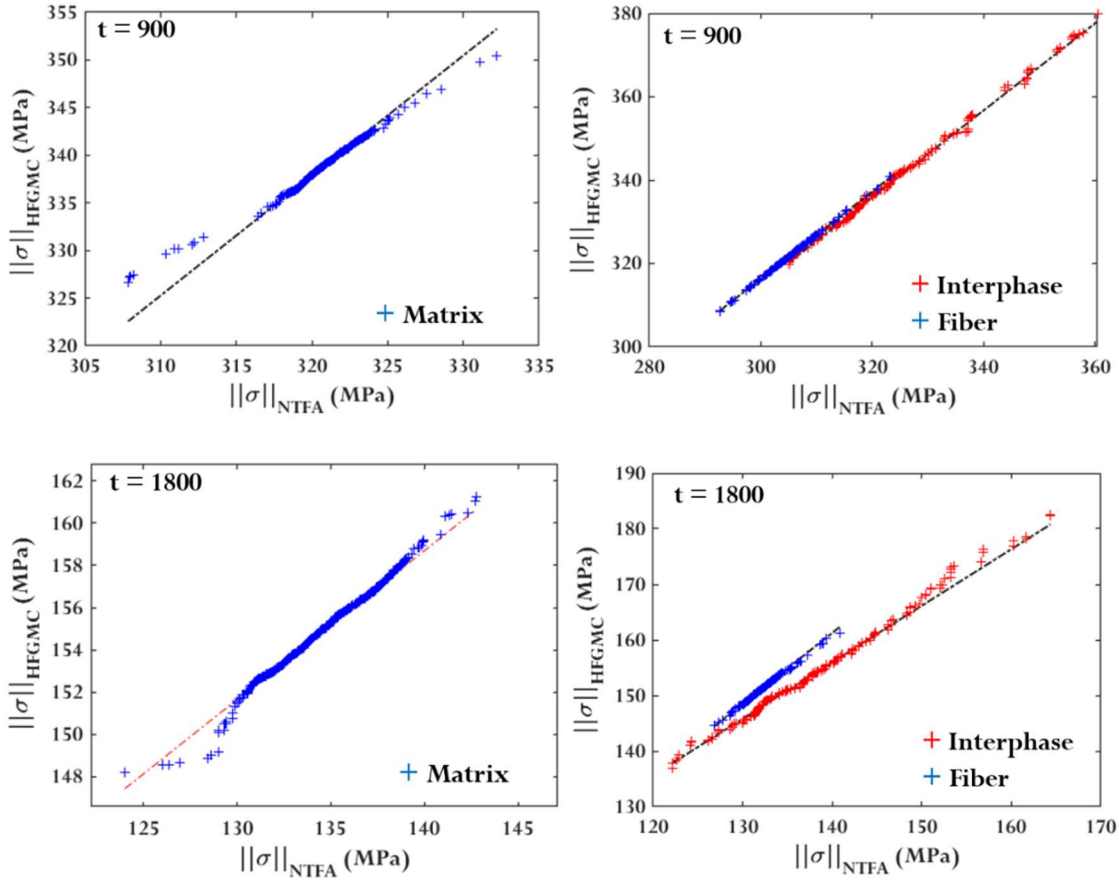

Figure 31. Distribution of Norm of Local Stress Field Using GS Modes (Test Case 2)

4.5.4 Gain in Computational Time

All computations were performed on an Intel Xeon Processor ES-2680 machine consisting of 28 cores with 4 GB memory per core. The computational cost of the ROM and HFGMC simulations are compared for test case 1. The CPU time taken to solve the composite RUC with ~18,000 subcells using HFGMC simulations was around 13,680 secs. The HFGMC implementation results in 162,000 global systems of equations with 162,000 unknowns for the entire RUC. As a result, the full-field computations required over 4 GB of memory to store the global stiffness matrix defined in Eq. (4.9), together with the history and damage state variables for each subcell in the RUC.

In contrast, the NTFA approach shows significant improvement in both the computational time and memory requirements. The NTFA approach using KL modes has only seven internal variables (one per mode) for the entire RUC and took about 53 secs to predict the overall effective behavior defined by Eq. (4.35). The local field quantities are only reconstructed at any specific point in the load step when necessary. Likewise, the NTFA approach using GS modes (nine internal variables) took about 92 secs to predict effective RUC behavior. The two NTFA cases differ in cost by a factor of 1.73 approximately. However, the gain in CPU times obtained by using the NTFA approach over the HFGMC simulations is by a factor of over 100.

Moreover, the NTFA implementation required well below 500 MB of memory to simulate the same composite RUC and store all the necessary internal variables, system matrices, and local subcell field data. This reduction by over eight orders of magnitude in the memory requirement enables the NTFA implementation to efficiently simulate RUCs with a much finer discretization at every macroscopic integration point.

4.6 Summary

A reduced-order model (ROM) for composite materials based on a novel adaption of the nonuniform transformation field analysis (NTFA) with the high-fidelity generalized method of cells (HFGMC) theory was developed. The original NTFA theory was extended to account for material nonlinearity due to damage at the micro constituent level. A distinctive feature is that the continuum damage state variable was formulated as damage-induced inelastic strains, which allowed applying the superposition principle in the NTFA theory and solving the phase transformation strain or eigenstress fields. The nonuniformity in this inelastic strain field was approximated using tensorial modes that serve as deformation shape functions. A

macroscopic damage state variable was formulated to have the same evolution function as its microscopic counterpart using a finite number of inelastic modes.

The ROM's ability to handle highly heterogeneous local fields between constituent interphases, in addition to damage softening, was demonstrated for normal loading conditions. This was encountered in three-phase nanocomposites defined by nanoengineered orthotropic fiber-matrix interphase and matrix phase subject to damage, which was chosen to illustrate the developed theory. Two different mode identification approaches were investigated: (i) Karhunen-Loeve (KL) decomposition and (ii) Gram-Schmidt (GS). Both approaches captured the effective RUC stress response and damage evolution with enough accuracy. The model with GS modes showed overall better accuracy for the predicted local stress field distribution. The NTFA approach showed a significant improvement in computational time and memory requirements than the HFGMC approach, making the model attractive for large-scale concurrent multiscale simulations. The current NTFA formulation forms the basis for further developing the theory to account for nonlinearity due to rate-dependent plasticity and damage effects with improved predictive accuracy.

While the two idealized inelastic strain paths in Section 4.4 verify the assumptions made in deriving the reduced-order CDM formulation analogous to its microscopic counterpart, the applicability of the ROM in multiscale simulations requires verification under more realistic loading conditions. It is important to note that under complex loading such as combined transverse tensile/compressive and transverse shear, the CDM computation results in highly heterogeneous damage localization bands that deflect and evolve within the composite microstructure.

Since the present CDM model and HFGMC theory do not account for mesh objectivity, an alternative formulation is needed to capture more realistic cases where mixed-mode damage

or crack localization bands appear and evolve across periodic boundaries. For example, integral-based non-local theories can simulate a progressive transition from diffuse damage to strain localization and regularizing continuum damage evolution. Therefore, similar theories can be incorporated within the HFGMC framework to regularize the present CDM model and capture damage-dependent non-local interactions. This could help achieve mesh objectivity and capture fully bridged damage localization bands under more realistic loading conditions. In the context of the proposed approach, the NTFA deformation modes can now be based on damage-induced inelastic strain fields obtained using regularized non-local CDM computations. Besides, the ROM utilizes strain concentration tensors for each sub-element, which are precomputed using the second-order displacement fields of the HFGMC theory and introduce normal-shear coupling. Therefore, with sufficient inelastic modes, the developed NTFA ROM is expected to effectively capture the formation and evolution of highly heterogeneous localization bands. The investigation of the method's predictive capability under complex loading conditions and its implementation into a commercial finite element code for multiscale analysis is a prospect for future research.

CHAPTER 5

HIGH FIDELITY MODELING OF SANDWICH SPACE STRUCTURES

5.1 Introduction

A secondary objective of the research presented in this proposal is developing a high-fidelity modeling framework that allows for a consistent way of performing mechanical and thermal strength analysis to correlate the failure response of composite sandwich structures with experimental observations. Earlier efforts to model sandwich structures involved using well-established analytical approaches such as equivalent single layer and higher-order sandwich panel theories (Mindlin 1951; Reddy 1984; Najafizadeh and Heydari 2004; Dafedar and Desai 2002; Kapuria and Achary 2004). In general, an equivalent single layer is defined with the same bending stiffness as the skins only while neglecting core through-thickness flexibility and any interactions between the skin and core. The higher-order theories account for the through-thickness flexibility of the core and can be used to investigate hygrothermal effects, buckling, and nonlinear behavior in sandwich panels (Frostig 1997; Frostig and Thomsen 2005). Likewise, the core sheet material with a complex cellular geometry is often modeled as a single orthotropic layer with homogenized stiffness properties estimated using various analytical theories (Klintworth and Stronge 1988; Yang and Becker 2004). While these methods are useful in preliminary design and quick estimates, they are not suitable for predicting the strength, localized damage hot spots, and failure mechanisms accurately.

FE modeling is a popular tool in analyzing complex structures and has been widely used to capture nonlinear responses in composite sandwich structures. Layered shell elements, whose elastic properties are derived using classical laminate theory, are widely used in FE

analysis to simulate core as one of the laminate layers (Li et al. 2016; Liu et al. 2016). However, this approach does not fully capture the bending and shear behavior of the panel and fails to account for failure modes, such as delamination. On the other hand, composite laminates modeled using several layers of solid brick elements capture the through-thickness stresses and the stresses at the layer's interface, which becomes significant with an increase in the number of plies. Using linear elastic properties combined with failure criteria can predict strength; however, it fails to predict damage initiation and evolution in composite sandwich materials. As a result, progressive damage models are implemented to capture the initiation and evolution of damage in thin composite skins before the structural collapse.

The properties of the core sheet material are accurately estimated by explicitly modeling the complex core cellular geometries (Russel et al. 2011; Giglio et al. 2012; Chamis et al. 1986). The use of explicitly modeled honeycomb core sheet geometry using 3D shell elements accurately captures the orthotropic stiffness behavior and local failure mechanisms such as core shear and cell wall buckling (Lyford and Andrew 2017). It is worth mentioning that structural loads on adhesively bonded fittings and joints cause localized core buckling near the fitting region and often lead to premature joint failure (Smith and Banerjee 2012). Hence, it may be more appropriate for representing the detailed cellular geometry in such composite sandwich panels to capture the localized nonlinear effects, despite the increase in model size and added computational cost.

This chapter presents an investigation into the thermal degradation and failure response of complex composite sandwich structures with adhesively bonded metallic fittings subject to cyclic thermal loading. First, detailed analyses are conducted to investigate the failure and predict the intrinsic nonlinear material properties of sandwich panels with a specific aerospace-grade Aluminum 5056 honeycomb core and an MJ-type high modulus fiber/cyanate ester-

based resin composite skin. The cellular honeycomb core geometry and the composite skin, fittings, and adhesives are modeled using shell and solid finite elements. A cup joint is chosen to investigate the honeycomb core buckling failure under cup pull-out loading normal to the panel. The nonlinear effects of the core shearing and the local plastic deformation in the Aluminum 5056 alloy are analytically predicted to match the test coupon's load versus displacement curve. An H-Clip fitting bonded to the sandwich panel's edge is then used to investigate the progressive damage response of the M55J/CE-3 resin composite skins. Sandwich panels with H-Clip fitting loaded under shear, normal, and pull-off directions exhibit failure modes involving face sheet compression, core failure, and face wrinkling. A CDM-based failure model is developed and implemented as a user-defined material subroutine to capture the stiffness degradation and associated failure modes in the composite face sheet. The damage model parameters are calibrated to match the predicted load-displacement curve with experiments under different loading conditions.

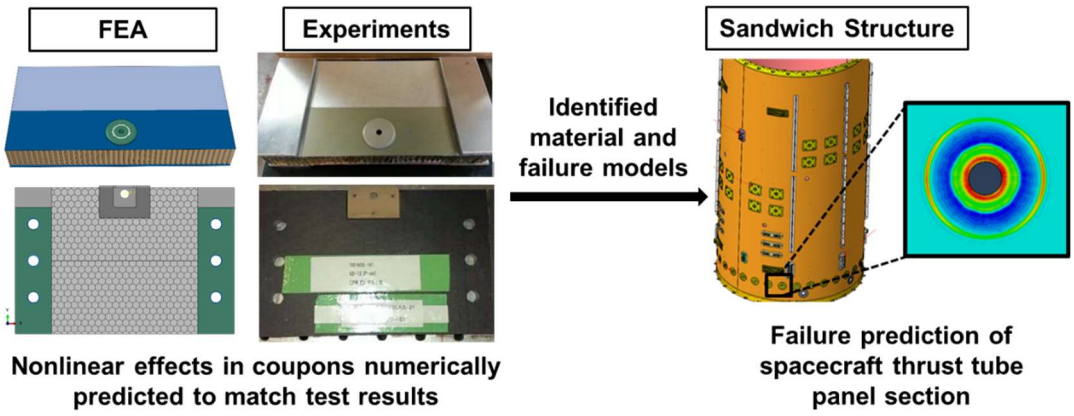

Figure 32. Schematic of High Fidelity Analysis of Sandwich Structures

Last, the nonlinear material properties and modeling strategies are incorporated in the subsequent FE analysis of a spacecraft's thrust tube sandwich structure with bonded metallic

fittings subjected to cyclic thermal loading. Figure 32 illustrates the modeling framework and the information flow. Detailed stress and failure analysis are performed considering the complex stress states developed in the core, face sheet, and adhesives. The predicted damage hot spots of the sandwich panel coupon with a cup bonded fitting are correlated with the expected response and experimental observations. The developed methodology for analyzing sandwich structures can be extended to investigate spacecraft thrust tube sections with other configurations of bonded joints and fittings.

5.2 Methodology

A typical sandwich structure comprises thick sandwich panels, thin adhesive layers, and metallic fittings. High-fidelity FE models are built using Abaqus commercial software (ABAQUS 2013) with explicitly modeled adhesive elements, honeycomb core geometry, and composite face sheet. The material parameters required to capture damage and failure in specific grade honeycomb core and composite face sheets are not well reported by the manufacturer or in the published literature, owing to the experimental difficulties associated with testing small-diameter fibers and multiple configurations of core sheet geometry. Therefore, the initial goal is to investigate failure mechanisms and predict the necessary constitutive parameters for the specific Aluminum 5056 honeycomb core and M55J/cyanate ester-based resin composite material. The estimated parameters and the methodology are then incorporated to analyze a spacecraft's thrust tube composite structure with metallic fittings subjected to thermal cycling.

5.2.1 Cup Fitting Coupon with Normal-to-panel Loading

5.2.1.1 Model Setup

The developed FE model consists of the cup fitting bonded to the sandwich panel made of Aluminum 2024 alloy face sheets, as illustrated in Figure 33. The cup fitting is designed to hold the load in the center of the panel and is often used to support components or adjacent panels. The coupon has two adhesive bond lines: the lower and the upper bond lines between face sheet and cup fitting. The adhesives have a general thickness of 0.01 inches and are modeled as EA9309.NA material with elastic and plastic properties was obtained from (Stapleton et al. 2010). The cup fitting is modeled as a 7075-T6 aluminum alloy with elastoplastic constitutive properties (Dey et al. 2016). The face sheet/adhesive/cup fitting interface is modeled as perfectly bonded with common nodes shared by their corresponding elements (Chen and Yan 2012). The inner surface of the face sheet is connected to the edge nodes of the honeycomb core-shell geometry using node-surface-based TIE constraints. The fitting and adhesives are modeled using solid brick elements with reduced integration points to ensure adequate load transfer to the panel with a decreased computational cost. The panel face sheets are modeled using reduced-integration shell elements since the face sheet is not expected to contribute to the failure of the cup fitting. However, the honeycomb core is expected to contribute to failure; hence, shell elements with four integration points are used. The fully-integrated shell elements cannot hourglass and are used to accurately model the regions undergoing large deformation due to core buckling. The final model resulted in approximately 114462 and 18756 shell elements generated for the honeycomb core and face sheet, respectively, and 7473 solid elements for the adhesives and cup fitting.

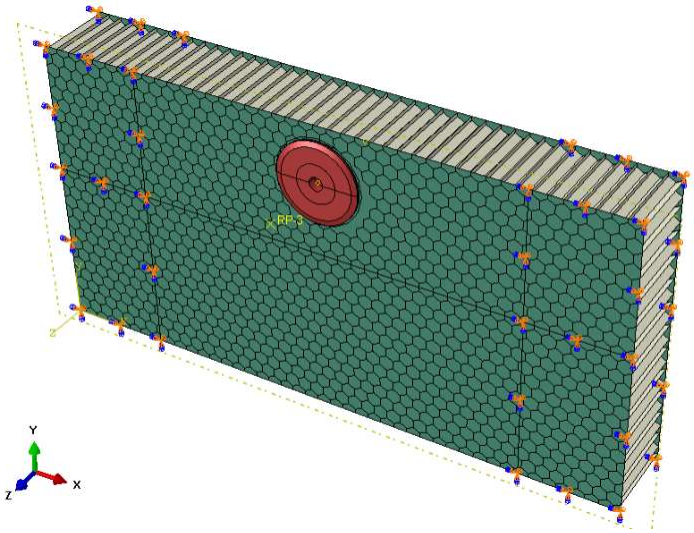

Figure 33. FE Model of Sandwich Panel with Aluminum Skin and Cup Fitting

While the face sheet/adhesive/fastener interface transfers load from the cup to the panel, the honeycomb core is responsible for transferring load between the face sheet by carrying the load in shear. The cell walls of the honeycomb geometry plastically deform when the core exceeds its shear strength capabilities. In the developed model, the honeycomb core utilizes an Aluminum 5056-H39 alloy foil material and has a 3.1 pcf (per cubic feet) nominal density. The specific temper of aluminum 5056 is almost exclusively used as a component of the manufactured honeycomb sheet. There is very little information providing specific strength properties for the material itself. Hence, yield strength of 50 ksi and ultimate strength of 60 ksi was initially assumed, and the stress-strain curve was fit around these values based on the known modulus and a typical stress-strain pattern, as shown in Figure 34 (a). The cell wall thickness is altered to simulate the manufacturing tolerances and account for imperfections in the honeycomb material. The thickness is reduced by ~10 % in all the honeycomb core cells. A flatwise pull-out load test is simulated by imposing a Z-axis displacement, which attempts to pull the cup out of the panel. The load is applied through a reference point tied to a set of

nodes in the fitting that simulates the fastener region. The coupon's load-displacement response is readily obtained from the reference point and compared with experimental data.

The experimental results for the cup fitting coupon were obtained from a previous investigation by Lyford and Andrew (2017). The coupon test was conducted using an Instron universal testing machine. A fastener was mounted inside the cup fitting that was closer to the edge of the panel. The coupon test was conducted by pulling the fastener in the flat-wise normal direction, as shown in Figure 35. The coupon was secured to a pair of aluminum reaction plates that sandwiched the coupon and reacted to the applied load. The deflection at the head of the tensometer was measured as well as the applied load. Six coupons were tested to ensure the results were reliable and the failure modes were consistent.

5.2.1.2 Analysis and Discussion

In the previous study, a modified Riks' method in the Abaqus/Standard was chosen as the solver to capture the post-buckling response of the honeycomb core. Rik's method required artificially smeared shape eigenvectors onto the honeycomb core mesh to trigger the cell wall buckling. While the approach showed good accuracy, the method may not work well with larger models with significant discontinuities in the solution. Moreover, introducing local imperfections to trigger buckling artificially becomes highly dependent on numerical parameters rather than a consequent physical process. In this investigation, the Abaqus/Explicit solver is chosen to simulate the global nonlinear response due to local cell wall buckling. The explicit dynamics method with low loading rates ensures minimal inertial effects and can physically simulate global nonlinear behavior due to local plastic or damage response. Moreover, the need to simulate progressive material degradation and failure with

element deletion makes the dynamic solver suitable for efficient nonlinear analysis. In the present analyses, an enhanced viscous-based hourglass control is used to suppress spurious energy modes and mass scaling to achieve the critical stable time increment.

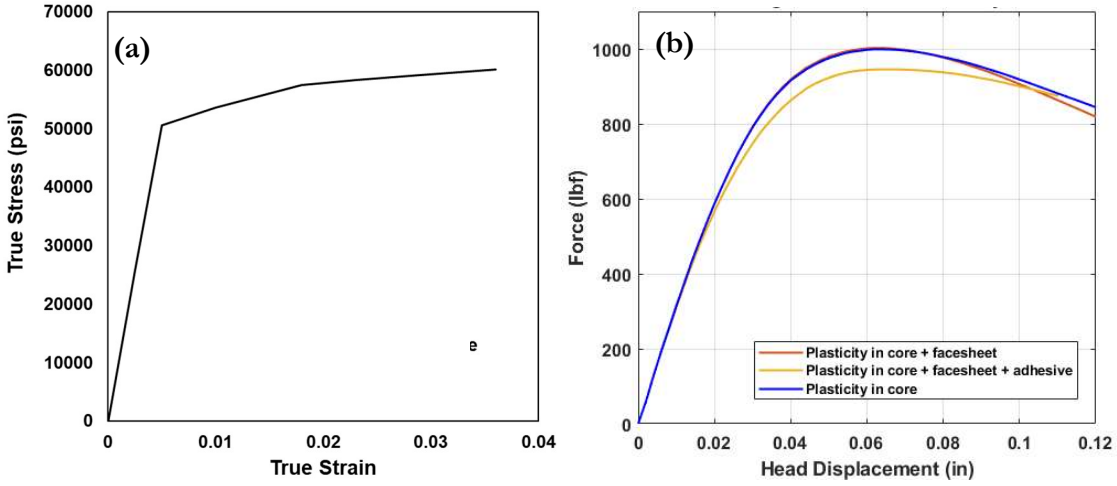

Figure 34. (a) Stress-Strain Curve for Al 5056 Alloy; (b) Effect of Plastic Deformation

Sensitivity studies are conducted to understand the significance of plasticity in the aluminum core, face sheet, and adhesive. Figure 34 (b) compares the load-displacement response for different cases of plasticity in the various components. The global nonlinear and failure response is primarily dominated by the localized plastic deformation in the aluminum 5056 material, which leads to core cell wall buckling. The plasticity in the aluminum face sheet is only notable in the later stages of the load-displacement response. However, the load-displacement response collapse occurs much earlier when the plasticity in the adhesive is considered.

Additionally, core buckling is observed to be localized around the cup fitting region. The local structure stresses and deformation shape from the model are compared to that of the

experiments (Lyford and Andrew 2017). As seen in Figure 35, the buckling pattern is physical and correlates well with the experimentally observed pattern.

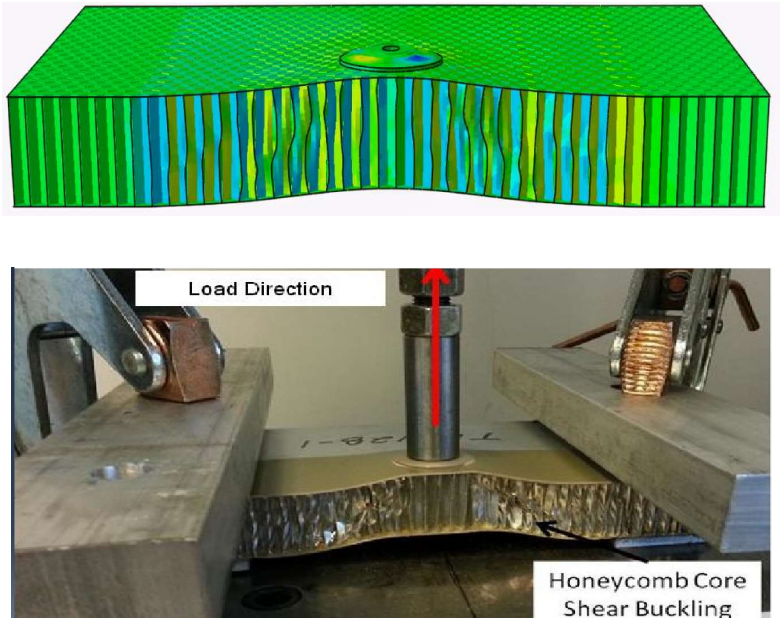

Figure 35. Comparison Of Predicted Buckling with Experiments (Lyford And Andrew 2017)

A preliminary comparison of the model response with the test results shows that the predicted coupon stiffness agrees well with the stiffness of the tested coupon. However, the point of departure from the linear part of the load-displacement response and the ultimate failure load did not match the test results. The Al 5056 alloy stress-strain curve is numerically estimated to minimize the predicted post-linear coupon response discrepancy. The yield strength of 50 ksi was too high to correlate with the core failure due to shear buckling. Hence, the yield strength is reduced to 40 ksi, and a smooth transition from the yield point to the ultimate strength is established to sufficiently match the point of departure from the linear part of the load-displacement curve and the ultimate load (see Figure 36 (a)). The model predictions using the estimated honeycomb core material properties compare well with the various test coupon results shown in Figure 36 (b). The calibrated stress-strain curve for the

Al 5056 core material will be used for subsequent analysis of honeycomb sandwich panel coupons discussed in the next section.

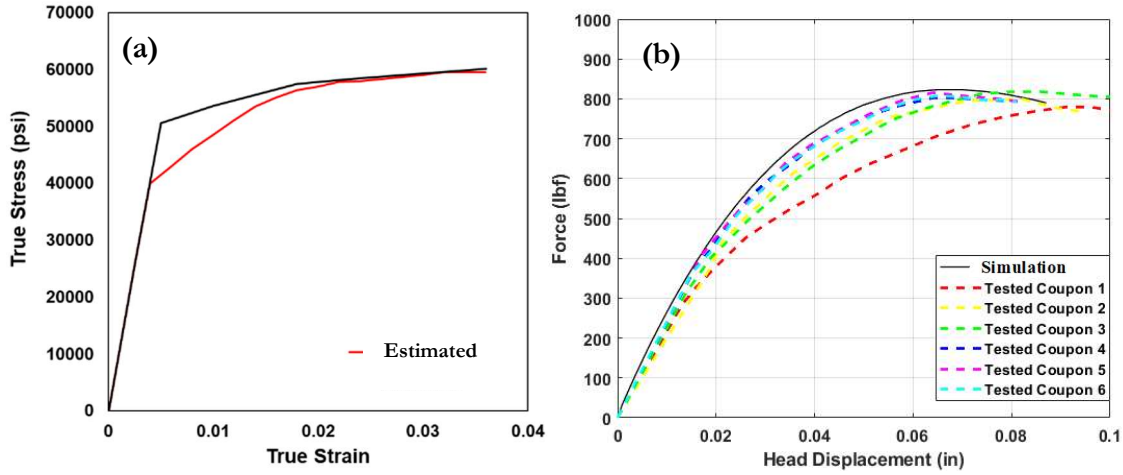

Figure 36. (a) Estimated Stress-Strain Curve (Red) for Al 5056; (b) Comparison of Predicted Load-Displacement Response with Test Data (Lyford And Andrew 2017)

5.2.2 H-Clip Fitting Coupon with Composite Skin

5.2.2.1 Model Development

The H-Clip fitting is designed to facilitate the edge-edge connection between adjacent structures or components. The FE model of the H-Clip coupon is developed as per the tested configuration, as shown in Figure 37. The bottom and the top face sheet are created with 3-ply composite skin using solid elements partitioned to represent each ply. The skin is made of M55J high modulus unidirectional fibers reinforced in CE-3 resin and consists of [+60/0/-60] stacking sequence with +60° as the outermost ply. The honeycomb core sheet used in this model has a 3.1 pcf nominal density. Note that the core material utilizes the calibrated plasticity curve for Aluminum 5056 alloy from the analysis presented in the previous subsection.

A beam element with a circular profile is introduced to simulate loads from the bolt to the coupon. The ends of the beam element are connected to the circumferential edge of the H-clip hole. A reference point is introduced and connected to the beam element using equation constraints to emulate displacement from the load head to the bolt-fastener assembly. The 0^{o} fiber direction is along the y-axis and runs perpendicular to the core ribbon direction along the x-axis. The two ends of the coupon are constrained to emulate fixed boundary conditions. Additionally, all the elements in the face sheet, fitting and adhesive have at least three elements through-thickness. This ensures higher fidelity and captures all local deformation behavior. The final model with the converged mesh comprises 238280 shell elements for the honeycomb core, eight elements for the beam element, and 265082 reduced integration solid elements for the face sheet, adhesives, and fitting geometry.

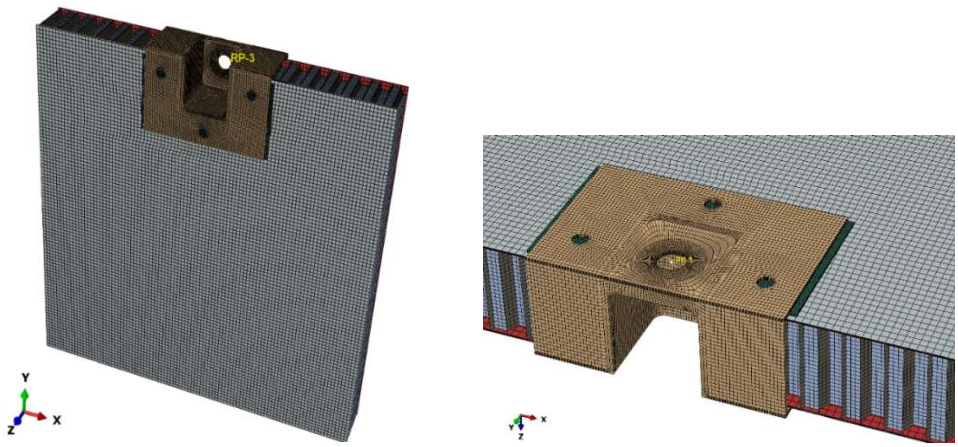

Figure 37. FE Model of Composite Sandwich Panel with Adhesively Bonded H-Clip Fitting

Hashin's failure criteria are used to evaluate the different failure modes in the composite face sheet. The criteria distinguish tensile and compressive modes of the fiber and the matrix and interact with more than one stress component to evaluate the different failure mechanisms. Since the inbuilt Hashin damage model in Abaqus is limited to plane stress

formulations, it could not be used directly in this work. In this study, the composite face sheets are modeled using solid brick elements to capture through-thickness stresses and the stresses between individual ply accurately. Therefore, a CDM-based damage model with a modified 3D Hashin type failure criteria is implemented using a user-defined material subroutine. Note that the damage model used in this study also accounts for interaction between fiber and matrix damage modes and shear using damage interaction coefficients while capturing through-thickness deformation.

The CDM model is evaluated at every integration point of the face sheet element, and the damage is homogenized and treated as degradation of the element's stiffness matrix. Four failure mode indices, d_f, d_m, d_z, d_s are used to evaluate the 3D Hashin-type failure criteria (see Table 10). The first criterion corresponds to fiber failure. The second failure corresponds to matrix-dominated failure. The third failure corresponds to transverse matrix failure (flatwise normal). The last mode corresponds to shear-dominated failures (interlaminar shear).

Table 10. Failure Modes and Failure Criteria of Composite Plies

Failure Mode		Failure criteria (Hashin criteria)
Matrix Failure	$\sigma_2 > 0$	$d_m{}^2 = \left(\sigma_2/Y_t\right)^2 + \left(\tau_{12}/S_{12}\right)^2 + \left(\tau_{23}/S_{23}\right)^2 \geq 1$
	$\sigma_2 < 0$	$d_m{}^2 = \left(\sigma_2/Y_c\right)^2 + \left(\tau_{12}/S_{12}\right)^2 + \left(\tau_{23}/S_{23}\right)^2 \geq 1$
Shear Failure	σ_{12}	$d_s{}^2 = \left(\sigma_1/X_c\right)^2 + \left(\tau_{12}/S_{12}\right)^2 + \left(\tau_{23}/S_{23}\right)^2 \geq 1$
Delamination (flatwise normal)	σ_3	$d_z{}^2 = \left(\sigma_3/Z_t\right)^2 + \left(\tau_{13}/S_{13}\right)^2 + \left(\tau_{23}/S_{23}\right)^2 \geq 1$
Fiber Failure	$\sigma_1 > 0$	$d_f{}^2 = \left(\sigma_1/X_t\right)^2 + \left(\tau_{12}/S_{12}\right)^2 + \left(\tau_{13}/S_{13}\right)^2 \geq 1$
	$\sigma_1 < 0$	$d_f{}^2 = \left(\sigma_1/X_c\right)^2 \geq 1$

Once the failure criteria are satisfied, the damage initiates, and the subsequent damage evolution is assumed to follow a linear degradation law. Element deletion is performed when the damage variable reaches the critical value of 0.9. It is important to note that the implementation of constitutive models with strain-softening behavior results in mesh-dependency. The energy dissipated due to damage in the element decreases with a decrease in the element size. Therefore, the finite element characteristic length scales are used, related to the element size in the face sheet, and the softening due to damage is expressed as a traction-separation relation (Pineda and Waas 2013; Lapczyk and Hurtado 2007). The use of characteristic length scales and traction-separation relation ensures that the energy released during the damage process is per unit area, not per unit volume. This approach mitigates the dependence of the predicted softening response on the mesh density (Pineda and Waas 2013; Lapczyk and Hurtado 2007; Jirasek 1995). Matzenmiller et al. (1995) show that the evolution of damage in the constitutive material is related to fracture toughness and characteristic length. A modified form of their evolution equation is used to determine the temporal evolution of the continuum damage variable for the four different failure modes:

$$d_1 = 1 - \left\{1 + \left(\frac{d_f - 1}{1 - \frac{l_e X \epsilon_{11c}\left(d_f - 1\right)}{2G_f}}\right)\right\}^{-1} \tag{5.1}$$

$$d_2 = 1 - \left\{1 + \left(\frac{d_m - 1}{1 - \frac{l_e Y \epsilon_{22c}\left(d_m - 1\right)}{2G_m}}\right)\right\}^{-1} \tag{5.2}$$

$$d_3 = 1 - \left\{1 + \left(\frac{d_z - 1}{1 - \frac{l_e Z \epsilon_{33c}\left(d_z - 1\right)}{2G_m}}\right)\right\}^{-1} \tag{5.3}$$

$$d_{12} = 1 - \left\{1 + \left(\frac{(d_s - 1)/2}{1 - \frac{l_e S \epsilon_{shc} (d_s - 1)}{4G_{II}}}\right)\right\}^{-1} \tag{5.4}$$

where X, Y, Z, S and $\epsilon_{11c}, \epsilon_{22c}, \epsilon_{33c}, \epsilon_{shc}$ are the tensile or compressive strengths and their corresponding critical strains in the fiber, matrix, flatwise normal and shear direction, respectively. The finite element characteristic length is denoted by l_e. G_X, G_Y and G_Z are fracture toughness in the fiber, matrix, and flatwise normal direction and are different for tension and compression failure. G_{II} is the Mode II critical energy release rate for the in-plane shear failure. Since the fiber and matrix damage modes can also affect the shear stiffness reduction, the in-plane and out-of-plane shear damage variables d_i *(i=4,5,6)* are expressed as the following phenomenological equations

$$d_4 = \left(1 - (1 - \eta d_1)(1 - \beta d_2)(1 - d_{12})\right) \tag{5.5}$$

$$d_5 = \left(1 - (1 - \beta d_2)(1 - \beta d_3)\right) \tag{5.6}$$

$$d_6 = \left(1 - (1 - \eta d_1)(1 - \beta d_3)\right) \tag{5.7}$$

where η and β are regarded as interaction factors to account for the effect of the fiber and matrix damage on the degradation of the damaged shear stiffnesses.

The elastic and strength properties are obtained from previous investigations and manufacturer data sheets (Stoumbos et al. 2014). However, the availability of the desired fracture toughness properties for M55J/CE-3 is extremely limited in the published literature. The matrix fracture toughness of IM7/977-3 (Iarve et al. 2015) is used to predict flatwise interply delamination (G_Z). Additionally, the fiber fracture toughness properties of IM7/8552, another carbon fiber reinforced system, are used as initial values in the present study (Pinho

et al. 2006; Miami et al. 2007). The mode I matrix fracture toughness, the mode II critical energy release rates, and the shear damage mode interaction factors are additional parameters estimated to better correlate the predicted H-Clip coupon's nonlinear response with experimental data. Preliminary analysis and sensitivity studies of the H-Clip fitting coupon revealed the primary and secondary failure mechanisms under both pull-off and shear loading conditions. The final drop in the load-displacement curve occurs due to compressive matrix cracking for the pull-off load tests. The compressive matrix fracture toughness (G_{YC}) was estimated to match the predicted ultimate failure load with the experimental data. In the case of shear loading, the final coupon failure is dominated by tensile matrix cracking. The tensile matrix fracture toughness (G_{XC}) was calibrated to match the predicted ultimate failure load with experiments. The in-plane shear damage was responsible for the initial deviation of the predicted load-displacement response from the linear elastic regime. Therefore, the mode II critical energy release rate (G_{II}) and the two damage interaction parameters are further adjusted to improve prediction accuracy. Note that the shear mode interaction factors of the fiber (η) and matrix damage (β) are assumed to be the same in this study. The summary of material constants used in the developed constitutive model for the M55J/CE-3 face sheet is shown in Table 11.

Table 11. Material Properties Used for M55J/CE-3 Unidirectional Composite Lamina

Elastic Properties		
E_{11}	40	Msi
E_{22}	0.804	Msi
E_{33}	0.804	Msi
G_{12}	0.610	Msi
G_{23}	0.160	Msi
G_{13}	0.610	Msi
ν_{12}	0.271	
ν_{23}	0.271	
ν_{13}	0.271	

Strength Properties		
X_T	280	ksi
X_C	-112	ksi
Y_T	3.4	ksi
Y_C	-23.9	ksi
Z_T	2.2	ksi
Z_C	-2.2	ksi
S_T	4.2	ksi
S_C	-4.2	ksi

Fracture Properties		
G_{XT}^*	607	lbf/in
G_{XC}^*	868	lbf/in
$G_{YT}^‡$	1.5	lbf/in
$G_{YC}^‡$	48	lbf/in
$G_Z^†$	1.5	lbf/in
$G_{II}^‡$	2.2	lbf/in
$\eta^‡$	0.3	
$\beta^‡$	0.3	

† IM7/977-3 properties (Iarve et al. 2015)
* IM7/8552 properties (Pinho et al. 2006; Miami et al. 2007)
‡ Estimated

The experimental results for the H-Clip fitting coupon were obtained from a previous investigation (Stoumbos et al. 2014). The coupon tests were performed using an Instron universal test machine at the Northrop Grumman facility. The panel was supported by a fixture providing attachment and loading to the H-Clip along the nominal centerline of the test coupon. The coupon was secured to a pair of aluminum reaction plates that sandwiched the coupon and reacted to the applied load. The test consisted of pulling the H-Clip in shear (+x axis) and pull-off (+y axis) directions until past their ultimate load capacity. For each test case, the coupon was secured to T-slot plates providing lateral adjustment to align the H-Clip fixture over the load head. Each coupon was manually aligned to minimize binding at the rod end and clevis interface that would have caused premature failure of the coupon. The machine head displacement rate was 0.025 inches/min, and the tests were performed at room temperature. The deflection at the head of the tensometer was measured, and the applied load, with several coupons for each load case, was tested to ensure test reliability and failure mode consistency. It is also worth mentioning that only the coupon test results that set the upper and lower limit of the obtained stiffness and ultimate failure load are used for model validation, as shown in Figures 38 and 41.

5.2.2.2 Analysis and Discussion

First, the base model is simulated to assess the stiffness of the coupon in the linear elastic regime and match with experimental results. The model initially overestimated the coupon stiffness under shear (x-axis) and pull-off (y-axis) loading conditions. It is important to note that the displacement from the actual test data was measured at the head of the tensometer and not at the coupon itself. This could mean that the deflection of the load-fixture, which was relatively long in the shear and pull-off load tests, was not accounted for in the base model. Hence, a compliance loss factor is introduced in the form of equation constraints to adjust the transfer of displacement from the load head to the bolt-fastener assembly. Consequently, a 30 % loss in compliance is identified to better match the predicted model stiffness with that of the experiments in both shear and pull-off directions. On the other hand, the predicted coupon stiffness along the z-direction (normal) was in good agreement with the experiments with no compliance loss.

Figure 38 shows the comparison between the predicted and experimental load-displacement curves under shear (x-axis) loading conditions. The model prediction using the assumed fracture toughness values compares well with the experimental results. The progression of failure events is also labeled along the simulated load-displacement curve. The leading failure events and their corresponding damage contours in the outermost ply are shown in Figure 39. The contours shown under the corresponding failure modes have different upper and lower bounds for the damage variable. Hence, the subplots merely present the predicted hot-spots and propagation paths and not be wholly relied on to compare damage intensities under different failure modes. The initial deviation from the linear response (at point A) occurs due to compressive fiber failure in the outermost ply. Also, the fiber failure

interacts with the in-plane shear mode, and damage localizes near the fitting edges. The degradation of the fiber and in-plane shear modulus of the outer ply (+60 °) increases the middle ply's compressive stresses (0°). Beyond point C, compressive matrix cracking initiates in the 0° ply near the fitting region and degrades that layer's transverse stiffness. The drop in the load-displacement response before point D indicates face sheet failure without being able to carry the additional load. Beyond point D, the load gets transferred to the core, and a core tensile/compressive failure in the shear direction would cause the load-displacement curve to either saturate or drop beyond point E. The predicted final failure pattern near the fitting edge also compares well with the failed test coupon, as shown in Figure 40.

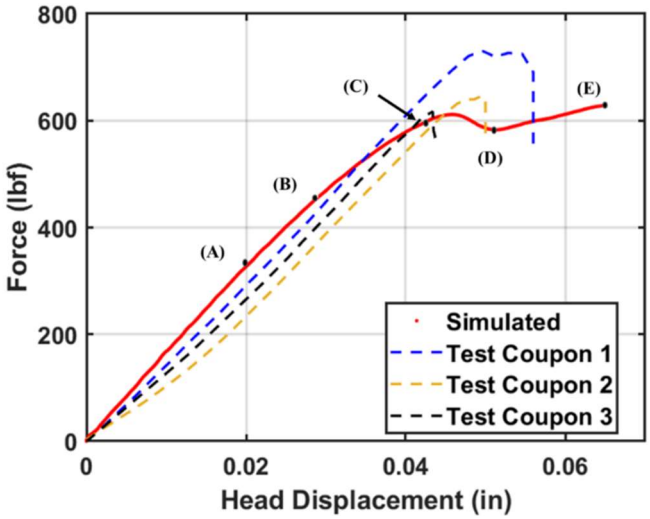

Figure 38. Comparison of Predicted Response and Test Results Under Shear Loading

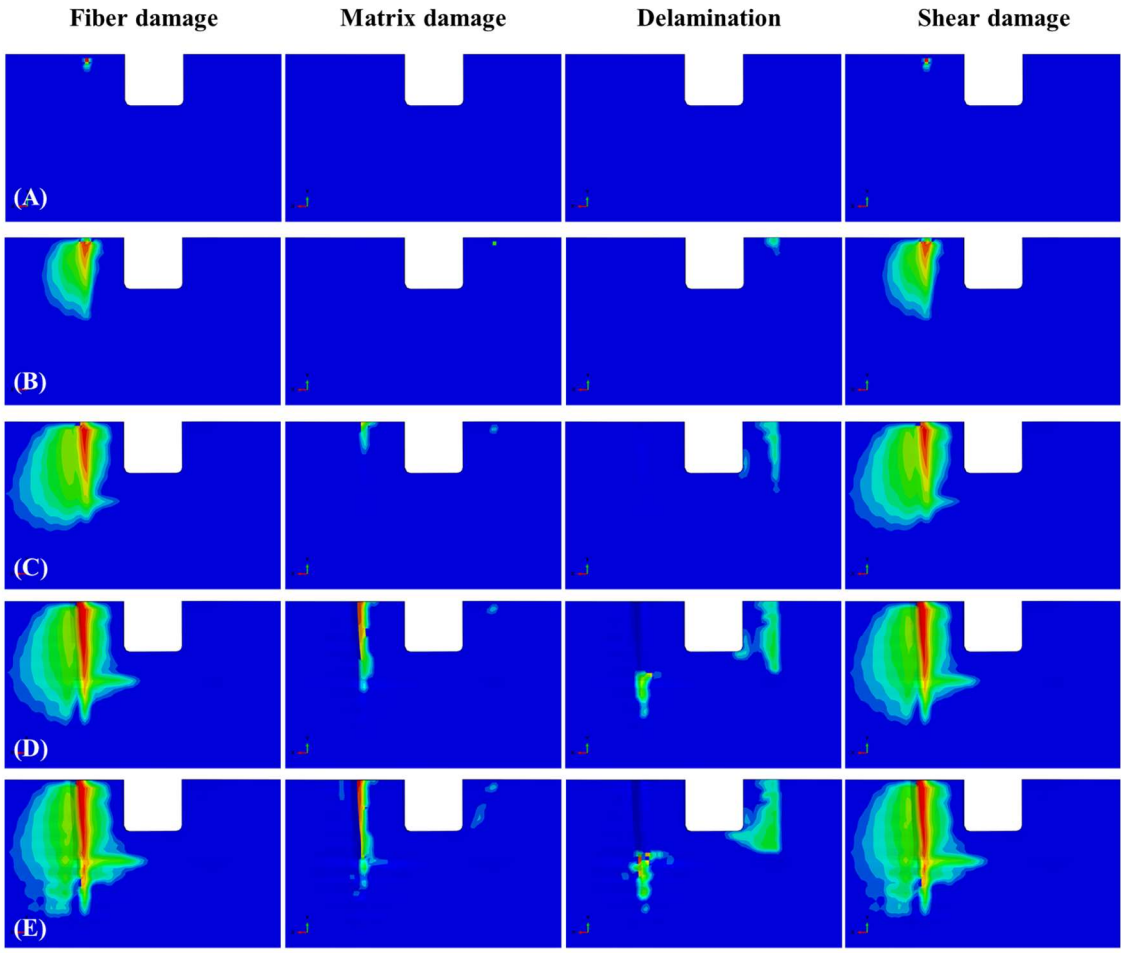

Figure 39. Progressive Failure in Outermost Composite Ply (+60 ^{O}) Under Shear Loading

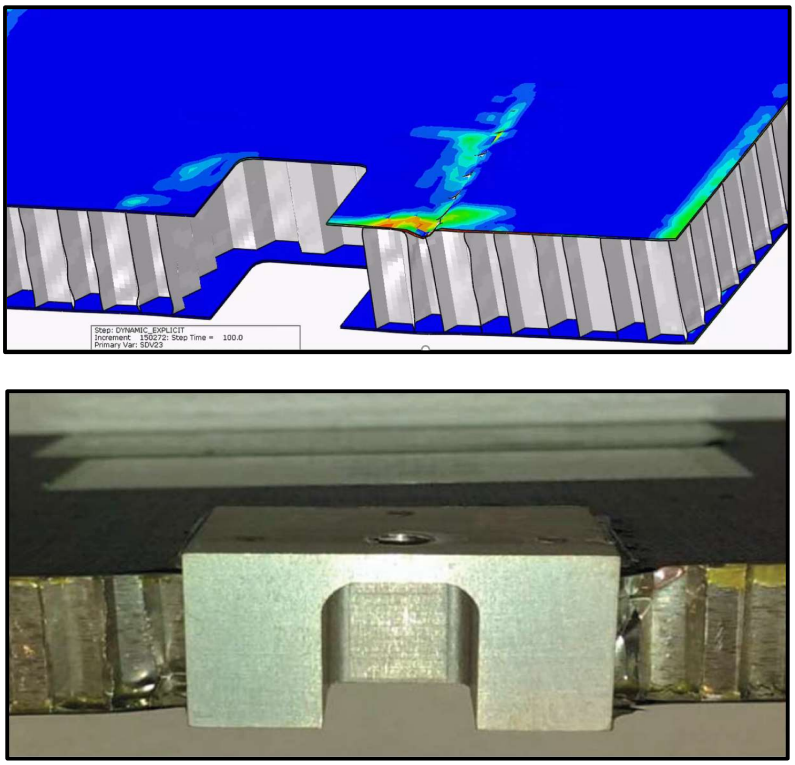

Figure 40. Comparison of Predicted Failure Pattern and Failed Test Coupon

Likewise, along the pull-off (y-axis) direction, the analysis predicts face sheet rupture near the fitting region due to tensile matrix cracking in the $+60^{o}$ outermost ply. Figure 41 shows the comparison between the predicted and experimental load-displacement curves and labels the progression of failure events under pull-off loading conditions. The simulated load-displacement response using the estimated fracture toughness values matches well with the experimental results. Figure 42 shows the corresponding damage contours in the outermost ply. The initial deviation from the linear elastic regime occurs due to a combination of tensile matrix cracking, delamination, and in-plane shear failure in the outermost ply with tensile matrix cracking as the dominant mechanism. As damage propagates, the drop in the curve beyond point C indicates complete face sheet rupture due to matrix tensile cracking and delamination.

Moreover, face sheet rupture causes highly localized shear stresses in the honeycomb core, revealing possible hotspots for core rupture, as shown in Figure 43. It is also worth mentioning that the predicted failure pattern agreed well with the experimental observations. The developed damage model with the estimated material constants and the honeycomb core elasto-plastic response will be incorporated in analyzing a spacecraft's thrust tube sandwich structure discussed in the following subsection.

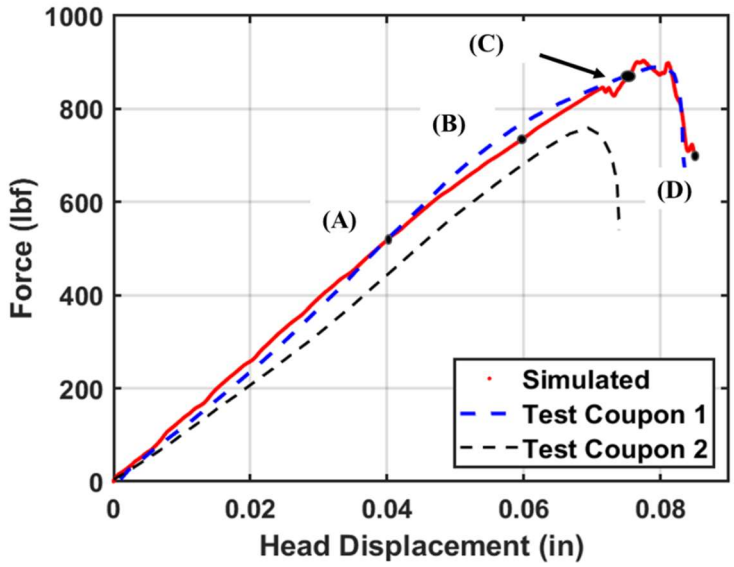

Figure 41. Comparison of Predicted Response and Test Results For Pull-Off Loading

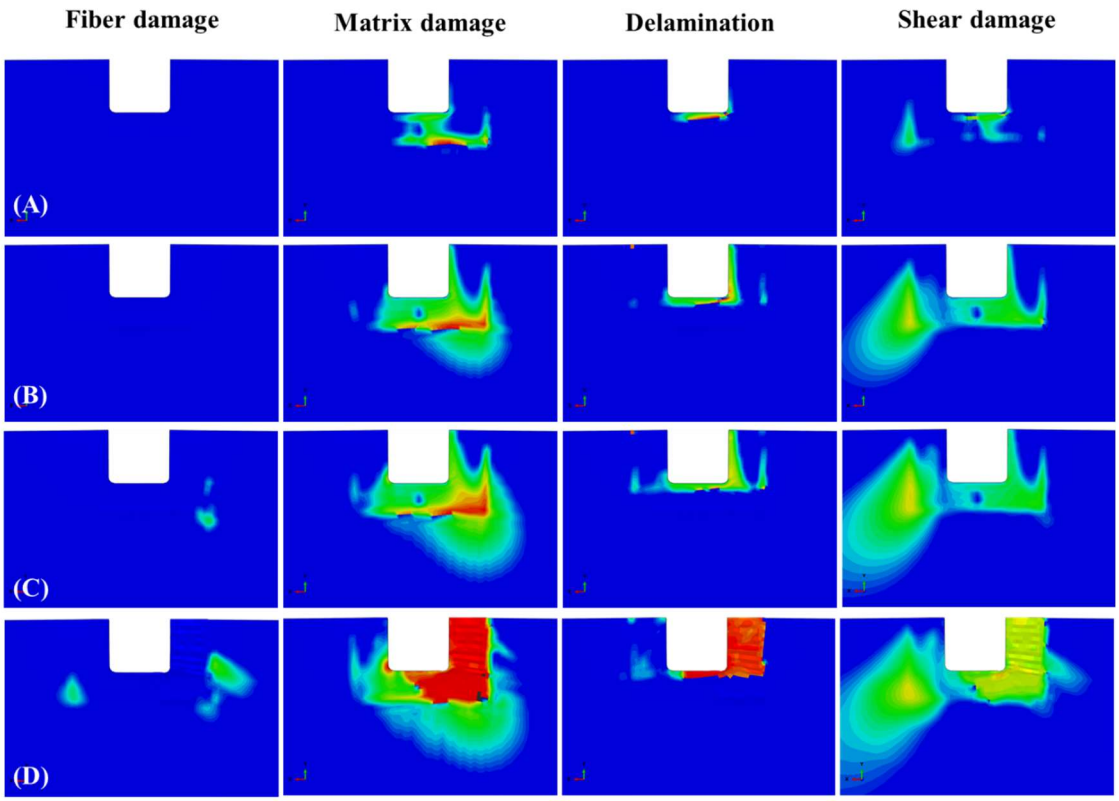

Figure 42. Progressive Failure in Outermost Composite Ply ($+60^{O}$) Under Pull-Off Loading

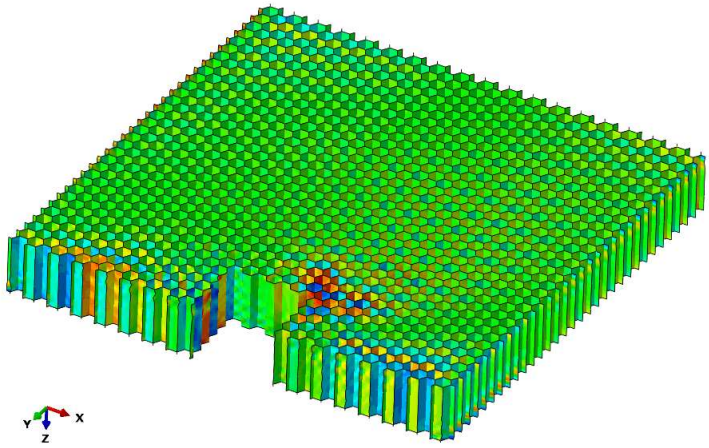

Figure 43. Shear Stresses in Honeycomb Core Under Pull-Off (Y-Axis) Loading

5.2.3 Sandwich Panel under Thermal Cyclic Loading

5.2.3.1 Model Setup

Earlier in the design phase, the composite materials used in spacecraft sandwich structures must appropriately account for the predicted in-orbit temperatures specific to that space mission. Recently, a space launch vehicle with an all-composite thrust tube containing several configurations of bonded metallic fittings was built at the Northrop Grumman facility. During the design verification phase, multiple anomalies and instances of visual fiber damage and cracked bonds were identified in the thrust tube post several cycles of thermal loading. Figure 44 shows a typical example of visual fiber damage at a cup-fitting location. Various test coupons of the sandwich structure with different configurations of bonded fittings were further developed and subjected to thermal cycling as part of the internal research and development. The present modeling effort aims to assess potential modes of failure and damage hot spots in such test coupons with a cup bonded fitting using the estimated nonlinear material properties and the established modeling strategies from the previous investigations.

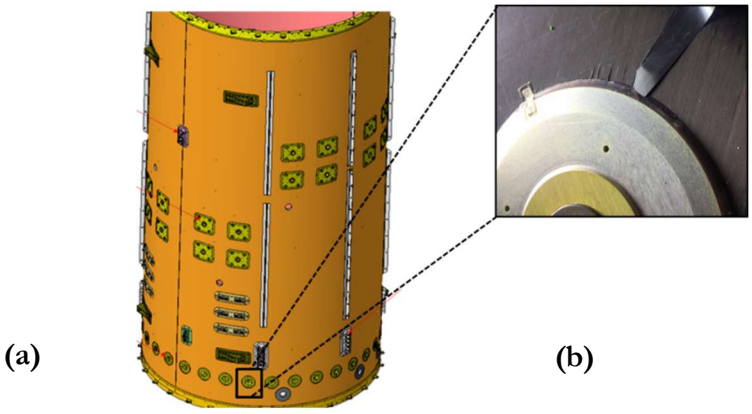

Figure 44. (a) Schematic of Spacecraft Thrust Tube with Bonded Fittings; (b) Thrust Tube Failure Near Fitting Post Thermal Cycling

The thrust tube fitting test coupon is modeled as a flat section of dimensions 10" x 10" x 0.5". The coupon model consists of Al 5056 honeycomb core with 6.1 pcf nominal density, 22-ply composite skins made of M55J/CE-3, EA.9309.NA adhesives, Al 7075-T73 washers, and Ti-6Al-4V cup fitting. The face sheet consists of [-45/0/0/0/+45/0/0/0/-45/0/0/0/+45/0/0/0/-45/0/0/0/0/+45] stacking sequence with -45° as the outermost ply. The 0° fiber direction is along the y-axis and runs perpendicular to the core ribbon direction along the x-axis. The detailed model of the test coupon is depicted in Figure 45 (a). The adhesive layer is modeled between the washer and face sheets on both the inner and outer sides of the thrust tube. Additional adhesive elements are modeled between the cup and the outer washer.

The face sheet, fitting, adhesives, and washers are modeled as perfectly bonded with common nodes between them to achieve a stable transfer of thermal loads at the interfaces. These components are meshed using solid brick elements with reduced integration points. The critical regions around the bonded cup fitting and the free edge interface used a more refined mesh relative to the strain gradients near the insert hole on the face sheet and core. Some relatively poorly formed elements in the face sheet were caused by having to mesh a circular cup fitting through the panel insert with a washer bonded to the face sheet while maintaining a structured mesh. Such regions were carefully partitioned to ensure the uniform transition of mesh and improve element aspect ratios. The honeycomb core is meshed separately using reduced-integration shell elements and discretized sufficiently to prevent excessive negative element volumes or other excessive distortion from occurring under high compressive and shear loads. The refined FE model resulted in approximately 727831 shell elements generated for the honeycomb core and 558152 solid elements for the face sheet, adhesives, washer, and fitting. The honeycomb core and the face sheets are connected using

node-surface TIE constraints. The node-surface-based constraint prevents each node on the honeycomb core element from punching inward and penetrating the face sheet. An enhanced viscous-based hourglass control was used to suppress energy modes that could trigger excessive distortion of solid elements with reduced integration points. Mass scaling was also used to achieve a stable time increment and prevent excessive incremental rotation of elements undergoing large deformation.

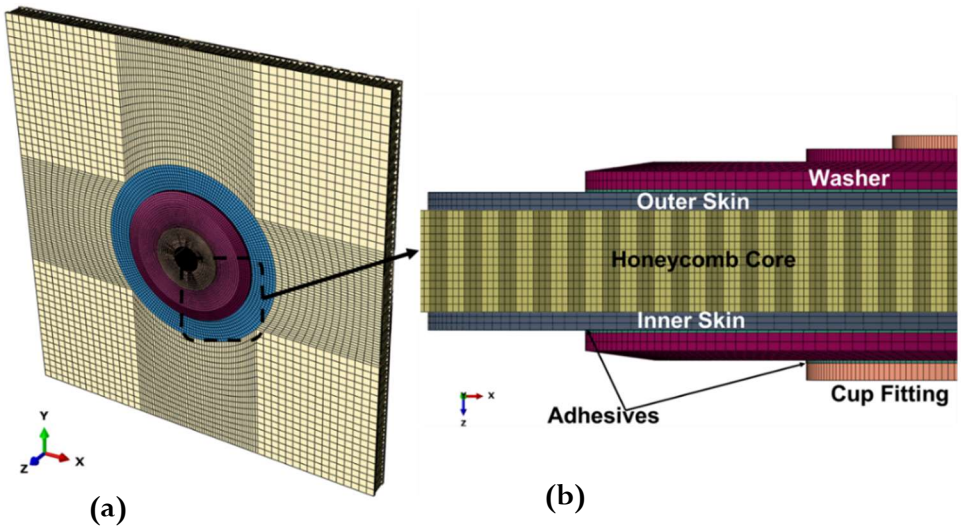

Figure 45. (a) Full Model Assembly; (b) Closer Look of Mesh Connectivity

The developed model includes the estimated elasto-plastic response for the honeycomb core and temperature-dependent CTE values obtained from the manufacturer datasheet. The temperature-dependent properties for the composite skin are obtained from another investigation (Stoumbos et al. 2014) (see Table 12). They are used as input in the developed user-defined material subroutine. This temperature dependence is described assuming a linear interpolation using the set of values from Table 12 for each material property at different temperatures. The subroutine internally computes the thermal strains and utilizes mechanical strains for the local stress analysis and subsequent evaluation of the developed damage model.

The temperature-dependent adhesive properties are obtained from the manufacturer (see Table 13) and are input in the form of Abaqus tabulated values. The material response for titanium cup fitting is assumed to be linear elastic, whose properties are also obtained from the published literature (Lampman and Zore 1990).

Table 12. Temperature-Dependent Material Properties of M55J/CE-3 0° Ply

	-37°C	22°C	63°C	
E_{11}	40.5	40	39.7	Msi
E_{22}	0.875	0.804	0.765	Msi
E_{33}	0.875	0.804	0.765	Msi
G_{12}	0.6665	0.610	0.579	Msi
G_{23}	0.1843	0.160	0.143	Msi
G_{13}	0.6665	0.610	0.579	Msi
v_{12}	0.2795	0.271	0.2778	
v_{23}	0.2838	0.271	0.2779	
v_{13}	0.279	0.271	0.2778	
α_{11}	-1.12	-1.08	-1.05	10^{-6}/°C
α_{22}	2.93	3.17	3.37	10^{-5}/°C
α_{33}	2.93	3.17	3.37	10^{-5}/°C

Table 13. Temperature-Dependent Material Properties of EA.9309.NA Adhesive

	-37°C	-19°C	22°C	63°C	
E	0.4884	0.4669	0.418	0.240	Msi
v	0.33	0.35	0.4	0.25	
α	6.57	6.91	9.4	8.46	10^{-5}/°C

Boundary conditions are applied to the coupon model as per test configurations. The nodes on the left end are constrained in the x-direction, while the top surface is constrained in the y-direction (see Figure 46). The other two ends are free to expand uniformly along the circumferential x-y plane. A kinematic coupling constraint is applied between a centroid node and node sets on the components corresponding to the free end of the coupon. Figure 47 illustrates individual centroid nodes on the face sheet and core (denoted by red), each

connected to their respective node sets (denoted by the yellow lines). The coupon model is exposed to pre-defined temperature field boundary conditions, which involve one complete temperature cycle from ambient to +63°C and then to –50°C. A stable mass scaling was used in the dynamic/explicit solver to decrease the solution time by increasing the minimum stable time increment to 1.0e-05 throughout the thermal load cycle.

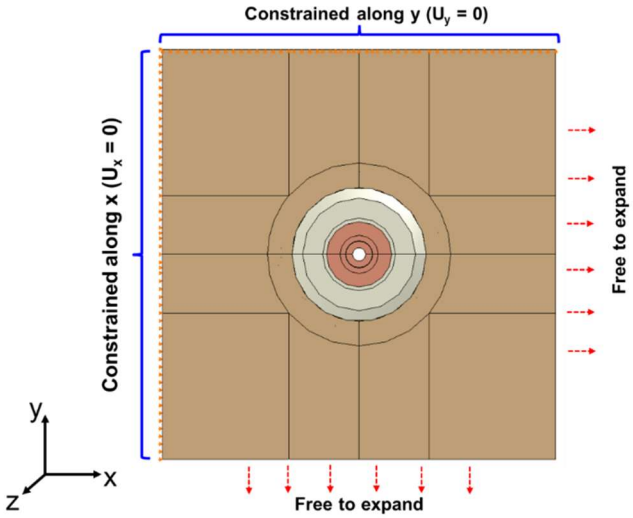

Figure 46. Displacement Boundary Conditions

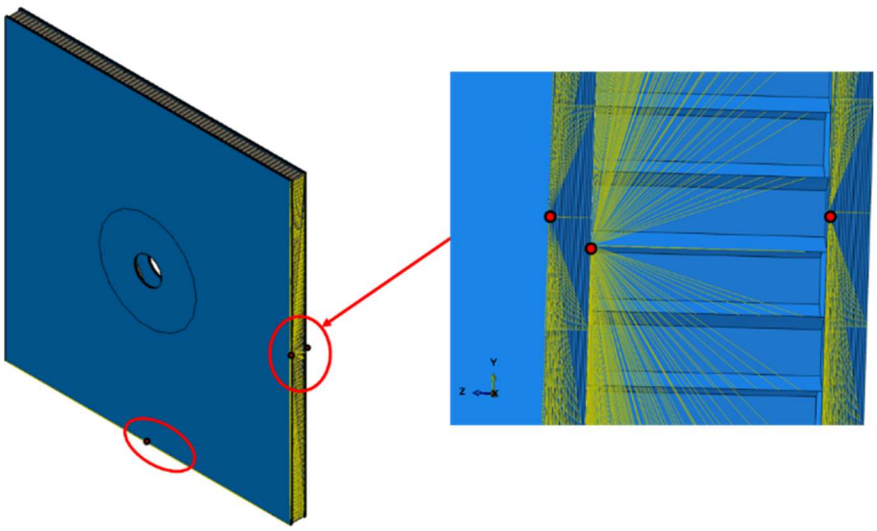

Figure 47. Kinematic Coupling Constraints on Free Ends for Uniform Expansion

5.3 Analysis and Discussion

First, the analysis is performed to investigate damage initiation and propagation in the composite face sheets. Figure 48 shows the progressive failure event in the outer ply of the face sheet on the outer side of the coupon (along +z) over different stages of cyclic thermal loading. Note that the figure does not illustrate the entire geometry but only the region near the fitting, which is of interest in correlation with experiments. During the hot conditioning part of the cycle, there are no signs of damage in the face sheet. However, at –5°C, damage initiates in the outer ply near the free edge boundary of the fitting due to delamination and in-plane shear. The failure initiation in the face sheet is attributed to the significant mismatch in CTE values, resulting in high thermal strains in the skin near the fitting boundary. At – 30°C, damage initiates near the fitting hole region due to delamination and shear. As the load cycle approaches – 40°C, damage begins to initiate near the fitting hole due to compressive fiber failure. Beyond – 40°C, the fiber damage grows in magnitude and propagates towards the free edge of the fitting. As a result, the shear damage near the hole coalesces with damage near the free edge of the fitting. Figure 49 illustrates the progressive failure events in the outermost face sheet on the inner side of the coupon (along -z). Likewise, the failure pattern is like the coupon's outer side (along +z) and is dominated by delamination and in-plane shear.

It is important to note that element deletion was unnecessary since the damage variables did not reach their corresponding threshold values. Further application of thermal cycles may increase the damage to its threshold value and trigger element deletion to investigate the post-failure response. Nevertheless, the analysis identified delamination and in-plane shear as potential failure modes that could lead to complete coupon failure. It is worth mentioning that the predicted damage initiation hot spot near the free edge boundary of the fitting correlates

well with the experimental observations. Additional investigations on the nonlinear response of honeycomb core and adhesives are carried out to better understand the underlying mechanisms, potential root causes, and damage precursors.

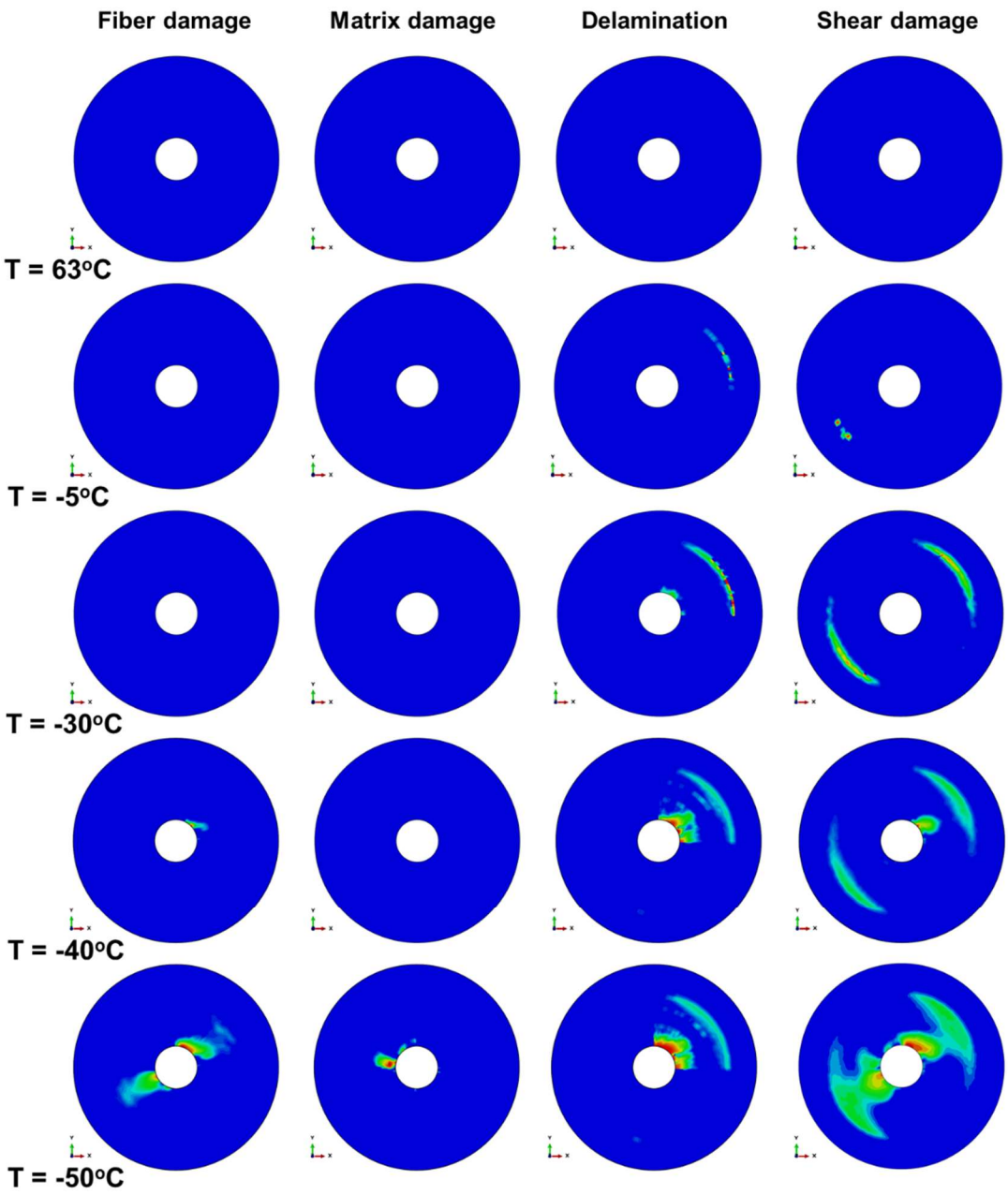

Figure 48. Damage Evolution in Outermost Ply (Along +Z) At Different Temperatures

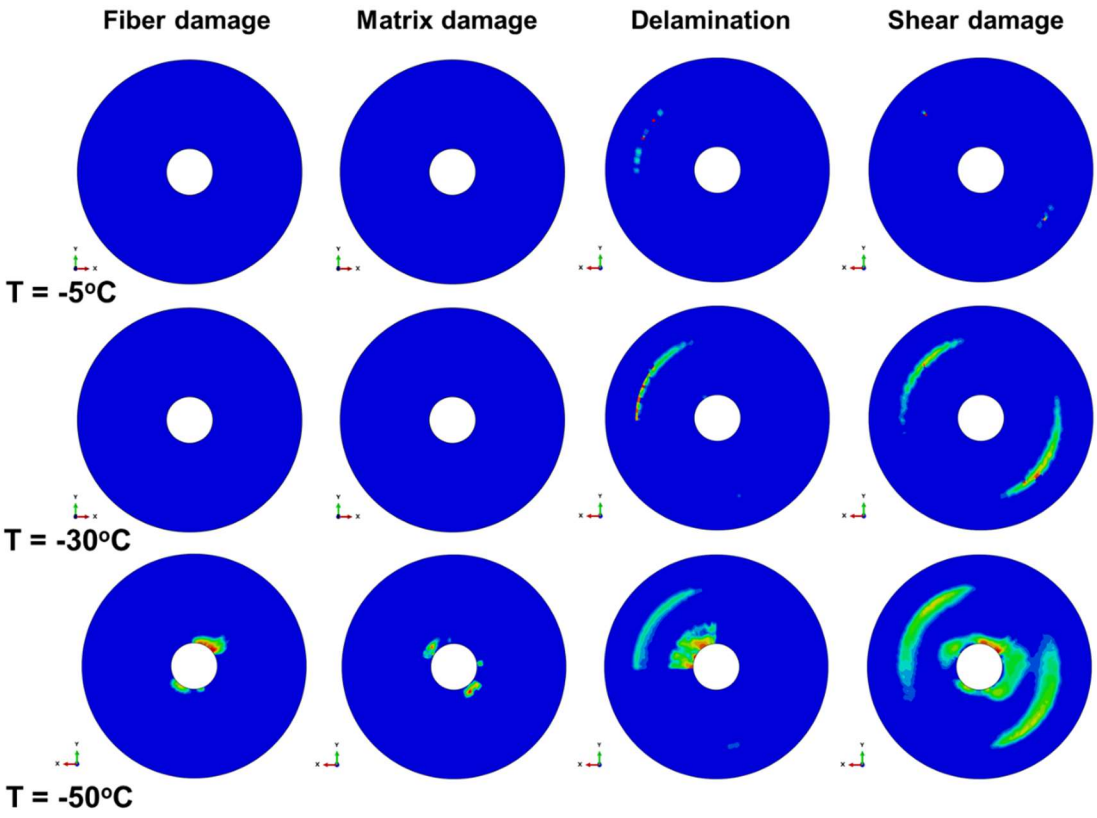

Figure 49. Damage Evolution in Outermost Ply (Along -Z) At Subzero Temperatures

The plastic deformation in the honeycomb core is another important phenomenon affecting the damage initiation and propagation in the composite face sheet. The variation of the honeycomb core's plastic dissipation energy is computed and plotted against the fluctuating temperature values, as shown in Figure 50. Points A to B corresponds to the hot conditioning, while beyond C corresponds to the cold conditioning part of the cycle. The plastic dissipation energy increases significantly up to point A, which is about 40°C, followed by saturation and a relatively less significant spike in energy as the temperature reaches 63°C. However, the dissipation energy remains saturated during most of the cold conditioning part of the cycle except when the temperature approaches –50°C (point D). The saturated

dissipation energy indicates the negligible effect of the honeycomb core on the microcrack formation in the face sheet during the cold conditioning part of the cycle.

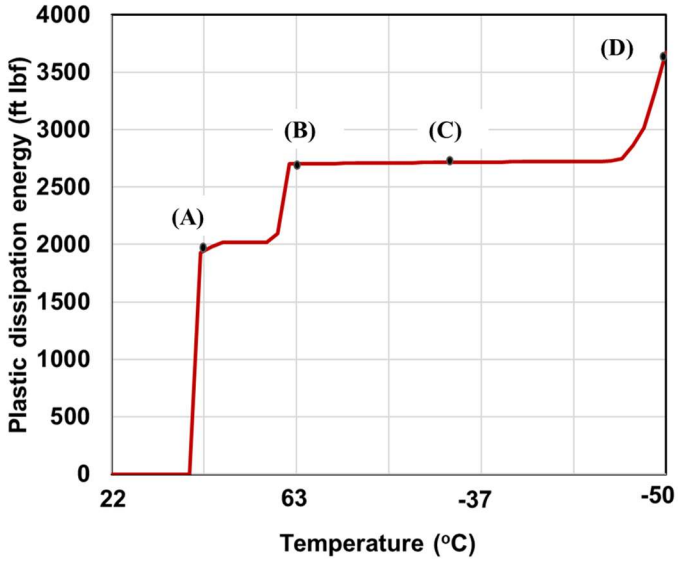

Figure 50. Plastic Dissipation in Core at Different Temperature Stages

Figures 51 (a) and (b) show the von-mises stresses in the honeycomb core near the fitting region at 63°C (point B) and −50°C (point D). There is a significant increase in local stress concentrations in the cell walls of the honeycomb core adjacent to the face sheet, which could indicate potential sites for delamination due to composite face sheet-core debonding. Besides, further thermal cycles could lead to higher stresses at the interface between the face sheet and core. Nevertheless, in the present study, the face sheet-core interface is modeled using perfect bonding conditions and does not account for debonding.

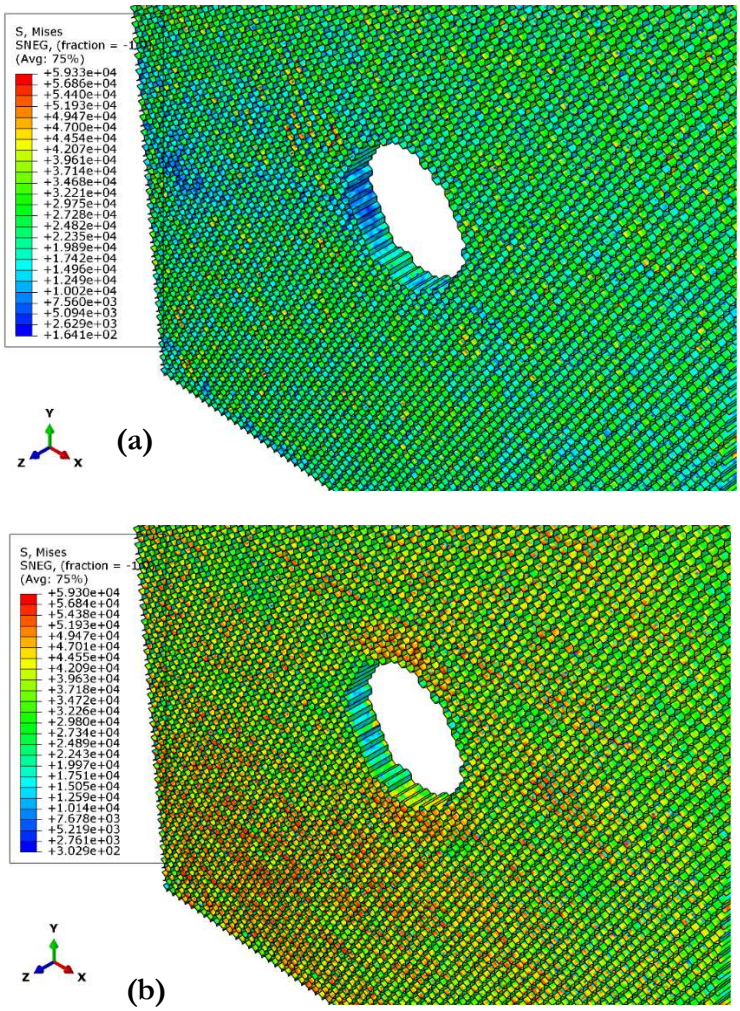

Figure 51. Von-Mises Stresses in Honeycomb Core at: (a) 63°C and (b) -50°C

Similarly, the deformation behavior of the adhesive layers is investigated. Figure 52 shows the variation of plastic dissipation energy in the adhesive layer between the washer and outermost composite skin at different temperatures. The deformation of the adhesive layer remains in the linear elastic regime during the hot conditioning part of the cycle. However, as the temperature approaches –5°C, the adhesive layer enters the plastic regime, and the dissipation energy continues to increase until –50°C rapidly. The initiation point also correlates well with the fact that face sheet microcracks initiate near the free edge beyond – 5°C. Figure 53 shows the equivalent plastic strain in the adhesive layer between outer skin and washer at

–37 C and – 50 C thermal cycle temperature. A closer look at the elements shows high concentrations of equivalent plastic strain at the adhesive bond line layer boundary. This suggests the adhesives' significant contribution to the damage initiation and evolution in the composite face sheet and bond line cracking at the free edge of the fitting as potential damage precursor.

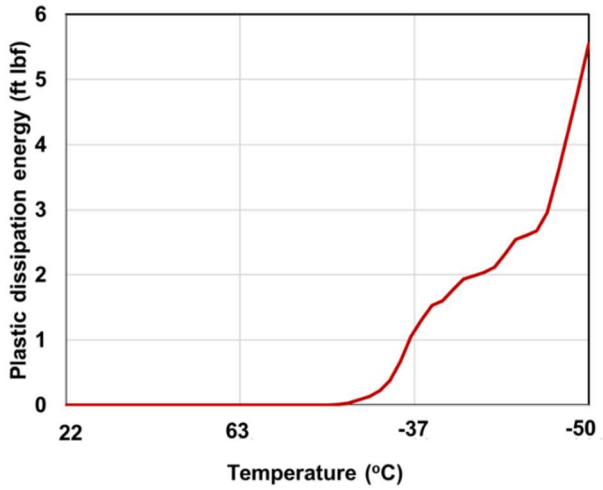

Figure 52. Plastic Dissipation in Adhesive Layer At Different Temperature Stages

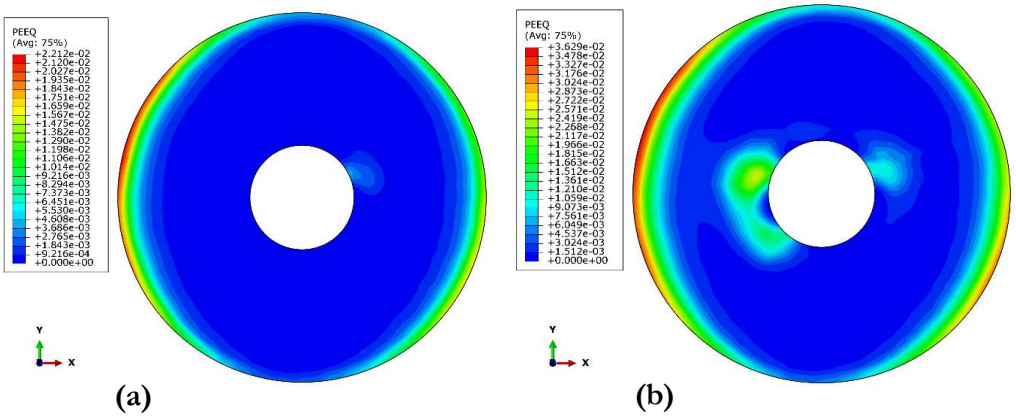

Figure 53. Equivalent Plastic Strain in Adhesive Layer at; (a) -37°C and (b) -50°C

5.4 Summary

A high-fidelity modeling methodology to investigate the thermomechanical performance of complex sandwich space structures was developed. Detailed finite element analyses were performed to investigate failure mechanisms in sandwich panel coupons with a specific aluminum honeycomb core and carbon-epoxy composite face sheet. The cellular honeycomb core sheet, composite laminate face sheet, metallic fittings, and adhesives were explicitly modeled to precisely capture the load transfer behavior and geometrical nonlinearities. Sandwich panel coupon subject to flatwise tension loading was used to investigate the honeycomb core's local and global buckling response, which is primarily dominated by the plastic deformation of the aluminum core material. The plastic deformation of bonded adhesives had a notable effect on the pre-peak nonlinear response. Panels with H-Clip fitting were then chosen to investigate the progressive damage response in the composite face sheet under different loading conditions. The material property degradation and associated failure modes were captured using a CDM-based failure model. The necessary material constants for the damage model were numerically estimated to match the predicted load-displacement response with that of experiments. The developed model captured localized damage initiation and propagation under different failure modes associated with face sheet compression, rupture, and delamination.

The estimated material constants and modeling strategies were incorporated in the subsequent analysis of a spacecraft's thrust tube sandwich coupon with bonded metallic fittings subjected to cyclic thermal loading. The developed model of the coupon predicted failure in the outer and innermost face sheets near the boundary of the fitting region. The analysis identified delamination and in-plane shear failure as dominant failure modes with

additional modes such as compressive fiber and tensile matrix cracking. The underlying root cause was attributed to the mismatch in CTE values that results in high thermal gradients at the bonded fitting interface during the cold conditioning part of the cyclic thermal loading. The adhesives along the free edge of the fitting region plastically deformed, indicating potential bond line cracking before the formation of microcracks in the composite face sheet. Also, the honeycomb core indicated possible hot spots for delamination due to face sheet-core debonding. However, the plastic deformation of the core sheet had a negligible effect on the microcrack formation in the composite face sheet. The identified failure and damage modes of the specific thrust tube sandwich coupon with a cup bonded fitting correlated well with the experimentally observed response. The methodology for the analysis of sandwich structures presented in this paper can be extended to investigate the qualitative performance of thrust tube coupons with other bonded joints and fittings configurations. Future work will include incorporating additional temperature-dependent material properties for the specific composite and adhesives obtained from detailed experimental characterization and testing to improve prediction accuracy.

CHAPTER 6

CONTRIBUTIONS AND FUTURE WORK

6.1 Contributions

The research work presented in this dissertation was primarily motivated by the lack of efficient techniques to bridge atomistic scale information with microscale and higher length scales for the analysis of complex nanoengineered composite material systems such as radially grown CNT architecture. To address this gap in literature, physics-based models and atomistically-informed efficient multiscale analysis framework were developed in this work for the linear and nonlinear analysis of nanoengineered composite materials. Summarizing the significant contributions of this work, the following achievements are noted:

- Developed an atomistically-informed high-fidelity microscale model for CFRP composites with radially-grown CNT architecture that utilized nanoscale-derived elastic and inelastic information and variation in the architectural parameters to efficiently estimate the nanocomposite properties at higher length scales.
- Developed a thermodynamically admissible constitutive model to efficiently transfer inelastic dual stress-softening behavior from discrete atomistic MD simulations of radially-grown CNT interphase region to higher length scales using a continuum damage mechanics approach.
- Investigated the linear and nonlinear effects of the unidirectional CFRP composites with radially-grown CNT architecture under mechanical loading, using the developed atomistically informed damage model.

- Investigated the effects of damage initiation and propagation with and without the presence of radially-grown CNTs and correlated subscale stress distribution and damage localization to the out-of-plane global mechanical response.
- Developed a reduced-order approximation of the high-fidelity microscale model to reduce the computational cost and memory requirements of repeated micromechanics simulations and efficiently transfer the homogenized microstructural response to higher length scales. Demonstrated improved computational time and memory by an order of 100 and 8, respectively.

Following are the secondary contributions from the research work presented in this dissertation:

- Investigated failure mechanisms and captured the intrinsic nonlinear material behavior of specific aerospace-grade aluminum honeycomb core and CFRP composite face sheets.
- Investigated the thermomechanical performance of complex honeycomb core composite sandwich space structures with adhesively bonded fittings exposed to extreme temperature ranges using high-fidelity FE modeling techniques.
- Demonstrated the use of a computational methodology for consistent analysis of mechanical and thermal strength degradation in complex sandwich composite structures.

With these achievements, the research presented in this dissertation will lead to an improved understanding of the load transfer characteristics, damage precursors, and failure mechanisms in complex nanoengineered composites and composite sandwich structures, which can be utilized to tailor their performance. The developed ROM will also be beneficial

to predict the global and local response of composites in general with significantly improved computational efficiency.

6.2 Future Work

Although this research work presents techniques for atomistically-informed multiscale modeling of complex nanoengineered composites, several gaps can be further addressed to further improve the current understanding of scale-specific damage initiation and propagation mechanisms in these material systems. For instance, the atomistically-informed interphase model developed in Chapter 2 does not account for the effect of CNT areal density on the interphase modulus along the CNT growth direction. Additional analysis at the nanoscale should be carried out to further improve the accuracy of the predicted properties while accounting for variation in moduli of the interphase material in all three directions. Moreover, it is essential to consider other competing damage mechanisms occurring at the nanoscale, such as CNT breakage, neglected in the current modeling effort. Nevertheless, the developed framework provides a strong foundation for future improvements towards increasing fidelity and can optimize the design and performance of radially-grown CNT architecture.

The ROM presented in Chapter 4 has been verified and validated for simple loading conditions such as uniaxial tensile and biaxial loading conditions. Verifying the model's predictive capability for more realistic and complex loading conditions will require a more sophisticated mode identification procedure that can preserve both the subscale and global features with sufficient accuracy. Implementing other mode identification procedures and adapting the model within a FE multiscale code can be aspects of future investigations.

REFERENCES

ABAQUS. 2013. *ABAQUS/Standard Analysis User's Manual Version 6.13-2.* Providence, Rhode

Aboudi, J. and Pindera, M.J., 2004. High-fidelity micromechanical modeling of continuously reinforced elastic multiphase materials undergoing finite deformations. *Mathematics and mechanics of solids*, *9*(6), pp.599-628.

Aldajah, S. and Haik, Y., 2012. Transverse strength enhancement of carbon fiber reinforced polymer composites by means of magnetically aligned carbon nanotubes. *Materials & Design*, *34*, pp.379-383.

Amsallem, D., Zahr, M., Choi, Y. and Farhat, C., 2015. Design optimization using hyper-reduced-order models. *Structural and Multidisciplinary Optimization*, *51*(4), pp.919-940.

Astrid, P., Weiland, S., Willcox, K. and Backx, T., 2008. Missing point estimation in models described by proper orthogonal decomposition. *IEEE Transactions on Automatic Control*, *53*(10), pp.2237-2251.

Balusu, K., Skinner, T. and Chattopadhyay, A., 2020. An efficient implementation of the high-fidelity generalized method of cells for complex microstructures. *Computational Materials Science*, *186*, p.110004.

Bhattacharyya, M. and Dureisseix, D., 2021. A multi-scale reduced-order-model strategy for transient thermo-elasticity with variable micro-structure. *International Journal for Numerical Methods in Engineering*.

Bhattacharyya, M., Dureisseix, D. and Faverjon, B., 2020. Numerical homogenisation based on asymptotic theory and model reduction for coupled elastic-viscoplastic damage. *International Journal of Damage Mechanics*, *29*(9), pp.1416-1444.

Bhattacharyya, M., Fau, A., Desmorat, R., Alameddin, S., Néron, D., Ladevèze, P. and Nackenhorst, U., 2019. A kinetic two-scale damage model for high-cycle fatigue simulation using multi-temporal Latin framework. *European Journal of Mechanics-A/Solids*, *77*, p.103808.

Boroujeni, A.Y., Tehrani, M., Nelson, A.J. and Al-Haik, M., 2014. Hybrid carbon nanotube–carbon fiber composites with improved in-plane mechanical properties. *Composites Part B: Engineering*, *66*, pp.475-483.

Carpenter, C.R., Shipway, P.H., Zhu, Y. and Weston, D.P., 2011. Effective dispersal of CNTs in the fabrication of electrodeposited nanocomposites. *Surface and Coatings Technology*, *205*(20), pp.4832-4837.

Chamis, C.C., Aiello, R.A. and Murthy, P.L., 1988. Fiber composite sandwich thermostructural behavior: computational simulation. *Journal of Composites, Technology and Research*, *10*(3), pp.93-99.

Chaturantabut, S. and Sorensen, D.C., 2010. Nonlinear model reduction via discrete empirical interpolation. *SIAM Journal on Scientific Computing*, *32*(5), pp.2737-2764.

Chatzigeorgiou, G., Efendiev, Y. and Lagoudas, D.C., 2011. Homogenization of aligned "fuzzy fiber" composites. *International Journal of Solids and Structures*, *48*(19), pp.2668-2680.

Chatzigeorgiou, G., Seidel, G.D. and Lagoudas, D.C., 2012. Effective mechanical properties of "fuzzy fiber" composites. *Composites Part B: Engineering*, *43*(6), pp.2577-2593.

Chen Z, Yan N. Investigation of elastic moduli of Kraft paper honeycomb core sandwich panels. Compos Part B–Eng 2012;43(5):2107–14.

Cho, B.G., Hwang, S.H., Park, M., Park, J.K., Park, Y.B. and Chae, H.G., 2019. The effects of plasma surface treatment on the mechanical properties of polycarbonate/carbon nanotube/carbon fiber composites. *Composites Part B: Engineering*, *160*, pp.436-445.

Cho, J., Daniel, I.M. and Dikin, D.A., 2008. Effects of block copolymer dispersant and nanotube length on reinforcement of carbon/epoxy composites. *Composites Part A: Applied Science and Manufacturing*, *39*(12), pp.1844-1850.

Chou, T.W., Gao, L., Thostenson, E.T., Zhang, Z. and Byun, J.H., 2010. An assessment of the science and technology of carbon nanotube-based fibers and composites. *Composites Science and Technology*, *70*(1), pp.1-19.

Chou, T.W., Gao, L., Thostenson, E.T., Zhang, Z. and Byun, J.H., 2010. An assessment of the science and technology of carbon nanotube-based fibers and composites. *Composites Science and Technology*, *70*(1), pp.1-19.

Dafedar JB, Desai YM. Thermomechanical buckling of laminated composite plates using mixed, higher-order analytical formulation. J Appl Mech, Trans ASME 2002;69:790–9.

Dai, G. and Mishnaevsky Jr, L., 2015. Carbon nanotube reinforced hybrid composites: Computational modeling of environmental fatigue and usability for wind blades. *Composites Part B: Engineering*, *78*, pp.349-360.

Datta, S., Fard, M.Y. and Chattopadhyay, A., 2015. High-speed surfactant-free fabrication of large carbon nanotube membranes for multifunctional composites. *Journal of Aerospace Engineering*, *29*(3), p.04015060.

Datta, Siddhant, Rajesh Kumar Neerukatti, and Aditi Chattopadhyay. "Buckypaper Embedded Self-Sensing Composite for Real-Time Fatigue Damage Diagnosis and Prognosis." *Carbon* (2018).

Dattaguru, B., Everett, R.A., Whitcomb, J.D., Johnson, W.S., "Geometrically Nonlinear Analysis of Adhesively Bonded Joints," *Journal of Engineering Materials and Technology*, Vol 106, No. 59, pp. 59-65, 1984.

Dey, Swapna, and Indranil Chattoraj. "Interaction of strain rate and hydrogen input on the embrittlement of 7075 T6 Aluminum alloy." Materials Science and Engineering: A 661 (2016): 168-178.

Dodla, S., 2018. Micromechanical Analysis for Two-Phase Copper-Silver Composites under Large Deformations. *Journal of Composites Science*, *2*(1), p.1.

Dvorak, G.J. and Benveniste, Y., 1992. On transformation strains and uniform fields in multiphase elastic media. *Proceedings of the Royal Society of London. Series A: Mathematical and Physical Sciences*, *437*(1900), pp.291-310.

Dvorak, G.J., Bahei-El-Din, Y.A. and Wafa, A.M., 1994. The modeling of inelastic composite materials with the transformation field analysis. *Modelling and Simulation in Materials Science and Engineering*, *2*(3A), p.571.

Farhat, C., Chapman, T. and Avery, P., 2015. Structure-preserving, stability, and accuracy properties of the energy-conserving sampling and weighting method for the hyper reduction of nonlinear finite element dynamic models. *International Journal for Numerical Methods in Engineering*, *102*(5), pp.1077-1110.

Feldhusen, Jörg, Christoph Warkotsch, and Alexander Kempf. "Development of a mechanical technology for joining sandwich elements." *Journal of Sandwich Structures & Materials* 11, no. 6 (2009): 471-486.

Ferrari, M., "Structurally Optimized and Additively Manufactured Inserts for Sandwich Panels of Spacecraft Structures," Swiss Federal Institute of Technology Zurich, Master's thesis no. 15-039, 2015.

Feyel, F., 2003. A multilevel finite element method (FE^2) to describe the response of highly nonlinear structures using generalized continua. *Computer Methods in applied Mechanics and engineering*, *192*(28-30), pp.3233-3244.

Freed, Y. and Aboudi, J., 2009. Micromechanical prediction of the two-way shape memory effect in shape memory alloy composites. *International Journal of Solids and Structures*, *46*(7-8), pp.1634-1647.

Fritzen, F. and Böhlke, T., 2010. Three-dimensional finite element implementation of the nonuniform transformation field analysis. *International Journal for Numerical Methods in Engineering*, *84*(7), pp.803-829.

Fritzen, F., 2013. *Microstructural modeling and computational homogenization of the physically linear and nonlinear constitutive behavior of micro-heterogeneous materials* (Vol. 1). KIT Scientific Publishing.

Frostig Y, Thomsen OT. Localized effects in the nonlinear behavior of sandwich panels with a transversely flexible core. J Sandwich Struct Mater 2005;7(1):53–75.

Frostig Y. Hygrothermal (environmental) effects in high-order bending of sandwich beams with a flexible core and a discontinuous skin. Compos Struct 1997;37(2):205–21.

Garcia, E.J., Wardle, B.L. and Hart, A.J., 2008. Joining prepreg composite interfaces with aligned carbon nanotubes. *Composites Part A: Applied Science and Manufacturing*, *39*(6), pp.1065-1070.

Gilat, A., Goldberg, R.K. and Roberts, G.D., 2002. Experimental study of strain-rate-dependent behavior of carbon/epoxy composite. *Composites Science and Technology*, *62*(10-11), pp.1469-1476.

Godara, A., Mezzo, L., Luizi, F., Warrier, A., Lomov, S.V., Van Vuure, A.W., Gorbatikh, L., Moldenaers, P. and Verpoest, I., 2009. Influence of carbon nanotube reinforcement on the processing and the mechanical behaviour of carbon fiber/epoxy composites. *Carbon*, *47*(12), pp.2914-2923.

Gorbatikh, L., Liu, Q., Romanov, V., Mehdikhani, M., Matveeva, A., Shishkina, O., Aravand, A., Wardle, B., Verpoest, I. and Lomov, S.V., 2018, August. Hierarchical design of structural composite materials down to the nanoscale via experimentation and modelling. In *IOP Conference Series: Materials Science and Engineering* (Vol. 406, No. 1, p. 012002). IOP Publishing.

Gorbatikh, L., Wardle, B.L. and Lomov, S.V., 2016. Hierarchical lightweight composite materials for structural applications. *Mrs Bulletin*, *41*(9), pp.672-677.

Green, K.J., Dean, D.R., Vaidya, U.K. and Nyairo, E., 2009. Multiscale fiber reinforced composites based on a carbon nanofiber/epoxy nanophased polymer matrix: synthesis, mechanical, and thermomechanical behavior. *Composites Part A: applied science and manufacturing*, *40*(9), pp.1470-1475.

Haj-Ali, R. and Aboudi, J., 2009. Nonlinear micromechanical formulation of the high fidelity generalized method of cells. *International Journal of Solids and Structures*, *46*(13), pp.2577-2592.

Haj-Ali, R. and Aboudi, J., 2013. A new and general formulation of the parametric HFGMC micromechanical method for two and three-dimensional multi-phase composites. *International Journal of Solids and Structures*, *50*(6), pp.907-919.

Haj-Ali, R., Zemer, H., El-Hajjar, R. and Aboudi, J., 2014. Piezoresistive fiber-reinforced composites: a coupled nonlinear micromechanical–microelectrical modeling approach. *International Journal of Solids and Structures*, *51*(2), pp.491-503.

Halgren, T.A., 1996. Merck molecular force field. I. Basis, form, scope, parameterization, and performance of MMFF94, *Journal of Computational Chemistry,* Vol. 17, No. 5-6, pp. 490-519.

Hassanzadeh-Aghdam, M.K., Ansari, R. and Darvizeh, A., 2018. Micromechanical analysis of carbon nanotube-coated fiber-reinforced hybrid composites. *International Journal of Engineering Science*, *130*, pp.215-229.

He, X., Zhang, F., Wang, R. and Liu, W., 2007. Preparation of a carbon nanotube/carbon fiber multi-scale reinforcement by grafting multi-walled carbon nanotubes onto the fibers. *Carbon*, *45*(13), pp.2559-2563.

Hegde, Sandesh Rathnavarma, and Mehdi Hojjati. "Thermally induced microcracks and mechanical property of composite honeycomb sandwich structure: experiment and finite element analysis." Journal of Sandwich Structures & Materials (2018): 1099636218802432.

Heimbs, Sebastian, and Marc Pein. "Failure behaviour of honeycomb sandwich corner joints and inserts." *Composite Structures* 89, no. 4 (2009): 575-588.

Hernandez, J.A., Caicedo, M.A. and Ferrer, A., 2017. Dimensional hyper-reduction of nonlinear finite element models via empirical cubature. *Computer methods in applied mechanics and engineering*, *313*, pp.687-722.

Huang, S.Y., Wu, G.P., Chen, C.M., Yang, Y., Zhang, S.C. and Lu, C.X., 2013. Electrophoretic deposition and thermal annealing of a graphene oxide thin film on carbon fiber surfaces. *Carbon*, *52*, pp.613-616.

Iarve, Endel V., Kevin H. Hoos, Michael Braginsky, Eric Zhou, and David Mollenhauer. "Tensile and compression strength prediction in laminated composites by using Discrete Damage Modeling." In *56th AIAA/ASCE/AHS/ASC Structures, Structural Dynamics, and Materials Conference*, p. 1880. 2015.

Inam, F., Wong, D.W., Kuwata, M. and Peijs, T., 2010. Multiscale hybrid micro-nanocomposites based on carbon nanotubes and carbon fibers. *Journal of Nanomaterials*, *2010*, p.9. Island, USA: Dassault Systémes Simulia Corp.

J. W. Klintworth and W. J. Stronge, "Elasto-plastic yield limits and deformation laws for transversely crushed honeycombs," International Journal of Mechanical Sciences, vol. 30, no. 3-4, pp. 273–292, 1988

Jiang, Q., Tallury, S.S., Qiu, Y. and Pasquinelli, M.A., 2020. Interfacial characteristics of a carbon nanotube-polyimide nanocomposite by molecular dynamics simulation. *Nanotechnology Reviews*, *9*(1), pp.136-145.

Jirasek, M. 2002. "Objective Modeling of Strain Localization," Revue Francaise Genile Civil, 6 (6):1119-1132.

Jorgensen, W.L., Maxwell, D.S., and Tirado-Rives, J., "Development and testing of the OPLS all-atom force field on conformational energetics and properties of organic liquids," *Journal of the American Chemical Society,* Vol. 118, No. 45, 1996, pp. 11225-11236.

Ju, X. and Mahnken, R., 2016. An NTFA-based homogenization framework considering softening effects. *Mechanics of Materials*, *96*, pp.106-125.

Jung, H., Choi, H.K., Oh, Y., Hong, H. and Yu, J., 2020. Enhancement of thermo-mechanical stability for nanocomposites containing plasma treated carbon nanotubes with an experimental study and molecular dynamics simulations. *Scientific reports*, *10*(1), pp.1-10.

Jyoti, J., Basu, S., Singh, B.P. and Dhakate, S.R., 2015. Superior mechanical and electrical properties of multiwall carbon nanotube reinforced acrylonitrile butadiene styrene high performance composites. *Composites Part B: Engineering*, *83*, pp.58-65.

Kapuria S, Achary GGS. An efficient higher-order zigzag theory for laminated plates subjected to thermal loading. Int J Solids Struct 2004;41:4661–84.

Karapappas, P., Vavouliotis, A., Tsotra, P., Kostopoulos, V. and Paipetis, A., 2009. Enhanced fracture properties of carbon reinforced composites by the addition of multi-wall carbon nanotubes. *Journal of Composite Materials*, *43*(9), pp.977-985.

Kin-Tak, L.; San-Qiang, S.; Li-Min, Z.; Hui-Ming, C. Micro-hardness and flexural properties of randomly-oriented carbon nanotube composites. J. Compos. Mater. 2003, 37, 365–376. 120.

Koo, B., Liu, Y., Zou, J., Chattopadhyay, A. and Dai, L.L., 2014. Study of glass transition temperature (Tg) of novel stress-sensitive composites using molecular dynamic simulation. *Modelling and Simulation in Materials Science and Engineering*, *22*(6), p.065018.

Krishnamurthy, A., Hunston, D.L., Forster, A.L., Natarajan, B., Liotta, A.H., Wicks, S.S., Stutzman, P.E., Wardle, B.L., Liddle, J.A. and Forster, A.M., 2017. Enhanced durability of carbon nanotube grafted hierarchical ceramic microfiber-reinforced epoxy composites. *Carbon*, *125*, pp.63-75.

Kulkarni, M., Carnahan, D., Kulkarni, K., Qian, D. and Abot, J.L., 2010. Elastic response of a carbon nanotube fiber reinforced polymeric composite: a numerical and experimental study. *Composites Part B: Engineering*, *41*(5), pp.414-421.

Kumar, S.; Han Gi, C.; Sreekumar, T.V.; Uchida, T. A comparison of reinforcement efficiency of various types of carbon nanotubes in polyacrylonitrile fiber. Polymer 2005, 46, 10925–10935. 121.

Kundalwal, S.I. and Ray, M.C., 2011. Micromechanical analysis of fuzzy fiber reinforced composites. *International Journal of Mechanics and Materials in Design*, *7*(2), pp.149-166.

Kundalwal, S.I. and Ray, M.C., 2012. Effective properties of a novel continuous fuzzy-fiber reinforced composite using the method of cells and the finite element method. *European Journal of Mechanics-A/Solids*, *36*, pp.191-203.

Lampman, S., and T. B. Zore. "Properties and selection: nonferrous alloys and special-purpose materials." *ASM Handbook* 2 (1990): 592-633.

Lapczyk, I. and J.A. Hurtado. 2007. "Progressive Damage Modeling in Fiber-Reinforced Materials," Compos. Part A-Appl. S., 38(11):2333-2341.

Largenton, R., Michel, J.C. and Suquet, P., 2014. Extension of the nonuniform transformation field analysis to linear viscoelastic composites in the presence of aging and swelling. *Mechanics of Materials*, *73*, pp.76-100.

Lee, Hyo S., Soon H. Hong, Jae R. Lee, and Yeung K. Kim. "Mechanical behavior and failure process during compressive and shear deformation of honeycomb composite at elevated temperatures." *Journal of Materials Science* 37, no. 6 (2002): 1265-1272.

Lettiere, B.R., Chazot, C.A., Cui, K. and Hart, A.J., 2019. High-density carbon nanotube forest growth on copper foil for enhanced thermal and electrochemical interfaces. *ACS Applied Nano Materials*, *3*(1), pp.77-83.

Li DH, Wang RP, Qian RL, Liu Y, Qing GH. Static response and free vibration analysis of the composite sandwich structures with multi-layer cores. Int J Mech Sci 2016;111:101–15.

Li, K., Gu, B. and Zhu, W., 2017, March. Molecular dynamics simulation aiming at interfacial characteristics of polymer chains on nanotubes with different layers. In *AIP Conference Proceedings* (Vol. 1820, No. 1, p. 020005). AIP Publishing LLC.

Liu B, Ferreira AJM, Xing YF, Neves AMA. Analysis of functionally graded sandwich and laminated shells using a layerwise theory and a differential quadrature finite element method. Compos Struct 2016;136:546–53.

Liu, Q., Gorbatikh, L. and Lomov, S.V., 2019. A combined use of embedded and cohesive elements to model damage development in fibrous composites. *Composite Structures*, *223*, p.110921.

Liu, Q., Lomov, S.V. and Gorbatikh, L., 2020. When does nanotube grafting on fibers benefit the strength and toughness of composites? *Composites Science and Technology*, p.107989.

Lu, F., Liu, Q., Druzhinin, P., Vandepitte, D., Zhou, G. and Lomov, S.V., 2019. Reduction of the volume redundancy in combined embedded elements/cohesive zone modelling-Comments on the paper: Liu Q, Gorbatikh L, Lomov SV. A combined use of embedded and cohesive elements to model damage development in fibrous composites, Composite Structures, 2019, 223: 110921. *Composite Structures*, *226*.

Lurie, S.A., Volkov-Bogorodskiy, D.B., Menshykov, O., Solyaev, Y.O. and Aifantis, E.C., 2018. Modeling the effective mechanical properties of "fuzzy fiber" composites across scales length. *Composites Part B: Engineering*, *142*, pp.24-35.

Lyford, Andrew Lindquist. "Failure Prediction of Honeycomb Panel Joints using Finite Element Analysis." PhD diss., Virginia Tech, 2017.

M. Giglio, A. Gilioli, and A. Manes, "Numerical investigation of a three-point bending test on sandwich panels with aluminum skins and Nomex honeycomb core," Computational Materials Science, vol. 56, pp. 69–78, 2012.

Maimi P., Camanho P.P., Mayugo J.A., Davila C.G., "A continuum damage model for composite laminates: Part II – Computational implementation and validation", Mechanics of Materials, 2007; 39: 909-919

Malekimoghadam, R. and Icardi, U., 2019. Prediction of mechanical properties of carbon nanotube–carbon fiber reinforced hybrid composites using multi-scale finite element modelling. *Composites Part B: Engineering*, *177*, p.107405.

Matveeva, A.Y., Lomov, S.V. and Gorbatikh, L., 2019. Debonding at the fiber/matrix interface in carbon nanotube reinforced composites: Modelling investigation. *Computational Materials Science*, *159*, pp.412-419.

Matzenmiller, A, J. Lubliner and R. L. Taylor. 1995. "A Constitutive Model for Anisotropic Damage in Fiber-Composites," Mech. Mater., 20(2):125–152

Medina, C., Fernandez, E., Salas, A., Naya, F., Molina-Aldereguía, J., Melendrez, M.F. and Flores, P., 2017. Multiscale characterization of nanoengineered fiber-reinforced composites: effect of carbon nanotubes on the out-of-plane mechanical behavior. *Journal of Nanomaterials*, *2017*.

Michel, J.C. and Suquet, P., 2003. Nonuniform transformation field analysis. *International journal of solids and structures*, *40*(25), pp.6937-6955.

Michel, J.C. and Suquet, P., 2010. Non-uniform transformation field analysis: a reduced model for multiscale nonlinear problems in solid mechanics. In *Multiscale Modeling In Solid Mechanics: Computational Approaches* (pp. 159-206).

Mindlin RD. Influence of transverse shear deformation on the bending of classical plates. J Appl Mech 1951;18:31–8.

Moaseri, E., Karimi, M., Maghrebi, M. and Baniadam, M., 2014. Fabrication of multi-walled carbon nanotube–carbon fiber hybrid material via electrophoretic deposition followed by pyrolysis process. *Composites Part A: Applied Science and Manufacturing*, *60*, pp.8-14.

Monteiro, E., Yvonnet, J. and He, Q.C., 2008. Computational homogenization for nonlinear conduction in heterogeneous materials using model reduction. *Computational Materials Science*, *42*(4), pp.704-712.

Murthy, P. L., & Chamis, C. C. 1986. Integrated Composite Analyzer (ICAN)-Users and Programmers Manual (No. NASA-E-2035).

Naghipour, P., Arnold, S.M., Pineda, E.J., Stier, B., Hansen, L., Bednarcyk, B.A. and Waas, A.M., 2017. Multiscale static analysis of notched and unnotched laminates using the generalized method of cells. *Journal of Composite Materials*, *51*(10), pp.1433-1454.

Najafizadeh MM, Heydari HR. 2004. Thermal buckling of functionally graded circular plates based on higher-order shear deformation plate theory. Eur J Mech A/ Solids, 23:1085–100.

Ogasawara, T., Ishida, Y. and Kasai, T., 2009. Mechanical properties of carbon fiber/fullerene-dispersed epoxy composites. *Composites Science and Technology*, *69*(11-12), pp.2002-2007.

Ogasawara, T., Ishida, Y. and Kasai, T., 2009. Mechanical properties of carbon fiber/fullerene-dispersed epoxy composites. *Composites Science and Technology*, *69*(11-12), pp.2002-2007.

Oliver, J., Caicedo, M., Huespe, A.E., Hernández, J.A. and Roubin, E., 2017. Reduced order modeling strategies for computational multiscale fracture. *Computer Methods in Applied Mechanics and Engineering*, *313*, pp.560-595.

Oskay, C. and Fish, J., 2007. Eigendeformation-based reduced order homogenization for failure analysis of heterogeneous materials. *Computer Methods in Applied Mechanics and Engineering*, *196*(7), pp.1216-1243.

Paley, M. and Aboudi, J., 1992. Micromechanical analysis of composites by the generalized cells model. *Mechanics of materials*, *14*(2), pp.127-139.

Park, Y. B., J. H. Kweon, and J. H. Choi. "Strength of Composite Sandwich Joints under Hygrothermal Condition." In *18th International Conference on Composites Materials (ICCM)*, pp. 21-26. 2011.

Peherstorfer, B., Butnaru, D., Willcox, K. and Bungartz, H.J., 2014. Localized discrete empirical interpolation method. *SIAM Journal on Scientific Computing*, *36*(1), pp.A168-A192.

Petras, A., Sutcliffe, M.P.F., "Failure Mode Maps for Honeycomb Sandwich Panels," Composite Structures, Vol. 44, No. 4, pp. 237-252, 1999.

Pineda, E. J. and A. M. Waas. 2013. "Numerical Implementation of a Multiple-ISV Thermodynamically-Based Work Potential Theory for Modeling Progressive Damage and Failure in Fiber-Reinforced Laminates," Int. J. Fracture, 182(1):93-122.

Pineda, E.J., Fassin, M., Bednarcyk, B.A., Reese, S. and Simon, J.W., 2017, July. Comparison of Multiscale Method of Cells-Based Models for Predicting Elastic Properties of Filament Wound C/C-SiC. In *Proceedings of the American Society for Composites—Thirty-second Technical Conference*.

Pinho S.T., Robinson P., Iannucci L., "Fracture toughness of the tensile and compressive fibre failure modes in laminated composites", Composites Science and Technology, 2006; 66: 2069-2079

Pozegic, T.R., Anguita, J.V., Hamerton, I., Jayawardena, K.D.I., Chen, J.S., Stolojan, V., Ballocchi, P., Walsh, R. and Silva, S.R.P., 2016. Multi-functional carbon fibre composites using carbon nanotubes as an alternative to polymer sizing. *Scientific reports*, *6*(1), pp.1-11.

Q. S. Yang and W. Becker, "A comparative investigation of different homogenization methods for prediction of the macroscopic properties of composites," Computer Modeling in Engineering and Sciences, vol. 6, no. 4, pp. 319–332, 2004.

Qian, H., Bismarck, A., Greenhalgh, E.S., Kalinka, G. and Shaffer, M.S., 2008. Hierarchical composites reinforced with carbon nanotube grafted fibers: the potential assessed at the single fiber level. *Chemistry of Materials*, *20*(5), pp.1862-1869.

Rafiee, R. and Ghorbanhosseini, A., 2017. Stochastic multi-scale modeling of randomly grown CNTs on carbon fiber. *Mechanics of Materials*, *106*, pp.1-7.

Rafiee, R. and Ghorbanhosseini, A., 2018. Predicting mechanical properties of fuzzy fiber reinforced composites: radially grown carbon nanotubes on the carbon fiber. *International Journal of Mechanics and Materials in Design*, *14*(1), pp.37-50.

Rai, A. and Chattopadhyay, A., 2018. Multifidelity multiscale modeling of nanocomposites for microstructure and macroscale analysis. *Composite Structures*, *200*, pp.204-216.

Rai, A., Datta, S., Chattopadhyay, A. and Lopez, C., 2017, January. Reinforcement of composite joint interface using nanomaterials. In *ASME 2017 International Mechanical Engineering Congress and Exposition*. American Society of Mechanical Engineers Digital Collection.

Rai, A., Subramanian, N. and Chattopadhyay, A., 2017. Investigation of damage mechanisms in CNT nanocomposites using multiscale analysis. *International Journal of Solids and Structures*, *120*, pp.115-124.

Rai, A., Subramanian, N., Koo, B. and Chattopadhyay, A., 2017. Multiscale damage analysis of carbon nanotube nanocomposite using a continuum damage mechanics approach. *Journal of Composite Materials*, *51*(6), pp.847-858.

Rangari, V.K.; Yousuf, M.; Jeelani, S.; Pulikkathara, M.X.; Khabashesku, V.N. Alignment of carbon nanotubes and reinforcing effects in nylon-6 polymer composite fibers. Nanotechnology 2008, 19, 245703.

Reddy JN. Energy and variational methods in applied mechanics. New York: Wiley; 1984.

Relun, Nicolas, David Néron, and Pierre-Alain Boucard. "A model reduction technique based on the PGD for elastic-viscoplastic computational analysis." *Computational Mechanics* 51, no. 1 (2013): 83-92.

Robens-Radermacher, Annika, Thomas E. Lacy Jr, Brett A. Bednarcyk, E. J. Pineda, S. M. Arnold, and T. M. Ricks, 2018. Solution of the nonlinear high-fidelity generalized method of cells micromechanics relations via order-reduction techniques.

Romanov, V.S., Lomov, S.V., Verpoest, I. and Gorbatikh, L., 2014. Can carbon nanotubes grown on fibers fundamentally change stress distribution in a composite? *Composites Part A: Applied Science and Manufacturing*, *63*, pp.32-34.

Romanov, V.S., Lomov, S.V., Verpoest, I. and Gorbatikh, L., 2015. Modelling evidence of stress concentration mitigation at the micro-scale in polymer composites by the addition of carbon nanotubes. *Carbon*, *82*, pp.184-194.

Roussette, S., Michel, J.C. and Suquet, P., 2009. Nonuniform transformation field analysis of elastic–viscoplastic composites. *Composites Science and Technology*, *69*(1), pp.22-27.

Russell, B.P., Liu, T., Fleck, N.A. and Deshpande, V.S., 2011. Quasi-static three-point bending of carbon fiber sandwich beams with square honeycomb cores. *Journal of applied mechanics*, *78*(3).

Ryckelynck, D., 2009. Hyper-reduction of mechanical models involving internal variables. *International Journal for Numerical Methods in Engineering*, *77*(1), pp.75-89.

Ryckelynck, David. "A priori hyperreduction method: an adaptive approach." *Journal of computational physics* 202, no. 1 (2005): 346-366.

Seyhan, A.T., Tanoglu, M. and Schulte, K., 2008. Mode I and mode II fracture toughness of E-glass non-crimp fabric/carbon nanotube (CNT) modified polymer based composites. *Engineering Fracture Mechanics*, *75*(18), pp.5151-5162.

Sharma, S.P. and Lakkad, S.C., 2011. Effect of CNTs growth on carbon fibers on the tensile strength of CNTs grown carbon fiber-reinforced polymer matrix composites. *Composites Part A: Applied Science and Manufacturing*, *42*(1), pp.8-15.

Shimokawa, Toshiyuki, Hisaya Katoh, Yasumasa Hamaguchi, Shigeo Sanbongi, Hiroshi Mizuno, Hiroyuki Nakamura, Ryoji Asagumo, and Hirobumi Tamura. "Effect of thermal cycling on microcracking and strength degradation of high-temperature polymer composite materials for use in next-generation SST structures." *Journal of composite materials* 36, no. 7 (2002): 885-895.

Shokrieh, M.M., Kefayati, A.R. and Chitsazzadeh, M., 2012. Fabrication and mechanical properties of clay/epoxy nanocomposite and its polymer concrete. *Materials & Design*, *40*, pp.443-452.

Singh, S.K., Srinivasan, S.G., Neek-Amal, M., "Thermal properties of fluorinated graphene," *Physical Review B,* Vol. 87, No. 10, 2013, pp. 104114.

Skoček, J., Zeman, J., & Šejnoha, M. (2008). Effective properties of textile composites: application of the Mori–Tanaka method. Modelling and Simulation in Materials Science and Engineering, 16(8), 085002.

Smith B, Banerjee B. Reliability of inserts in sandwich composite panels. Compos Struct 2012;94(3):820–9.

Snead, James M., and A. N. Palazotto. "Moisture and temperature effects on the instability of cylindrical composite panels." *Journal of aircraft* 20, no. 9 (1983): 777-783.

Stapleton, Waas, Bednarcyk. "Modeling Progressive Failure of Bonded Joints Using a Single Joint Finite Element " *NASA/TM*—2010-216824, 2010

Stoumbos, Tom G., Shahriar Setoodeh, Justin Francis, and Daniel Curtis. "Adhesively bonded joint modeling using finite element method for failure mode prediction." In *55th AIAA/ASME/ASCE/AHS/SC Structures, Structural Dynamics, and Materials Conference*, p. 1531. 2014.

Subramanian, N., B. Koo, A. Rai, and A. Chattopadhyay. "A multiscale damage initiation model for CNT-ehanced epoxy polymers." In *20th International Conference on Composite Materials. Copenhagen, Den-mark*, pp. 4410-4418. 2013.

Subramanian, N., Koo, B., Venkatesan, K.R. and Chattopadhyay, A., 2018. Interface mechanics of carbon fibers with radially-grown carbon nanotubes. *Carbon*, *134*, pp.123-133.

Subramanian, N., Rai, A. and Chattopadhyay, A., 2015. Atomistically informed stochastic multiscale model to predict the behavior of carbon nanotube-enhanced nanocomposites. *Carbon*, *94*, pp.661-672.

Subramanian, Nithya, and Aditi Chattopadhyay. "Molecular Dynamics Simulations for the Analysis of Nano-engineered Fuzzy Fiber Composites." In *2018 AIAA/AHS Adaptive Structures Conference*, p. 1284. 2018

Subramaniyan, A.K., and Sun, C., "Continuum interpretation of virial stress in molecular simulations," International Journal of Solids and Structures, Vol. 45, No. 14, 2008, pp. 4340-4346.

Suk, M.E., 2020. Atomistic behavior of nanoporous carbon nanotube-aluminum composite under compressive loading. *Materials Research Express*, *7*(1), p.015028.

Swaminathan, S., Ghosh, S., & Pagano, N. J. (2006). Statistically equivalent representative volume elements for unidirectional composite microstructures: Part I-Without damage. Journal of composite materials, 40(7), 583-604.

Tayfun, U., Kanbur, Y., Abaci, U., Guney, H.Y. and Bayramli, E., 2015. Mechanical, flow and electrical properties of thermoplastic polyurethane/fullerene composites: Effect of surface modification of fullerene. *Composites Part B: Engineering*, *80*, pp.101-107.

Thakre, P.R., Lagoudas, D.C., Riddick, J.C., Gates, T.S., Frankland, S.J.V., Ratcliffe, J.G., Zhu, J. and Barrera, E.V., 2011. Investigation of the effect of single wall carbon nanotubes on interlaminar fracture toughness of woven carbon fiber—epoxy composites. *Journal of Composite Materials*, *45*(10), pp.1091-1107.

Thostenson, E.T., Ren, Z. and Chou, T.W., 2001. Advances in the science and technology of carbon nanotubes and their composites: a review. *Composites science and technology*, *61*(13), pp.1899-1912

Tikarrouchine, E., Chatzigeorgiou, G., Praud, F., Piotrowski, B., Chemisky, Y. and Meraghni, F., 2018. Three-dimensional FE2 method for the simulation of nonlinear, rate-dependent response of composite structures. *Composite Structures*, *193*, pp.165-179.

Tuttle, Mark. "Impact of Moisture and Thermal Cycling on Delamination Fracture Toughness of Sandwich Composites." In *2018 AIAA/ASCE/AHS/ASC Structures, Structural Dynamics, and Materials Conference*, p. 2247. 2018.

Vaganov, G., Yudin, V., Vuorinen, J. and Molchanov, E., 2016. Influence of multiwalled carbon nanotubes on the processing behavior of epoxy powder compositions and on the mechanical properties of their fiber reinforced composites. *Polymer composites*, *37*(8), pp.2377-2383.

van Tuijl, R.A., Remmers, J.J. and Geers, M.G., 2018. Integration efficiency for model reduction in micro-mechanical analyses. *Computational mechanics*, *62*(2), pp.151-169.

Venkatesan, K.R., Subramanian, N., Rai, A. and Chattopadhyay, A., 2019. Atomistically informed multiscale modeling of radially grown nanocomposite using a continuum damage mechanics approach. *Carbon*, *142*, pp.420-429.

Wang, C., Li, Y., Tong, L., Song, Q., Li, K., Li, J., Peng, Q., He, X., Wang, R., Jiao, W. and Du, S., 2014. The role of grafting force and surface wettability in interfacial enhancement of carbon nanotube/carbon fiber hierarchical composites. *Carbon*, *69*, pp.239-246.

Wicks, S.S., de Villoria, R.G. and Wardle, B.L., 2010. Interlaminar and intralaminar reinforcement of composite laminates with aligned carbon nanotubes. *Composites Science and Technology*, *70*(1), pp.20-28.

Wicks, S.S., Wang, W., Williams, M.R. and Wardle, B.L., 2014. Multi-scale interlaminar fracture mechanisms in woven composite laminates reinforced with aligned carbon nanotubes. *Composites Science and Technology*, *100*, pp.128-135.

Wood, C.D., Palmeri, M.J., Putz, K.W., Ho, G., Barto, R. and Brinson, L.C., 2012. Nanoscale structure and local mechanical properties of fiber-reinforced composites containing MWCNT-grafted hybrid glass fibers. *Composites Science and Technology*, *72*(14), pp.1705-1710.

Xu, Y. and Van Hoa, S., 2008. Mechanical properties of carbon fiber reinforced epoxy/clay nanocomposites. *Composites Science and Technology*, *68*(3-4), pp.854-861.

Zang, J., Yuan, Q., Wang, F., "A comparative study of Young's modulus of single-walled carbon nanotube by CPMD, MD and first principle simulations," *Computational Materials Science,* Vol. 46, No. 3, 2009, pp. 621-625.

Zhang, F.H., Wang, R.G., He, X.D., Wang, C. and Ren, L.N., 2009. Interfacial shearing strength and reinforcing mechanisms of an epoxy composite reinforced using a carbon nanotube/carbon fiber hybrid. *Journal of materials science*, *44*(13), pp.3574-3577.

Zhong, Y., Bansal, Y. and Pindera, M.J., 2004. Efficient reformulation of the thermal higher-order theory for fgms with locally variable conductivity. *International Journal of Computational Engineering Science*, *5*(04), pp.795-831.